Università di Bologna
Dipartimento di Chimica Applicata e
Scienza dei Materiali

Università di Padova
Dipartimento di Ingegneria Meccanica
Settore Materiali

Lisa Biasetto

Dottorato di Ricerca in
Ingegneria dei Materiali
ING-IND/22
XIX Ciclo
a.a. 2005-06

Functional Ceramic Foams from Preceramic Polymers

Schiume Ceramiche Funzionalizzate
a partire da Polimeri Preceramici

Relatore: Prof. Paolo Colombo

Coordinatore: Prof. Giorgio Timellini

Index

Chapter 4- High Specific Surface Area SiOC microcellular foams

Appendix 1- Properties of Cellular Ceramics

Appendix 2- Characterization of structure and morphology

Introduction

The fabrication of ceramics via non-conventional techniques such as chemical-vapour-deposition, sol-gel technology and polymer pyrolysis has been attracting a lot of attention in the last decades. The reason of this great interest is due to interconnecting factors. Non-conventional techniques are the answer to increasing request of new applications for ceramics; on the other hand, the design of materials on the micro and nano-scale needs new processing routes.

Through this innovation path *Polymer-Derived-Ceramics* (PDCs) have been developed.

In the mid 1970s Yajima et al.[1] reported some investigations that confirmed a new method for producing advanced ceramics at significantly lower temperatures (800-1500°C) than conventional sintering processing. Since then many progresses have been reported by the international scientific community.

Nowdays PDCs find several applications as engineered components (MEMS, fibers, membranes, filters and biomaterials) and many patents have been submitted.

The reason of this developement is related to both their peculiar chemical-physical properties and their advantageus processing route.

In ceramics produced by powders processing, the presence of porosity has been considered a problem for many years. However in the last decades porosity and *cellular solids* have gained incresing attention because of their unique set of properties. Gibson and Ashby[2] reported a complete characterization of cellular solids (polymers, metals and ceramics) and their applications. More recently a more specific overview on cellular ceramics was published by Scheffler and Colombo[3]. These materials have properties that depend on both topology and composition, and they are growing importance as filters, catalyst supports, membranes, and scaffolds for cell growth.

The devolpement of the foaming process and of characterization techniques for porous solids allow to design materials with tailored morphology, composition and properties.

The present work wants to offer a complete characterization of polymer-derived SiOC microcellular foams, furthermore it wants to investigate new fields of applications for these materials.

SiOC micro-foams are functionalized by different techniques in order to prove the process versatility, the material tailorability and to provide further applications.

L. Biasetto

References

[1] Yajima, S., Hajashi, J. et al., *Nature, 261 (1976) 683*
[2] Gibson, L. J., Ashby, M. F., *Cellular Solids: Structure and Properties*, Cambridge University press, 1999
[3] Scheffler, M. and Colombo, P. *Cellular Ceramics*, WILEY-VCH Verlag GmbH & Co. KgaA, Weinheim, 2005

Chapter 1

Polymer-Derived Porous Structures

1.1 Cellular Structures

Nature offers various examples of cellular structures such as wood, corals and sea sponge, bones and bee honeycombs, and often researchers look at nature to design new materials (Figure 1.1).

Plastic cellular materials were first developed in order to answer the great need of polymeric components that the market started to ask after the 1950s.

The need of cheap plastic components usable in many everyday-life applications drove industries and reserachers to look for alternative production routes. The main advantages in using cellular plastics were given by the lower amount of material needed than fully bulk components and consequently their low density value.

This concept can be considered the key point for cellular structures, since their low density combined to their specific morphology give rise to a very unique set of properties.

Nowdays cellular structures are produced as plastics, ceramics and metals, and they find a very widespread use in usual engineering applications.

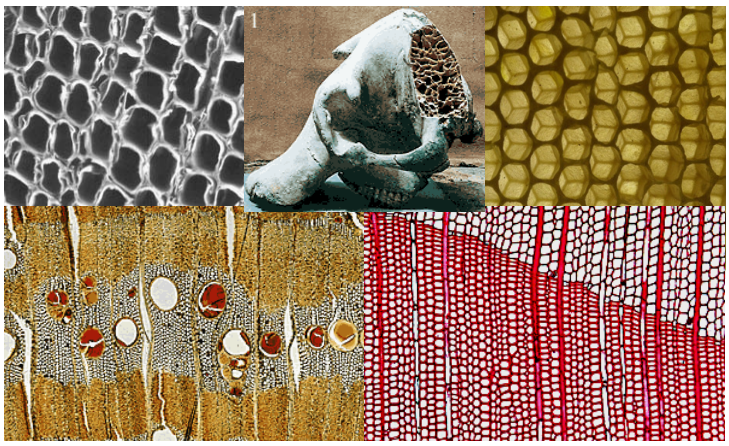

Figure 1.1- Cellular structures from nature: sea sponge, bones, bee honeycomb and wood.

The basic unit of cellular structures is a “cell” that is packed to efficiently fill space. Cells are enclosed empty spaces sorrounded by walls and edges. The final architecture of the material is determined by the way cells are packed: they can be

oriented (honeycomb) or random (foam). The connection between cells is called strut and the interconnection between cells (if present) is called cell-window (open cells).
Beside the material of which the cellular structure is made, the average cells size, shape and distribuition, their degree of interconnectivity (open *vs* closed-cells), the degree of anisotropicity (graded porosity) , the struts density and morphology (dense *vs* hollow), the amount of porosity (relative density) are all factors that deeply influence the final material properties.
Ceramic cellular structures are rapidly growing importance as filters, catalyst supports, membranes, and scaffolds for cell growth. Ceramic foams, honeycombs, connected fibers and three-dimensional periodic structures are all belonging to this class of materials (Figure 1.2).

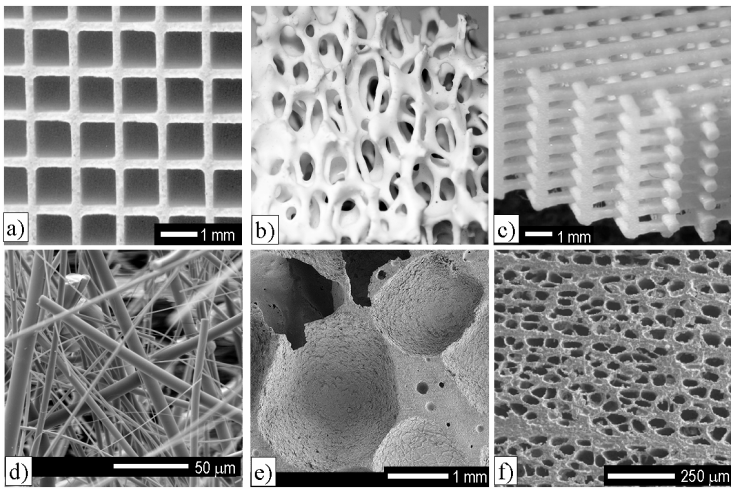

Figure 1.2- Examples of different classes of cellular ceramics with varied morphology. a) honeycomb, b) foam, c) scaffold (courtesy of J. Lewis, University of Illinois), d) fibre mat, e) connected hollow spheres (courtesy of J. Luyten, VITO), f) biomimetic structure (courtesy of H. Sieber and P. Greil, University of Erlangen). Courtesy of E. Bernardo, P. Colombo, Università di Padova[1]).

However the current terminology used to define porosity doesn't include the broad class of cellular structures. IUPAC (The International Union of Pure and Applied Chemistry) defined porous solids and pores mainly with the aim of helping the characterization of catalytic materials[2].
So a porous solid is defined as "a solid with pores, i.e. cavities, channels or interstices, which are deeper than they are wide" (which is not always the case, see for instance foams) and the *pore size* (generally pore width) as "the distance between two opposite walls of the pore". More importantly, it classifies the pore size into three different dimensional ranges: *micropores* (< 2 nm), *mesopores* (2-50 nm) and *macropores* (> 50 nm). According to this definition, thus, all cellular ceramics are constituted only of macropores, a generalization which does not help in describing their porous architecture in a detailed way.

In order to allow their description new definitions have been proposed.
As usual these defitions are deeply affected by the measurement method available for the material characterization. In *Appendix 2,* the analytical methods for the characterization of cellular solids are reported.
Cell size is defined as the cell diameter, it is usually measured in a 2D section and then properly converted to a 3D value. Cell density is defined as the number of cells per unit volume. These parameters can be both calculated and measured and the values compared.
The watershed, in terms of cell density, defining the border line between microcellular and macrocellular solids is 10^9 cells/cm^3 . Microcellular solids possess cell size <30 - 50 μm and macrocellular solids have cell sizes ranging from 50 μm to some mm.
The underlying principles that influence cellular properties are common to all three classes (polymers, metals and ceramics). Three factors dominate:

- The properties of the solid of which the material is made
- The topology (interconnectivity) and shape of cells
- The relative density ρ/ρ_s, where ρ is the density of the foam and ρ_s that of the solid of which it is made[3].

Besides taking into account the macrostructure and morphology one should keep in mind the material microstructure that is often a consequence of the processing route.
For istance, the presence of microvoids in cells and struts can be generated both from incomplete sintering and the foaming technique. As a consequence the final cellular structure properties are the result of the starting materials used and the technological route used to produce it.
Their properties (mechanical, thermal, electrical, acoustic, permeability of cellulars solids) differ from bulk materials of the same composition and they will be discussed in detail in *Appendix 1.* In Table 1.1 an overview of the unique set of properties typical of cellular ceramics is reported.
One of the most important application of cellular ceramics is the use as molten metal filters. Ceramic filters permit the removal of solid inclusions, the elimination of trapped gas, and provide laminar streams of the metal to fill the castings, thus representing a cost effective productivity enhancement in foundries.
Honeycomb, foam or fibre-based filters are used as a catalyst support for several key applications, including automotive or industrial exhaust gas purification.

Table 1.1- Typical Properties of cellular ceramics

Low	High
▪ Density	▪ Specific strength
▪ Thermal conductivity	▪ Specific stiffness
▪ Dielectric constant	▪ Permeability
▪ Thermal mass	▪ Thermal shock resistance
▪ Electrical conductivity	▪ Porosity
	▪ Specific surface area
	▪ Hardness / wear resistance
	▪ Resistance to chemical corrosion
	▪ Tortuosity of flow paths

High temperature catalytic ceramic filters for simultaneous abatement of dust and gaseous pollutants are widely used in traps for diesel particulate abatement and baghouse filters for incinerators, boilers, etc. These cellular traps filter particulate either according to a superficial or "shallow-bed" filtration mechanism (honeycombs) or to interstitial or "deep" filtration mechanism (foams).

A recent application is that of cellular ceramics as porous-medium burners. Their use in the premixed combustion of various fuels, either within or near the surface of the inert porous ceramic, permits energy saving and significantly reduced NO_x emissions.

In another recent development, cellular ceramics (foams or 3D scaffolds) are being used in tissue engineering and tissue regeneration. In the first case cellular structures are used as templates for tissue growth, while the second case involves the direct implantation of an engineered scaffold (seeded with cells or not) into a defect to guide and stimulate tissue repair in situ.

Several other applications have been envisioned and exploited for cellular ceramics; among these are implantable drug delivery system, 3D reinforcement for metal or polymer matrix composites, thermal protection systems (thermal shields for the aerospace industry), kiln furniture (their low thermal mass allows a faster furnace shut down and significant energy saving), emitters for thermophotovoltaic applications, components for hypervelocity impact shields for spacecrafts and satellites, components in composite, lightweight armour systems, heat exchangers, lightweight structures (sandwich panels in which the cellular ceramic core can act both as a structural element and a functional porous medium), current collectors in Solid Oxide Fuel Cells, acoustic liner in mufflers for general aviation aircraft and substrates for bacteria immobilization (for the purification of water in fish tanks through wet/dry biofiltration or for aerobic waste water treatment (containing various organics, non-toxic solvents and various salts).

In the following sections Polymer-Derived Porous Structures will be discussed in depth, focusing on the most novel techniques develpoed. The use of PDCs to produce porous structures is very advantageous mainly because of the lower processing temperatures (800-1200°C) than conventional powders processing. Moreover it is

possible to apply conventional plastic forming technologies, generally with low processing costs, to the realization of ceramic products[4].

1.2 Polymer-Derived Ceramics (PDCs)

Organosilicon polymers materials have an universal place in our daily life due to their specific properties such as low weight, mechanical strenght and processability[5]. Moreover they find widespread applications (Figure 1.3) as ceramics precursors (ceramic heaters[**], coatings[6], C/C/SiC brakes for motorbikes[*], MEMS[7], SiOC ceramic foams[8,9], SiOC precision components[10], Polymer-derived ceramic fibers[11]), mainly because they possess improved properties compared to the conventional ceramic materials, such as their specific electrical, thermal, chemical, mechanical and biological properties.

The first example of polymer-derived cereamics can be traced back to the 1970s, when carbosilanes were polymerized, drawn into fibers, and then pyrolyzed in controlled atmospheres to produce fibers of silicon carbide[12].

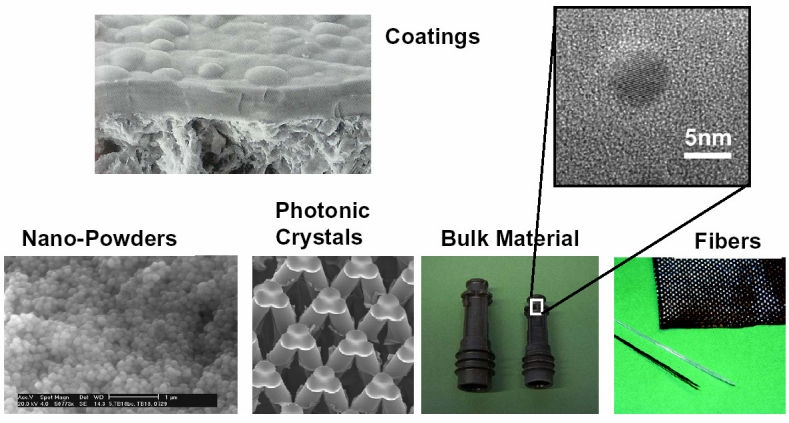

Figure 1.3- PDCs from nano to macroscale (courtesy of Dr. Ralf Hauser, Darmstadt University, D)

The chemical route to produce ceramics consists in:

[**] Robert Bosch GmbH
[*] STARBLADE™, Starfire Systems Inc., USA

- The synthesis of oligomers or polymers from low molecular compounds (precursors), which ideally possess the structural elements that are desired in the final product.
- Chemical or thermal cross-linking of the as-synthesized precursors in order to obtain high molecular compounds convertible into ceramics with high yields.
- Pyrolysis of the cross-linked polymer providing the desired ceramic material, accompanied by the formation of gaseous reaction products[13].

Si-based PDCs can be subdivided into three main groups: (1) silicones and polysilsesquioxanes, as precursors for SiOC ceramics when processed under N_2 or Ar, (2) polysilanes and polycarbosilanes, as precursors for SiC ceramics and (3) polysilazanes that give after pyrolysis SiCN materials:

1) $[-R^1R^2Si-O-]_n$, $[RSiO_{1.5}]_n$ **2)** $[-R^1R^2Si-]_n$, $[-R^1R^2Si-CH_2-]_n$ **3)**$[-R^1R^2Si-NH-]_n$

where R= H, R^1= CH_3, R^2= C_6H_5 (Phenyl) or CH= CH_2 (vinyil)

The ceramic composition can be designed starting from the polymer structure and materials in a binary, ternary and quaternary system can be produced. SiC, SiN, SiOC, SiCN, SiECN, SiECO (where E= B, Al) and SiOCN are typical polymer derived ceramics.

Chloro-organosilicon compounds are important starting materials for the synthesis of polysilanes, polycarbosilanes, poly (organosylazanes), polyborosilazanes, polysilylcarbodiimides, polysilsequioxanes, polycarbosiloxanes and other silyl-containing polymers[14, 15, 16]. Polysiloxanes are usually inexpensive and commercially available (SiOC precursors). There are two general routes to produce polysiloxanes: the polycondensation of α, ω– functionalized linear silanes and the ring opening (ROP) of cyclic silaethers.

Synthesis of SiCN-precursors can be made starting from chlorosylanes by means of ammonolysis reactions with ammonia or aminolysis with different amines. The main disadvantage of this route is the difficult separation of the polymeric reaction product from the solid byproducts NH_4Cl or H_3NRCl. These types of reactions generally yield a mixture of oligomers and low molecular weight polymers which can easily volatilize and depolymerize giving low ceramic yields. Therefore cross-linking must be performed prior to pyrolysis.

The introduction of reactive substituents to silicon in poly (organosilazanes) and polysilylcarbodiimides such as hydrogen and vinyl groups enables the modification of the polymers with boron and aluminium for the production of the quaternary Si-E-C-N

ceramics (E= B, Al). Similar to the findings in the field of SiCN-derived ceramics, the insertion of aluminium or boron in polysiloxanes is expected to provide a higher temperature and oxidation resistance to SiOC ceramics derived therefrom.The ceramic structure, composition and properties are deeply affected by the cross-linking reactions.

This step is often necessary to improve the polymer yield and the ceramic material properties. Covalent bonds are formed among the low molecular weight chains and gas evolution is recordered. These gases are generally condensation products and residues of synthesis reactions. The cross-linking reactions can be processed chemically, by addition of catalysts such as ammonia or Zr-acetylacetonate for polysiloxanes, and Acetonitrile for polysilazane, and-or thermally like warm-pressing or photo-curing. These techniques will be discussed more in datail in Chapter 2.

The polymer to ceramic conversion can be obtained thermally (pyrolysis) or non-thermally (ion irradiation).

Pyrolysis can be performed via conventional oven annealing[17] or by microwave[18] or laser heating[19].

The conventional oven annealing to process the polymer-to-ceramic conversion generally consists in a heat treatement under inert atmosphere (nitrogen or argon) up to 800-1200°C. This procedure is widely used eventhough to produce bulk PDCs components it is sometimes replaced by Hot Isostatic Pressing. By this route, high pressure combined to high temperature gives fully dense ceramics. The evolution of gases starts generally at temperature around 400°C and porosity is formed.

At higher temperatures pores collapse and at temperatures above 1000°C the porosity is completly filled by the ceramic solid phase. High pressure prevents the formation of micro pores in the early stage of pyrolysis, giving a more homogeneus, fully dense ceramic.

The Ion Irradiation treatement is controlled by two key parameters: the linear density of energy transfererd to electron shells, and the ratio of this energy density to that used to diplace atoms.

The pyrolytic conversion into thermodynamically stable compounds, namely SiC, turbostratic graphite and silica, requires long-range rearrangements which are possible only at very high temperatures. This redistribuition reactions without changes in the composition, compete with other reactions, such as the oxidation of polycarbosilanes leading to the formation of insulating layers around $SiCH_x$ islands, and the evolution of various stable organic molecules with sequences and rates depending on the heat cycle and atmosphere (gas nature and pressure). On the contrary, the high amount of energy transferred locally to electronic shells during ion irradiation promotes an out of equilibrium chemistry, characterized by the formation of

many free readicals in a fraction of picosecond and their combination at random (like in a very localized thermal spike)[20].

The polymer-to-ceramic conversion leads to high shrinkage during the thermolysis, due to the elimination of organic moietis and gases evolution. As a consequence structures with cracks and pores are produced and mechanical strenght is negatively affected.

The addition of fillers can prevent the cracks formation during thermolysis. This process can be performed in two different ways: 1) Polymer with passive filler, 2) Polymer with active fillers.

In the case of processing polymer with passive fillers, no reactions occur between the filler and the matrix and cracks formation is prevented because the filler limits the shrinkage of the material. As passive fillers, different metal carbide and nitride can be used. In the case of active fillers , metals or intermetallic compounds react with the matrix and/or the volatile compounds of thermolysis, producing nitrides or carbides. Active fillers during pyrolysis react with the matrix and expand giving near net-shape components (again reducing the shrinkage occuring in the material).

Oxide fillers can react with Si-based ceramic polymers to form complex oxides such as mullite, cordierite, wollastonite, SiAlON, etc.

By the addition of active fillers new properties such as , magnetic, electrical properties can be introduced in the component. Moreover it is possible to decrease shrinkage and porosity.

The microstructure of PDCs after pyrolysis is subject to fervent debates among scientists since there are some difficulties in investigating their structure. Some models have been developed[21-30]. From a macroscale point of view they can be defined as amorphous ceramics when pyrolyzed at temperature lower than their crystallization temperature, however high resolution analysis reveals the presence of nanodomain structures. TEM, SAXS, solid state NMR combined with etching in the case of oxide-ceramics[21,22,23] are the tecniques used to detect their structure.

In Table 1.2 a comparison of the properties of PDCs with SiO_2 and SiC are reported.

Table 1.2- Properties comparison of PDCs ceramics and conventional SiC, SiO_2 and Si_3N_4

Composition	Density (g/cc)	CTE 1000°-100°C (10^{-6} K^{-1})	Glass Transition T (@10^{13}Poise) (°C)	E (GPa)	Ref.
SiC	3.2	4.3	-	482	[24]
SiC	2.32-2.55	3.1-4	-	190-270	[25] [26]
SiOC	2.35	3.14	1350	97.9	[27]
SiO_2	2.2	0.5	1190	70	[27]
SiCN	2.35	3	1350	80-225	[28]
Si_3N_4	3.2	2.85-3.2	-	55-214	[24]

Riedel et al.[28] (Table1.3) report chemical structure and related properties of SiCO and SiCN ceramics.

Table1.3- A summary of the Structural and High-Temperature properties of SiCN and SiOC Polymer-Derived Ceramics [28].

Molecular And nanostructure	SiCN	Technique	SiOC	Technique
Si Atoms	Tetrahedrally bonded to C and N	NMR SAXS	Tetrahedrally bonded to C and O	NMR
C Atoms	→ sp^3 when bonded to Si → sp^2 when bonded to other C atoms → Not bonded to N	NMR	→ sp^3 when bonded to Si → sp^2 when bonded to other C atoms	NMR
Size of Nanodomains	1-2 nm gradually increasing in size with annealing	SAXS and SANS	1-2 nm is size increasing in size with annealing	SAXS and HF etching
High temperature Proerties	**SiCN(B)**		**SiCO**	
Creep	Negligeble steady-state creep up to 1550℃. Powders impervious to solid state sintering without additives.		Negligeble steady-state creep up to 1300℃. Powders impervious to solid state sintering without additives.	
Crystallization	SiCN resists crystallization of SiC up to 1400℃ and SiBCN up to 1600℃		Resists crystallization of SiC and SiOC up to 1300℃	
Oxidation	Oxidation resistance similar to the best known resistance in crystalline materials, i.e. CVD silicon nitride and silicone carbide.		Despite the presence of high amounts of carbon (near one third molar), the oxidation resistance suggests carbon activity is much less than unity	
Decomposition	In Ar, SiCN is stable up to 1450℃ and SiBCN up to 2000℃ (Si_3N_4 decomposes at 1400℃)		Decomposes in inert atmosphere at 1350-1450℃ due to carbothermal reduction reactions.	

In the analyzed cases, the amorphous phases are formed in carbon-rich regimes, relative to the stochiometric mixtures of the crystalline forms. A key question in understanding the transformation of the polymeric state to the nanostructured ceramic is the role of “free” carbon. The introduction of elements such as boron or aluminium improve thermal and mechanical stability. These properties of PDCs are typical for the amorphous state which can persist up to 1800℃.

Saha et al.[29] define the SiOC structure using a multidomains model based on three constituents: clusters of silica tetrahedra that form the heart of the domain , the

sorrounding monolayer of mixed bonds of the type $SiO_{4-n}C_n$ where n gives the fourfold coordination of silicon to carbon and oxygen, and the graphene cage-like network that encases the domains. In accordance with Riedel[23] the carbon bonded to silicon assumes a sp^3 coordination and the carbon in graphene is sp^2 or graphitic carbon.
The nanodomains characterization of SiCN ceramics has also been recently reported[30], however chemical informations about the composition of these nanodomains is not yet understood.
In the next sections more attention will be given to the formation of porous structures by mean of preceramic polymers.

1.3 Ceramic Foams

Ceramic foams are a specific class of porous materials that consists of a three-dimensional array of polyhedral cells, with average linear dimension ranging from 10 μm to some mm, packed to fill space and possessing a geometry that, when isotropic, can be approximated to that of a tetrakaidecahedron[31].The actual cell shape however depends on several factors, including the fabrication process.
According to Gibson and Asbhy[26], one can properly speak of foams only when the relative density of the material is ≤0.3, while for higher densities it should be classified as a generic (macro) porous material. Cells can be surrounded by ceramic walls (randomly oriented in space) or the solid can be contained only in the cell edges (struts). If present in the cell walls pores (cell-windows), create an interconnected structure (open-cells foams).
Current commercially available ceramic foams include compositions such as allumina, zirconia, cordierite, mullite, silica, silicon carbide and hydroxyapatite.
Depending on their morphology (e.g. open *vs* closed cells, pores size distribuition) they can find applications as: filters (molten metals[32], particulate from diesel exhaust gases[33]) radiant burners, catalyst support, biomedical devices, kiln furniture, reinforcement for metal matrix composites, bioreactors, thermal protections systems, supports for space mirrors, components in solid oxide fuel cells, light weight sandwich structure, heat exchangers (graphite foams) etc.
The advantages of using porous ceramics in these applications are usually the high melting point, tailored electronic properties, high corrosion and wear resistance in combination with the features gained by the replacement of solid material by voids in the component. Such features include low thermal mass, low thermal conductivity, controlled permeability, high surface area, low density, high specific strength, and low dielectric constant[34].

Presently three main processes to fabricate ceramic foams have been developed.
In the 1960s Shwartzwalder and Somers[35] used polymeric sponges as tamplate for cellular ceramics. Since then the replica technique has been widely used and developed. The process consist on impregnating a cellular structure by a ceramic suspansion of appropriate viscosity, drying of the ceramic suspansion and burn-out of the sponge in order to obtain a ceramic exhibiting the same morphology as the original porous material. Templates can be synthetic (typically polyurethane, but also vitreous carbon) or natural (such as coral and wood). This technique offers a great flexibilty since it can be extended to any ceramic material that can be properly dispersed into a suspansion.
The typical morphology obtained by the replica technique is a very open reticulated foam (the solid is all contained in the struts) with porosity varying from 40-95% and pores with sizes approximately between 200 μm and 3 mm. The high pore interconnectivity make these foams the ideal candidates for filtration purposes.
The main disadvantage of this approach is related to the sponge burn-out that leaves cracked and hollow struts, that can compromise the mechanical strength of the final material.
As a consequence many attempts have been made in order to avoid this shortcoming by improving the wetting of the suspansion with the help of additives, adding a second step to fill cracks in the struts, introducing fibers or reactive compounds.
A variation of the replica technique is a process where the polymeric template is not burned out but pyrolysed to yield a pyrolytic carbon skeleton that can then be coated by a ceramic material, generally using Chemical Vapour Deposition. The resulting structure is completely open cell with dense struts comprised of a carbon core and an external layer – typically 10 to 1000 μm thick - of the selected material (oxide, nitride, carbide ceramics as well as borides, silicides and metals).
More recently the use of preceramic-polymers (PP) instead of the ceramic suspansion has been introduced by Bao et al.[36] The interaction between the PU sponge and the PP seems to be more attractive for this kind of technique (improved wetting of the sponge, partial melting of the cross-linked polymer during pyrolysis) since during the PU burning-out the PP shrinks and the typical hollow and damaged struts are not observed[37].
The second basic approach relies on foaming a ceramic slurry by using a blowing agent (that can be a voltaile liquid, combustible solid particles, a gas produced by reactions in the mixture or added to it). In most cases, the consolidated foams are afterwards sintered at high temperatures to improve mechanical properties.
In this approach the porosity is proportional to the amount of gas incorporated into the suspansion or liquid medium during the foaming process, while the pores size is related to the stability of the wet foam. Since the wet foam is a thermodynamically

unstable system (where bubbles grow and coarse) the most critical issue on direct foaming process is the approach used to stabilize the air bubbles incorporated within the initial suspansion or liquid medium. Stabilization can be performed by use of surfactants or particles.

The use of surfactants like long-chain amphiphilic molecules (e.g. lipids and proteins) presents the main disadvantage related to the low adsorption energy of surfactants at the gas-liquid interface. Therefore the use of such long-chain surfactants cannot prevent the long-term destabilization of foams. Therefore the use of surfactants in the direct-foaming process ask for setting agent to consolidate the foam microstructure. By this route only small pores size can be obtained (~50μm)[34]. In the 1970s Wood et al.[38] following the success of the polymer replica technique, incorporated ceramic particles into organic solutions containing precursors of polyurethane foam. By the in situ evolution of gases damaged struts are avoided. Moreover the use of this technique can also be extended to inorganic materials that present a sol-gel phase transition in liquid medium. However it has been predominantly applied to silica-based systems[39].

On the other hand the use of particles as stabilizers allow a long-term wet foam stability, giving a wider range of porosity (40-93%) and pores size ranging from 10 to 300 μm[34].

This approach probably yields the widest range of cellular structures and hence properties, but they are generally less open than the replicated foams. Moreover these processing routes can give a gradient pores size due to the effect of the blowing agent.

The final approach relies on the incorporation of sacrificial additives in the form of beads and related materials[40].

This technique typically consists in the preparation of a biphasic composite, consisting of a continuous ceramic matrix where a second phase is continuosly dispersed. The second phase will act as sacrificial template that will be burned-out to give the final porosity.

This approach seems to be very versatile since the foam morphology (porosity, pores size and distrinbuition, open- *vs* closed-cell) can be tailored adjusting the amount of sacrificial template and the final material composition can be chosen starting from the ceramic powders.

Typical values for porosity can range from 20%-90% and pores size from 1-700 μm, with typically isotropic structure and properties.

In this case, the most critical step is related to the sacrificial fillers burn-out; since it gives gas realese, structures based on ceramic powders must possess enough mechanical strenght in order to prevent the foam collpase (in the worst case) or to

retain the sacrificial filler shape.The sacrificial filler burn-out is generally realized during sinterization or pyrolysis.

A wide variety of sacrificial materials have been used as pore formers, including natural and synthetic organics, salts, liquids, metals and ceramic compounds.

As a consequence many ceramic powders-sacrificial templates systems have been developed (Y_2O_3 stabilized ZrO_2-starch[41], TiO_2 or SiO_2-volatile oils or water[42,43,44]) .

The need to control all these parameters has given a great impulse to researchers, however still no one route is sufficiently flexible to yield all the necessary structures[45].

Unconventional techniques have been developed in the last years and they include the use of volatile or combustible additives that are lost during firing, CVD deposition of various refractory materials on a foamed carbon skeleton[46]; sintering of hollow spheres[47]; SiO gas reaction or siliciding of carbon preforms[48]. One particular approach for forming porous ceramics used starch as both binder and pore former[49]. It is well known that satrches can act as binders due to their gelling ability in water[50], but during firing they result in residual porosity.

Inorganic pore formers can also be used; these include alkaline earth metals and their oxides, as well as a range of other oxides, nitrides and carbides. The mineral perlite is also commonly used. After forming and drying, the green bodies are fired, and the pore formers partially or completely melt and/or react with the ceramic powder.

In Figure 1.4 a microstructural comparison of ceramic foams produced by diffrent processing routes is reported.

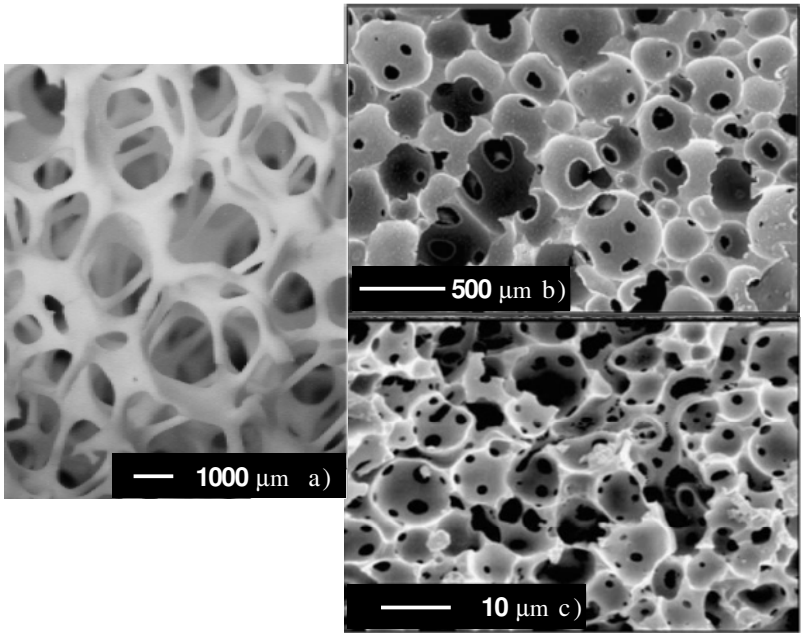

Figure 1.4- Typical microstructure of ceramic foams: a) macrocellular Al_2O_3 replica; b) macrocellular SiOC directly foamed ceramic; c) microcellular SiOC from PMMA burnout.

In this section the manufacturing of Polymer-Derived macro and microcellular ceramic foams using unconventional techniques will be discussed.
As described before,the definition for macro and microcellular structures is based on cells size and cell density.

1.3.1 Macrocellular Ceramic Foams

Macrocellular foams tipically present cell size larger than 50 μm and cell densities < 10^9 cells/cm^3.
As previously reported, Bao et al. realized macrocellular ceramic foams coating a PU sponge by mean of preceramic polymers instead of a ceramic slurry. By this route they produced macrodefects free struts in a macrocellular interconnected SiC foams. Moreover adding Si_3N_4 and TiC to the starting polysilane solution they realized SiC-Si_3N_4 and SiC-TiC composite foam with the main pourpose to increase the foams strenght and their high temperature resistance[51,52].
In the patents by G. Renlund, W. Minnear and A. Bracco[53,54] a siloxane solid resin was mixed with polyurethane precursors to prepare macrocellular ceramic foams. Their work was followed by a patent by Daws et al.[55], which employs foaming of a phenolic resin and a siloxane liquid precursor.
Colombo et al.[56] investigated in depth this new route consisting of co-blowing a silicon resin and polyurethane (PU) precursors. In the work reported in [56], a methyl (polysiloxane) was mixed with precursors for polyurethane (polyols and isocyanates) in dichloromethane (with the addition of surfactants and catalysts). Blowing was started by vigorous stirring at a controlled temperature (25-40 °C).
The choice of PU precursors, the amount of solvent and the type and amount of surfactants influenced the viscosity of the mixture and the final foam architecture (open vs closed cells) and characteristics (bulk density), while the type and amount of catalysts controlled the rising profile of the foam and yield the crosslinking of the silicon resin. During blowing, the PU phase separated (due to immiscibility with the preceramic polymer) into small islands (typical dimensions before pyrolysis 50-300 μm) embedded within a preceramic polymer matrix, but during the early stages of foaming its presence controlled the resulting green foam morphology and characteristics[57]. Upon pyrolysis, the silicone resin converted into a SiOC amorphous ceramic, while the PU decomposed almost completely, leaving some residual carbon within the cearmic. Because the material was obtained from direct foaming process,

that is from the nucleation of gas bubbles within a liquid which tend to grow and coalesce[58], a large dispersion in cell size was observed. The average cell size, for this foam possessing a bulk density of 0.47 g/cm^3, was 230-310 μm. The struts were dense and the structure appeared generally to be without defects[59].

Recently, studies have shown the possibility to foam poly(siloxane) without an additional polyurethane foaming agent[60,61] . In this case, foaming is due to the evaporation of by-products of the cross-linking reaction (water).

A phenyl methyl poly(silsequioxane) containing small amounts of ethoxy and hydroxy groups was foamed by an in situ blowing technique. When heated above 200 °C, condensation reactions occured releasing water and ethanol and then triggering the pore formation in the polymer. So water and ethanol deriving from condensation reactions during the polymer curing, act as foaming agents and the foam structure is stabilized by the concurrent viscosity increase with proceeding cure of the polymer melt.

With increasing degree of curing, e.g. increasing the number of Si-O-Si intermolecular cross links, the viscosity of the polymer increased thereby stabilizing the transient foam structure. Variation of the degree of curing was then used to tailor cell size, strut thickness and interconnectivity of the pores.

Moreover the microstructure can be tailored to optimize the mechanical, magnetic and electrical properties by loading the polymer with reactive or inert filler particles[62].For istance quartz powders[63] can be added to the system in order to decrease the linear shrinkage after pyrolysis or $MoSi_2$, Cu_2O, SiC, C particles can be added in order to tailor electrical properties[64]. Moreover polymer-derived ceramic foams can be infiltrated with Mg or Al alloy applying squeeze casting process in a carbon dioxide atmosphere[57]. The addition of such alloyes allow to produce Interpenetrating Phase Composites (IPCs).

The beginning of the IPCs concept rise from the shortcoming deriving from the large shrinkage occuring during pyrolysis of PP. As previously reported shrinkage results from the escape of low molecular weight gases. The need for these atoms to escape via solid-state diffusion limits ceramics produced by this method to sizes of the order of micrometres if the resulting material is to be pore free.

This limitation is circumvented if the polymer derived ceramics are used to produce the reinforcing phase of a large composite material. In the form of a fine reinforcing phase, conversion of the polymer to a ceramic can take place with easy escape of volatile species, after which the resulting material is used to fabricate a large and fully dense composite material. For this reason, polymer-derived SiC has been largely produced and commercialized in the form of fine reinforcing fibers, such as the Nicalon™ fibers produced by Nippon Carbon in Japan.

The use of open-cell ceramic foams improves the final composite material properties. In the IPCs both phases, the matrix and the reinforcement phase, form an interconnected interpenetrating network structure[65], as opposed to usual composites in which the reinforcemnt takes the form of isolated fibers, whiskers or particles.

IPCs promise significantly higher poroperties improvement compared to conventional composite materials.

Although limited to silicon containing preceramic polymers, the polymer derived foams offer a higher interconnectivity of the cells and a higher isotropy of the cell arrangement compared to the conventional ceramic foaming techniques.

Moreover the regulation of the crosslinking time and temperature allow to manifacture foams with gradient porosity, in one fabrication step.

Pore gradient ceramics offer an interesting potential for being used as biocompatible implants, preforms for liquid metal infiltration, thermal barrier coatings and thermal shock resistance. However, the fabrication of porous ceramics with graded porosity (using conventional techniques) is more sophisticated as compared to isotropic ceramic foams and usually requires multiple manufacturing steps[66].

In Figure 1.5 a 3D tomography recostruction of a sample possessing graded porosity.is reported.

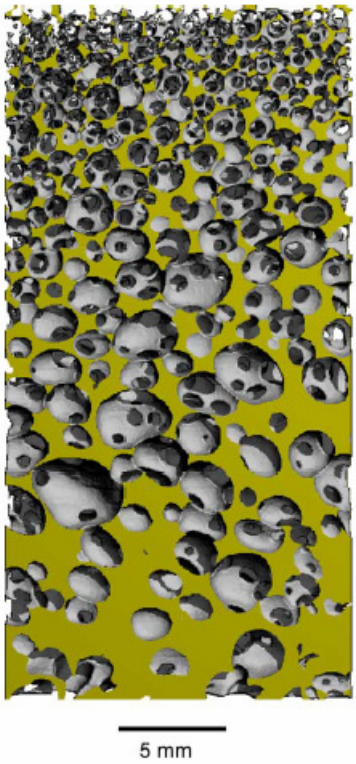

Figure 1.5- 3D tomography reconstruction of a foam possessing graded porosity [66]

In Table 1.4 an overview of the compositions and morphologies that can be obtained using preceramic polymer to produce ceramic foams is reported.

The above mentioned techniques make preceramic polymers very attractive for the production of macrocellular ceramic foams. This is due to the higher versatility and the easier production route (compared to conventional techniques) that allow the tailoring of the final material properties.

Table 1.4- Overview of the produced ceramic foams starting from a Preceramic Polymer

Composition	Cell-size	Morphology	Processing Route	Ref.
SiOC	230-410μm	Open	PP-PU direct foaming	[56]
	1-1.6 mm	Graded porosity	PP direct foaming,	[66]
	500μm-2 mm		PP-PU direct foaming	[8]
	1-80μm	Open and closed	UEXP templates, CO_2, PMMA templates	[73] [74] [78] [79] [71] [67]
SiC	400-900μm	Open	PP-PU replica	[36]
	<30 μm	Open	UEXP templates CO_2	[72] [75] [81]
	10-100 μm	Open	Salt compact replica	[71]
	80-660 nm	Open	PP-colloidal SiO_2 templates	[84]
$3Al_2O_3*2SiO_2$	<20 μm	Partially open	UEXP templates	[76]
$2MgO*2Al_2O_3*5SiO_2$	45-55 μm	Open	UEXP templates	[77]
SiOC+Fe/Ni/Co SiOC+C SiOC+SiC	>50 μm	Open	PP-PU and PP direct foaming	[64]
$SiC+Si_3N_4$			PP-PU replica	[51]
SiC+TiC			PP-PU replica	[52]

1.3.2 Microcellular Ceramic Foams

Microcellular (plastic) foams were developed by Suh et al.[68] in the 1980s as a means to reduce the amount of polymers used to make plastic parts without damaging their appearence or usability, and since then low density microcellular materials (LDMMs) have attracted considerable interest because of their unique morphology and structure-property relationship. In addition to cost saving, microcellular plastics have a lower thermal conductivity and density, higher impact strength, toughness and fatigue life than dense plastics. Tipically, microcellular plastic foams have closed cells, with cell densities greater than 10^9 cells/cm^3 and fully grown cells smaller than 50 μm[69].

The use of a preceramic polymer to produce microcellular ceramic foams takes advantage of the low cost process, since it is possible to apply conventional plastic forming technologies (injection molding, extrusion, resin transfer molding, melt spinning...).

Moreover, it has been recently demonstarted the possibility to control the porosity percentage and the cells density by different routes.

In 1995 Fitzgerald et al.[70] reported the production of fine open-celled ceramic foams starting with a commercially available polysiloxane. In this process, a sodium chloride compact formed by sintering was first infiltrated with molten polycarbosilane under applied pressure. After dissolution of the salt, the resulting polymer foam was cured by oxidation in air and pyrolysed to form a silicon carbide foam. Cells size down to 10 μm were produced in this manner, however the process was quite laborious in terms of time (several weeks).

The use of polymeric microspheres as sacrificial fillers to induce the porosity inside the material is nowadays a quite well-known technique.This research group has recently developed open-cells, microcellular SiOC foams starting from a polysiloxane, as ceramic precursor, and poly-methilmetacrylate microbeads as porosity source[71].

This procedure will be discussed in detail in Chapter 2.

Kim et al.[72,73] have developed closed-cells SiOC microcellular ceramic foams by mean of expandable or unexpandable hollow plastic microspheres mixed to a commercially available polyalkylsiloxane. This pores source consists of poly-methyilmethacrylate shells containing hydrocarbon gas. Increasing temperature, the pressure inside the shells increases inducing the softened spheres expansion.

Since the porosity percentage, the pores morphology and their degree of interconnectivity are the parameters that must be controlled, the effect of the amount of microspheres used, their expansion temperature and the pre-ceramic polymer degree of crosslinking have been studied. Using both expanded and unexpanded microspheres they obtained closed-cell SiOC foams. The use of unexpanded microspheres (30-70wt.%) created closed porosity since difficulties releated to the good control on expansion process. However only closed-cell foams were obtained, using expanded microspheres up to 90 wt.%, that is a very high amount of powders considering their low density value (0.9 g/cc).

On the other hand open-cell SiC microcellular foams heve been produced, starting from a mixture of polysiloxane, phenol resin or carbon black (as carbon source) and expandable microspheres (60-80 wt.%). After pyrolisis at 1200°C the SiOC+C foam was converted to SiC by carbothermal reduction at 1650°C under argon atmosphere[74,75].

Since the responsable of interconnection among cells is considered the amount of sacrificial templetes added to the mixture, one should expect interconnection among cells using 90wt.% of already expanded microbeads in SiOC foams. On the other hand SiC foams produced by the same route possess a high degree of interconnectivity, even though the templates used were expandable. The reason of

this discrepancy could lay in the carbothermal reduction step (added to convert the SiOC+C system to SiC).

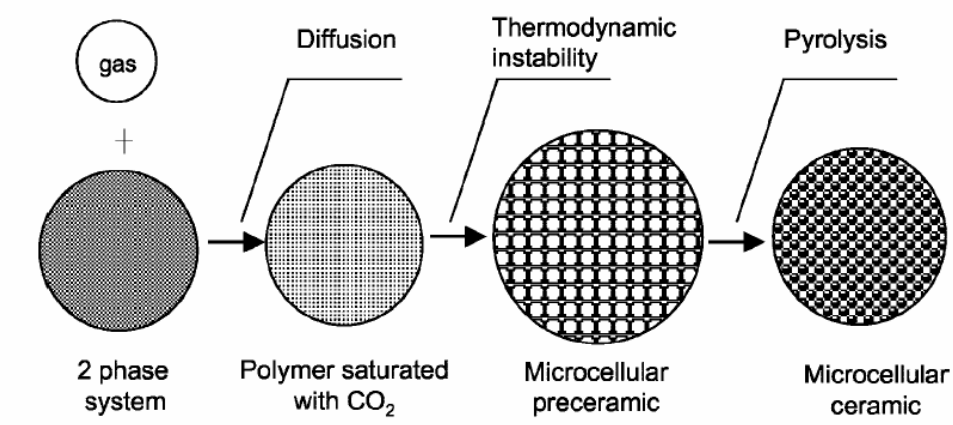

Figure 1.6- Morphology change of preceramic polymer and gaseous CO_2 system during processing of microcellular ceramic.

Pre-ceramic polymer can also be used to produce porous structures with different composition, such as cordierite[76] or mullite ceramics[77], by simply adding fillers or precursors which will produce the final composition upon heating and sintering.

For istance, burning a polysiloxane in air at 700°C, SiO_2 is produced; adding to the starting mixture talc, Al_2O_3 and expandable microspheres and sintering at 1325°C a microcellular cordierite ceramic can be obtained.

One more unconventional technique consists in saturating the preceramic-polymer after shaping at high pressures (340 MPa) by gaseous, liquid or supercritical CO_2. After saturation is reached, a thermodynamic instability is induced by a fast pressure drop or heating. Once the thermodynamic instability is induced, microvoids start nucleating and growing inside the material. After foaming the polymer is pyrolyzed and eventually sintered in order to improve its properties (Figure 1.6).

In this process several parameters affect the final material properties, such as cell density, morphology and strenght.

Since the solubility of CO_2 in the polymer is controlled by T and P, under these thermodynamic conditions the pre-ceramic polymer's chemical-physical properties can be deeply affected , such as lowering its softening point. This means that the pre-ceramic polymer used, its degree of cross-inking (temperature, time and presence of catalyst), the saturation conditions of the green samples, the pressures-drop rates and the sintering conditions all contribute to a particular set of properties.

Kim et al.[78,79] have shown how density cells can be increased, keeping the saturation T and P and the pressure-drop rate constant, by changing the ceramic precursor. If the polymer softening temperature is lowered by the saturation conditions then the

polymer collapse during the foaming step. In this case it is necessary to add to the polymer a further polymer whose softening point is not lowered by the specific

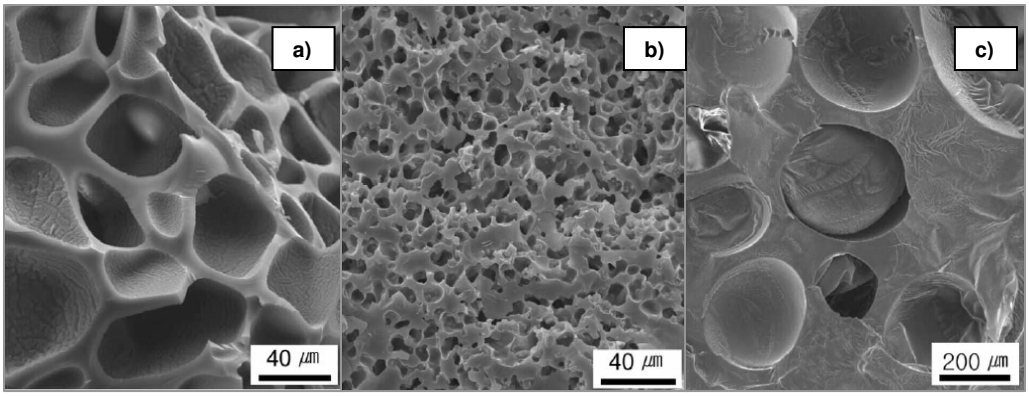

Figure 1.7- The effect of CO_2 infiltration conditions on foam morphology: (a) PS saturated at R.T. for 24 h under 5.5 MPa of CO_2, (b) PCS saturated at 50°C for 24 h under 8.3 MPa of CO2, and (c) PCS saturated at R.T. for 24 h under 5.5 MPa of CO_2 and foamed at 200°C for 3 s. The pressure drop rate was fixed as 1.37 MPa/s and 24 h, respectively, for all specimens[80].

saturation conditions. So the optimal temperature for foaming must be kept between the softening and melting temperature of the polymer.

On the other hand keeping the polymer fixed, but changing saturation and pressure-drop conditions, the porous ceramic can deeply vary its morphology and porosity (Figure 1.7).

For istance saturation under liquid CO_2 has given closed-cell of avarage size of 50 μm compared to open-cell CO_2 of 2 μm average size[80].

Nevertheless still some points are under investigation such as the crosslinking effect on porosity. What seems to be demonstrated is that increasing the degree of crosslinking of the polymer, the CO_2 solubility decreases and consequently the amount of porosity that can be produced by inducing a thermodynamic instability decreases as well. However the eventual addition of a catalyst in the crosslinking step has effects on CO_2 solubility that are still under investigation.

A further improvement of the technique consist of adding a second phase in the starting polymer (for istance polyolefine, LDPE)[81]. Since the foaming process under CO_2 saturation is governed by the nucleation and growth of microvoids, the presence of a dispersed second phase is responsable of hetherogeneous nucleation. In this case the complex viscosity ratio between the LDPE and the preceramic polymer must be carefully controlled in order to obtain a homogeneous and interconnected dispersion. In the work developed by Kim et al. keeping the polyolefine concentration lower than 10% the viscosity ratio resulted in a uniform dispersion of drops of polyolefine inside the polymer matrix, so inducing the formation of a homogeneous

open cells structure. By this technique Kim and co-workers prepared foams possessing a cell density in the range 2-4*10^8 cells/cm^3 and cell size <30μm.
One further method to produce macroporous polymer-derived SiC was reported by Sung et al.[82]. In ths work, a solution of polymethilsilane in THF was used as SiC precursor, while porosity was induced by colloidal silica spheres. After pyrolysis silica spheres were removed by etching the composite material. By this route a high specific surface area material was produced (150-172 m^2/g).
In Table 1.4 an overview of the available microcellular ceramic foams is reported.

1.4 High Specific Surface Area (SSA) PDCs

The densification process of PDCs during pyrolysis is subject to considerable attention. Since difficulties are still present in producing fully bulk components of large dimensions, the complete understanding of the phenomenological behavior of the polymer to ceramic conversion is necessary in order to grant the process reproducibility asked by industrial applications.
On the other hand, recent studies have shown how pyrolysis stopped at appropriate temperatures can lead to a controlled amount of pores in the final material. This amount of open porosity results in high specific surface area ceramic materials and new challenging applications have started to involve PDCs (e.g. gas adsorption-desorption, catalysis, membranes ecc.).
Pure and chemically modified silicas -in porous, high-surface-areas forms- are widely used as catalysts, adsorbents, and supports for heterogeneus metal catalysts. Numerous examples of modifications made to pure silica for specific applications have been reported in the leterature. These include chemically-mixed oxide systems, e.g. silica-zirconia, silica-titania and silica-alumina, as well as monolayer coatings of titania and lanthana on silica for use as catalyst supports[83,84,85]. Yet another example is provided by the synthesis of mixed adsorbents, where the useful properties of porous inorganic materials (e.g. silica, alumina and titania gels) are combined with those of active carbons[86]. These “mixed” materials, e.g. silica-carbon gels, display better adsorption properties than the values predicted by assuming additivity of properties of the individual components. Various processing routes have been developed to take advantage of this synergism.
The synthesis of silicon oxycarbide glasses, through a partial sobstitution of oxygen atoms by carbon atoms, has attracted much attention as a way to improve the thermal and mechanical properties of silica.

Oxycarbide glasses can provide (i) a homegeneously distributed source of carbon atoms for pyrolitic generation of a disperesed carbon phase in porous silica, (ii) a porous support that is thermally more stable than pure silica, (iii) a porous support that enhances the dispersion and/or activity of a supported metal catalyst, or a (iv) unique catalyst system or absorbent, per se[87].

SiOC glasses synthesized by the sol-gel route can retain their high SSA values up to pyrolysis temperatures of 800°C. However by varying the precursors these values can be retained up to much higher temperature ranges. Pantano et al.[87,88] realized high SSA SiOC glasses by sol-gel technique. Pores size distribuition and SSA values were tailored as funcution of the chemical sol-gel synthesis and by controlling crosslinking reactions and pyrolysis time and temperature. Phenyltrimethoxysilane (PhTMS) was hydrolyzed with tetramethoxysilane (TEOS) to make aerogels and xerogels. Further pyrolysis in inert atmosphere up to 1500°C led to porous SiC/SiOC glasses. Highly porous SiC/SiOC pssessing SSA of 581 m^2/g were formed at temperatures of 1000°C. Pyrolyzing pure PhTMS, highly porous SiC/SiOC aerogels possessing SSA of 400-500 m^2/g after pyrolysis up to 1400-1500°C were produced. The high SSA values, apparently resulted from free carbon formed from the free carbon atoms present in the benzene ring and subsequent carbothermic reactions with SiO_2 to form SiC.

PDCs substantially differ from materials having the same compositions, but synthesized by the sol-gel route. The sol-gel process involves the hydrolysis, condensation and low temperature pyrolysis of polymeric precursors that can be molecularly designed to provide buildings blocks for the desired material structure. A dried xerogel is usually a microporous material.

Preceramic polymers can be both synthesized and commercially available. In order to answer to the need for new adsorpents possessing more stability than the ones available, the use of commercially available preceramic polymers is favourable.

The polymer to ceramic conversion can be explained as a three steps process. Temperatures defining the border lines between consecutive steps is dependent on the starting polymer characteristics. After shaping the material is usually dense and becomes porous upon heating. However, micropores can be formed after crosslinking and their presence is influenced by the molecular structure of the PP, the crosslinking process and the shaping (cold or warm-pressing).

Generally between 100°C and 450°-550°C crosslinking and structural reorganization start combined with the release of volatile low molecular Si- containing oligomers. At temperature higher than 450°-550°C organic moieties elimination start occuring (mainly hydrogen and hydrocarbons) giving rise to gas evolution. The nature of the eliminated organic groups is of course strictliy dependent on the polymer architecture. This stage is considered the responsable of the pore formation during pyrolysis. Due to variation in the viscosity of the system a critical temperature (typical for each

system) can be defined. This critical temperature is the limit for pores formation: further annealing causes pore collapse due to both the end of the gas evolution process and the increasing viscosity of the polymer derived ceramic.

The last step in the pyrolysis process can be named as densification and cristallization. At this stage (generally temperature higher than 800°C) the organic moieties have been completly removed from the chain and the ceramic material is formed. Further annealing (T>1200°C) leads to cristallization of the amorphous ceramic.

In 1990 Yao et al.[89] proposed a mathematical model for the pore formation during the pyrolysis of preceramic polymers. To describe the initiation of pore formation the classical theory of nucleation and growth and gas diffusion mechanisms were considered. The mathematical model was compared to experimental results for formation of non oxide ceramics (SiC from plycarbosilane). The model was capable to predict porosity and its distribuition which is influenced by temperature, pressure, as well as thickness, chemistry, and the physical properties of the pyrolyzing object. During the polymer to ceramic conversion supersaturation conditions are reached in the core sample, that give rise to nucleation and growth of bubbles which lead to such pore formation.

Wan et al.[90] have recently studied the porosity evolution during polymer to ceramic conversion of commercially available polyureasilazane. The crosslinking, compacting and pyrolysis temperatures effects on pores formation and densification were investigated by mean of nitrogen adsorption-desorption, mercury porosimetry combined to TEM and SEM investigations. A densification mechanism based on surface reaction and pyrolysis accomodated by viscous flow was proposed.

In this work, two kinds of pores were detected: small pores (d_{sp}< 10 nm) and large pores (d_{lp} > 200 nm). Small pores seem to be an intrisic properties of the polymer and they exhibit no volume change up to 450°C.

These pores are eliminated within the narrow temperature range 450°-600°C. As a consequence the pyrolysis of the polymer compact starts with a decrease in density until 450°C. The larger pores show an increase in volume up to 450°C; a volume decrease occurs progressively from 450° to 1040°C.

In the initial stage of pyrolysis, gas generation bulids up an internal pressure inside the pores. As demonstrated by Konetschny and Seitz[91,92], there is viscous flow of the polymer at elevated temperature and thus the internal gas pressure results in an increase in pore size and volume. This phenomenon is profound in larger pores. In smaller pores where the equilibrium pressure of the monomers or oligomers is lower, and the smaller pore size cannot provide sufficient escaping tunnel size for the relatively large monomer or oligomer molecules, bulging of pores is less significant. In smaller pores, the shorter distance between the functional groups enables reaction

pyrolysis to happen between opposite walls of the pore, which results in easy elimination of nanometric pores within the narrow temperature range of 450°-600°C.
In larger pores, the short-distance nature of the surface reaction makes it impossible for reaction to happen between opposite walls of the pore. However, reaction of functional groups and surface pyrolysis can nonetheless happen at adjacent areas of internal surfaces, preferably at locations with smaller radius of curvature. This reaction pyrolysis results in localized viscous flow as shown in Figure 1.8.; therefore, progressive densification can also happen in larger pores, although not as vigorously as in nanometric pores. Densification stops only when active functional groups are exhausted or the viscosity of the matrix material becomes too high because of ceramization.
Changing the ceramic precursor, temperature range for pore formation and densification can be modified, the same as pores dimensions.
Moreover the polymer can be designed in order to obtain a different amount of porosity and SSA by varying the CH_3/Si ratio.

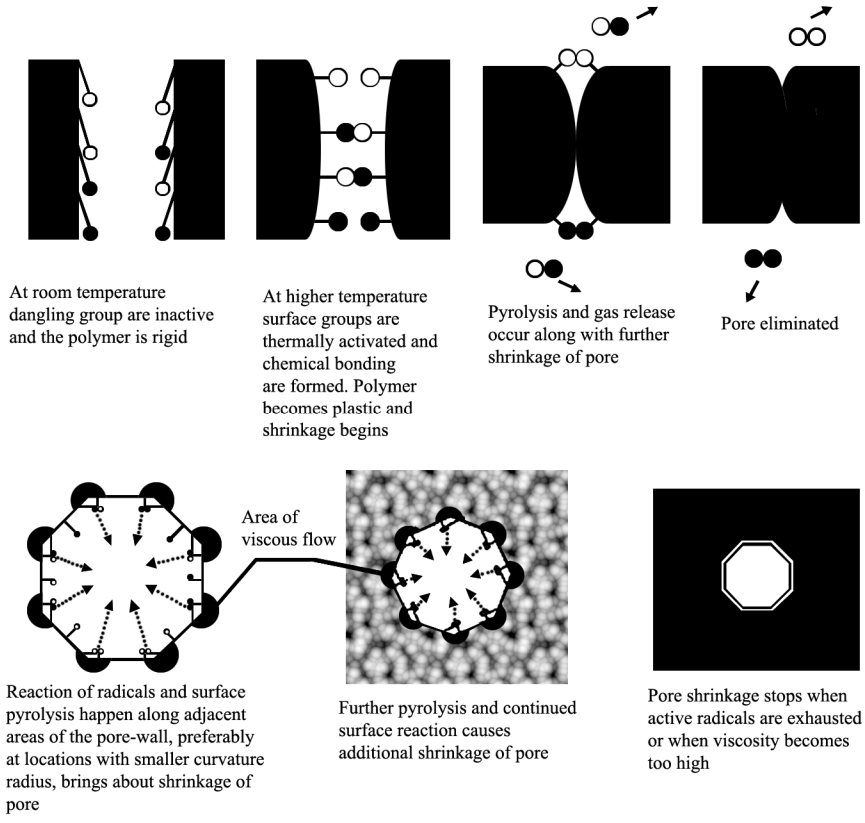

Figure 1.8- Model for densification mechanism of surface/pyrolysis accomodated by viscous flow, [90].

Schmidt et al.[93,94] studied the effect of pore channels on the pores formation during pyrolysis of polysiloxanes. The microchannels were induced by decomposition of polystirene microfibers. High Specific Surface Area (450 m^2/g) SiOC ceramic were obtained by pyrolysis up to 600°C under nitrogen flow. Further annealing up to 1000°C resulted in microporosity collapse. The presence of microchannels helped the gas realese during pyrlolysis and prevented cracks formation on large components.

However by modyifing the polysiloxane by alkylsilanes, by incorporating long-chain branches such as Methyltrimethoxysylane (MTMS) or propyltrimethoxysialne (PTMS), and moreover by the incorportaion of prepyrolized fillers, the microporosity retention beyond 1000°C with SSA of 163 m^2/g was induced. The increased gas formation by decomposition of long chain alkylsilanes supported the pore structure; moreover the presence of microchannels formed during the first step of pyrolysis by decomposition of polystirene microfibers, offered escaping ways to gas evolution. The prepyrolyzed (1000°C) fillers addiction stabilized the pores structure since they reduced viscous flow processes.

Colombo et al.[95] prepared foams with a bimodal pores size distribuition (Figure 1.9) using the direct foaming technique of in situ polymerization of PU in silicon resin (SR).

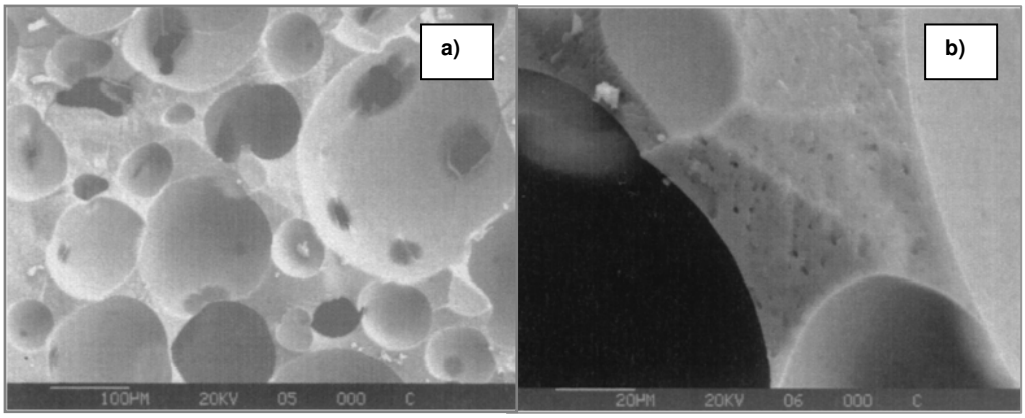

Figure 1.9- Microstructure of PP/PU foam (a) with micro-/meso-porosity (b), [95].

Varying the SR/PU weight ratio, adding activated carbon or β-SiC particles to the starting mixture, and varying the pyrolysis condition (fast and slow heating rates) they studied the effect of pyrolysis temperature on pores formation and SSA. The temperature of the highest SSA (500 m^2/g) value was 600°C (critical temperature) for all the samples, even though increasing the PU amount and the presence of fillers (activated carbon) induced pores formation and their retention up to 1200°C.

The main disadvantage in this procedure for the formation of micro and mesoporosity in PDCs is the very slow heating rate (of the order of 0.1 K/min) necessary for pores

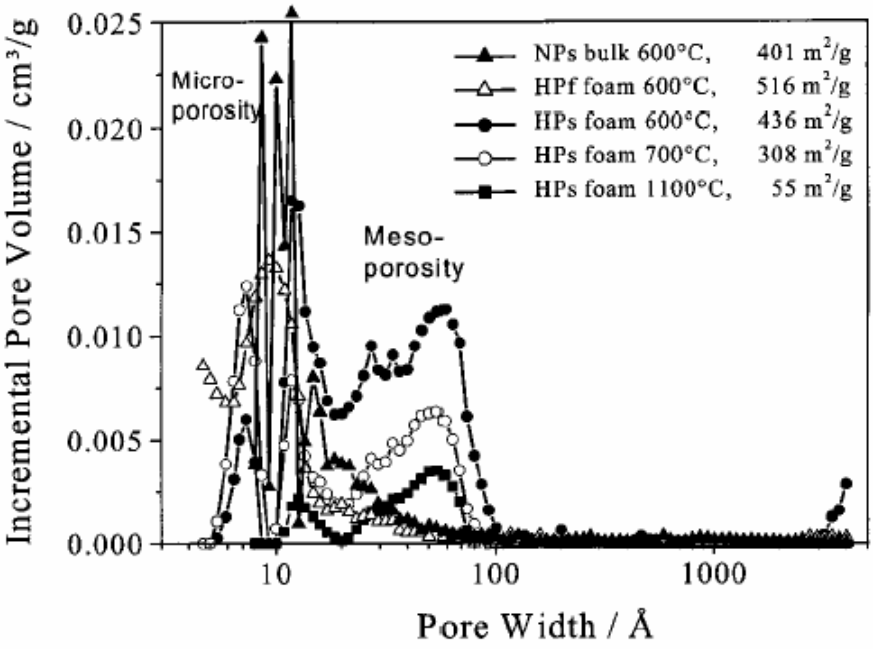

Figure 1.10- Pores size distribuition as function of pyrolysis temperature, heating rate and composition [95]; NPs: bulk samples; HP foam: silicon resin/PU, 1/1; HPf and s foam is referred to fast (2 K/min) and slow (0.1 K/min) haeting rate.

retention. The introduction of either inert or chemically active fillers can retain microporosity and thus also high SSA after pyrolysis at elevated temperatures (1200°C). In the effect of composition, heating rate, and pyrolysis temperature on the SSA of the ceramic material is reported (Figure 1.10).

Vollmer et al.[96] showed in their work how microporous amorphous silicon imidonitride (Si_2N_2NH) can be synthesyzed by ammonolysis of both co-oligomers of methylsilazane and dimethylsilazane and of block of copolymers of butadiene and methylsilazane.

Silicon imidonitride are interesting materials because they present both potential reactive base sites (SiNH) and a three dimensional network of structural units (SiN).

In the work presented by Vollmer the micropores volume was tailored as function of methil/silicon ratio and pyrolysis temperature. In the range pyrolysis temperature of 450-650°C, high SSA (350-425 m^2/g) imidonitride were prepared. The micropores formation was related to gases evolution (CH_4, NH_3) during pyrolysis.

Taking advantage of the intermediate state during pyrolysis when microporosity is formed by the evolution of volatile species, a recent paper published by Wilhelm et al.[97] defines a new class of materials called *Ceramer*.

The approach consists on the convertion of polymethyl- and poly (methylphenylsiloxanes) in a hybrid state by pyrolysis in nitrogen atmosphere.

Due to their high microporosity the ceramers are suited for applications like adsorption processes. Possible applications for these materials are then the areas of separation, gas storage, catalysis and removal of pollutants. One of the most important challanges posed by the increasingly stringent regulation of air pollution in many countries, is therefore, the search for efficient and economical control strategies for Volatile Organic Compounds (VOCs), e.g. hydrocarbns. At present, the applicable technology for VOC control is adsorption on activated carbon with subsequent recovery or incineration. Sorption behaviour of activated carbons is widely investigated and owing to their high SSA , high micropore volumes and rapid sorption capabilities, they offer an efficient technology. However it has been recognized that this technique is also subject to disadvantageous effects, such as fire risk, pore plug (due to polymerisation of some VOCs catalysed by some ashes present on activated carbon surfaces), hygroscopicity, and some problems associated with regeneration. Due to described diadvantages of activated carbons the development of alternative adsorbents is necessary and siloxane derived cearmers seem to be promising.

As reported in [97], Wilhelm et al. studied the possibilities to tailor pores volume using dfferent precursors.

In the reported study, they used solid polymethylsiloxane PMS (MK, Wacker AG, Germany), liquid polymethylsiloxane precursor M120XB (GE Bayer Silicones, Germany), where the polymer was solved in Xylene, and a polymethylphenylsiloxane H44 (Wacker AG, Germany), which was used for the foamed ceramers. A detail description of the process can be found in [97]. In this context the we will give an overview.

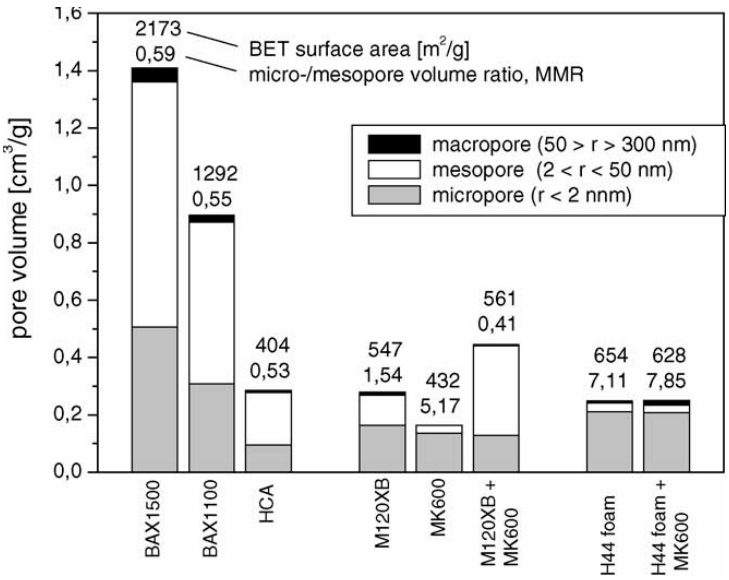

Figure 1.11- Pore Volume fraction, pores distribuition and Specific Surface Area (SSA) as function of the ceramic precursor, [97].

Five different samples were prepared MK600 (PMS, crosslinked in air at 200°C, grinded and sieved through mesh < 125 μm, uniaxially pressed and pyrolyzed under nitrogen flow at 600°C), H44 (crosslinked and foamed at 200°C in air and then pyrolyzed at 600°C), H44+MK600 (MK600 was added as filler before crosslinking), M120XB (same procedure as MK600), M120XB+MK600 (MK600 was added before crosslinking).

Specific surface areas and pores size distribuitions were then compared to commercially available wood-based activated carbons (BAX1500, BAX1100) and a monolhitic honeycomb (HCA).

In Figure 1.11 a results overview after nitrogen adsorption/desorption measurements and BET calculations is reported.

All ceramers produced by pyrolysis of M120XB and MK show almost identical micropore volume in the range of 0.12-0.16 cm^3/g. Distinctive differences were however manifested in their mesopores volumes. The addition of MK600 filler to the MK120XB increases the mespores volume considerably. The filler particles enhance the pore formation as shrinkage of the bulk is prevented during pyrolysis, and moreover, the decomposition of the material during thermal treatement leads to additional mesopores.

Comparing the sorption behavior of newly developed ceramers with the one of activeted carbons, the loading capacity of ceramers is comparable to that of activated carbons, possessing the same amount of pore volumes. Moreover, the very important advantage of the ceramers is the possibility to clean the adsorber totally from the adsorbed species whereas in case of activated carbon some vapours remains always trapped in the microstructure.

Williams et al.[98] studied the crosslinking effect of PCS on micropores retention after pyrolysis at 700°C. Both crosslinked and non-crosslinked PCS resulted in the development of microporous materials, the maximum apparent surface density and pore volumes for both materials being similar. However, differences occured, with the non-crosslinked material having a plateau region of highest surface areas between 400 and 600 °C, while that of the crosslinked material rose to a maximum at around 600 °C. A further difference in the two materials is that at 700°C, the microporosity was lost in the non crosslinked material, but was still apparent in the crosslinked material. The loss of microporosity at 700°C for the non crosslinked sample arose from the conversion from a polymer to an amorphous inorganic material and occured at a lower temperature than in the crosslinked sample, the maximum microporosity occuring at the point where this transition began.

Since pores formation during pyrolysis is accomodated by viscous flow, it is a temperature dependent process. Ageing effects in inert atmospheres at temperatures lower or equal to those of pyrolysis showed very low (< 10wt.%) weight loss[95,98].

However this limits the high temperature application of these materials to inert and reducing atmospheres only, as it was shown that heat treatemnt in air results in lost of SSA.

Other techniques are available in order to increase the PDCs surface densities, such as HF etching for oxide containing ceramics[22], deposition of a mesoporous coating or zeolites[99]. This techniques will be dscussed in more detail in Chapter 4.

In Table 1.5 a literature overview of High SSA ceramics from the pyrolysis of preceramic polymers is reported.

Table 1.5- Literature overview of high SSA ceramics, derived from pyrolysis of preceramic polymers.

PP	T_{curing}	T_{pyr}	SSA	Ref.
PCS	200	600	473	[98]
PCS	200	700	338	[98]
PCS	-	600	454	[98]
PS	-	600	450	[93]
PS+MTMSorPTMS	-	>1000	163	[94]
SR/PU	-	600	500	[95]
SR/PU+activated carbon or β-SIC	-	1200	130	[95]
SiliconImidonitride	-	650	425	[96]
PMS	200	600	547	[97]
PMPS	200	600	654	[97]
PMS+PMPS	200	600	628	[97]
PMS solid	200	600	432	[97]

1.4 Membranes

Ceramic membranes have attracted considerable attention because of their potential applications in harsh enviroments , since they possess excellent thermal and chemical stability (0<pH<14) and are usable under critical conditions where polymeric membranes are unstable[100]. Moreover, they offer the possibility of easy regeneration.

The applications ranges from food and biotechnology to waste water treatment and gas separation techniques and open a wide variety of innovative developments[101].

Ceramic membranes normally have an asymmetrical structure composed of at least two, mostly three, different porosity levels. Indeed, before applying the active, microporous top layer, a mesoporous intermediate layer is often applied in order to reduce the surface roughness. The macroporous support ensures the mechanical resistance of the nanofilter.

The ceramic membranes are often formed into an asymmetric, multi-channel element. These elements are grouped together in housings, and these membrane modules can withstand high temperatures extreme acidity or alkalinity and high operating pressures, making them suitable for many applications where polymeric and other inorganic membranes cannot be used (Figure 1.12).

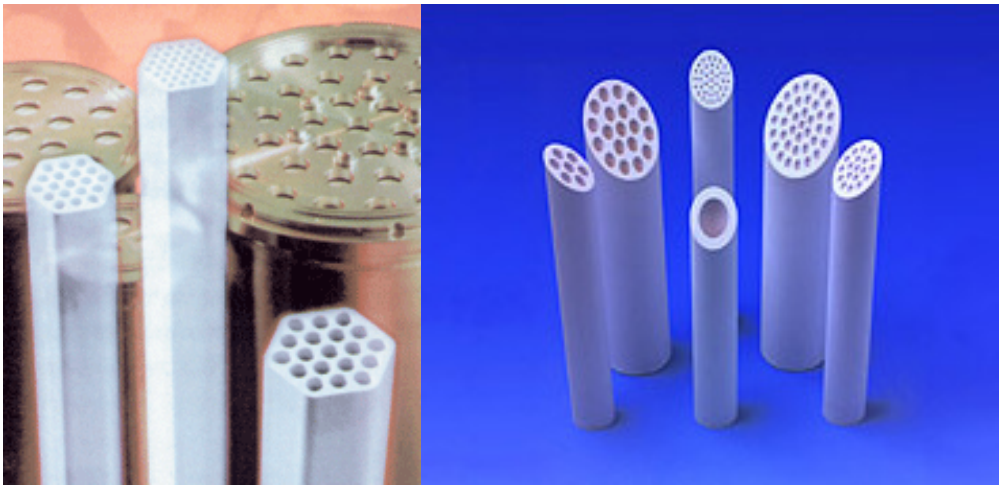

Figure 1.12- Some exemples of commercially available ceramic membranes

Commercially available ceramic membranes cover compositions from A to Z in terms of materials (from α– Al_2O_3 to ZrO_2). Commercial applications of alumina (α–Al_2O_3) membranes have been found in the brewing (wine and beer clarification) and the pharmaceutivcal industries.

Microporous ceramic membranes can be expected to use in membranes reactors for conversion enhancement in dehydrogenation[102] and methane reforming reactions for hydrogen production. Hydrogen-permselective amorphous silica-based membranes have been synthesized using chemical vapour deposition[103] (CVD) and sol-gel technique[104].

Unfortunately , these highly permeable layers often have poor thermochemical stability, for example prolonged use or certain impurities can trigger phase transformations, which degrade the membrane selectivity[105,106].

More recently ceramic membranes have been produced by the polymer pyrolysis route, by stopping pyrolysis at appropriate temperatures in order to allow micro- and meso-pores formation. In Tab.5 a literature overview of PDCs membranes is reported.

Generally, a microporous ceramic membrane can be fabricated on a porous support (α- Al_2O_3), and an important structural feature is a mesoporous intermediate layer, i.e. γ- Al_2O_3, which is placed in between the layer of a hydrogen permselective microporous thin layer. To develop high-performance hydrogen separation membranes, it is important to develop technologies for fabricating a fine mesoporous

intermediate layer as well as fabricating a molecular-sieve microporous membrane. The polymer pyrolysis route offers both possibilities since the gas evolution during the polymer to ceramic conversion is responsable for pores formation. Pores size, as previously reported, can be designed as function of the ceramic precursor (polymer architecture), crosslinking and pyrolysis temperature, and possibly by adding sacrificial templates of appropriate size.

In the work of Iwamoto et al.[107] a microporous amorphous silica membrane has been synthesized by thermal conversion in air of polysilazane on a silicon nitride (Si_3N_4) porous substrate.

The Si_3N_4 porous substrates were prepared by mixing commercially available α- Si_3N_4 with 5 wt.% α- Al_2O_3 and 5 wt.% Y_2O_3. Turbostratic graphite was used as sacrificial filler to create porosity.

After ball-milling, powders were sieved and then uniaxially pressed at 5 Mpa. The green compact was then Hot Isostatically Pressed at 40 MPa up to 1550°C under N_2. The residual carbon in the speciemen was burned-out by heat treatement at 600°C in air.

By this route substartes with a mean pore size of 80 nm and 28% porosity were prepared.

The SiO_2/Si_3N_4 intermediate composite layer was prepared by spin-coating a Polysilazane (PSZ) solution in Xylene. The PSZ was crosslinked in nitrogen at 270°C and then heat treated in air up to 600°C. During the heat tretement in air, the nitrogen and hydrogen in the PSZ could be fully substituted by oxygen.

Microporous SiO_2 membrane was prepared by spin-coating the PSZ solution, that was cured in air at 270°C. The air-curing allowed the formation of Si-O-Si bonds at relativly lower temperatures. The complete conversion of PSZ into SiO_2 , was then realized by heat treatement in air at 600°C. A very thin (< 150 nm) and defect-free layer was prepared. The crosslinking in nitrogen was effective for the mesoporous structure developement of the PSZ-derived silica within the porous substrate, and the continuous volatilization of the light weight molecules in the PSZ is considered to act an important role for the formation of the mesopores. The H_2 permselectivity was found to be competitive with previous results reported in literature (H_2/N_2= 141).

Li et al.[108] prepared an amorphous Si-O-C membrane on the outer surface of an $\tilde{\alpha}$–Al_2O_3 support. The intermediate layer was formed by dip-coating the substrate with p-xylene solutions of polycarbosilane (PCS). It was dried, cured in air at 200°C and pyrolyzed under nitrogen flow at different temperatures (T_{min}= 350°C, T_{max}= 950°C). The SiOC membranes were prepared by addition of Polystirene (PS) in the starting solution, in order to increase the pores percentage and consequently permeation properties. The pyrolysis temperature was increased up to 950°C because gases, especially hydrogen, require to be separated at temperatures higher than 500°C.

However what was observed from adsorption-desorption measurements was that pyrolysis between 450-650°C increased the volume of mesopores. This was mainly caused by volatilization of small molecules. After pyrolysis at 750°C and 950°C, most mesopores vanished. The surface area was increased by devolatilization of PS prior to decomposition of PCS, and it reached a maximum at 550°C. When the pyrolysis temperature was increased further, PCS was conveted to an inorganic structure with three-dimensional crosslinkings. The surface area was then decreased by more than one order of magnitude. Permeation measurements revealed a great improvement by addition of PS up to 10^{-7} mol/m*s*Pa after pyrolysis at 950°C and H_2/N_2 selectivity of 11.5 at the same pyrolysis temperature. For the prospect utilization of the membrane the satisfactory permeance should be in the order of 10^{-8} mol/m*s*Pa for hydrogen and the selectivity of hydrogen with respect to nitrogen over 100.

Suda et al.[109] studied the crosslinking effect on micropores formation on SiC-based membranes deriving from the pyrolysis of a commercially available PCS. In this study Polystirene (PS) was added as thermal-liable polymer.

They observed three main phenomenons:

- the existance of radical reactions between evolved gases from PS and functional groups of the pore wall in the samples like non-crosslinked PCS+PS may contribute to change micropores structure.
- The network formation in the precursor matrix was suggested to serve to prevent aggregation of gases evolved during pyrolysis. Crosslinked PCS start to form 3D network in the precursor matrix at lower pyrolysis temperature, resulting in the relativly smaller pore size compared with non-crosslinked samples.
- The kinetic gas diameter of the gases evolved during pyrolysis also contributes to determine the size of micropores.

Nagano et al.[110] reprt on gas permetion properties of SiC membranes from PCS without oxygen-curing process (Table 1.6). In the reported study the capillary force effect during the porous support dip-coating in a PCS- Xylene solution are also investigated. The use of capillary force during initial dip-coating of PCS was effective to suppress defect in SiC film.

Wach et al.[111] used a PCS/PVS blend in order to improve the film properties (defect free) on a porous Al_2O_3 support. The plasticizing effect of PVS allows for the development of asmoother coating on the substrate during solvent evaporation, and reducing formation of cracks and pinholes during pyrolysis. Moreover they used ion irradiation technique instead of the usual thermal treatement (Table 1.6).

Table 1.6- Literature overview properties of PDCs membranes. T_{cur} is the curing temperature in air if not specified otherwise, T_{pyr} is the pyrolysis temperature in inert atmosphere if not specified otherwise, PH_2 is the permeance to Hydrogen measured at T_m, H_2/N_2 is the ceramic membrane permselectivity measured at T_m (measurement temperature).

Ceramic Precursor	T_{Cur} (°C)	T_{Pyr} (°C)	Composition	PH_2 (mol/m^{2}s Pa)	H_2/N_2 Permselectivity	T_m (°C)	Ref.
PCS+PS	200	550	SiOC	10^{-7}	11.5		[108]
PCS/PVS blend	Ion Irr.	850	SiC	10^{-8}	149	200	[111]
PSZ	270 N_2	600 Air	SiO_2	$1.3*10^{-8}$	141	300	[107]
PCS	80	400-800	SiC	10^{-7}-10^{-8}	>100	700	[109]
PCS	300 Ar	800	SiC	$1.3\text{-}8.1*10^{-7}$	-	600	[110]
PCS	200	950	SiOC	$1*10^{-8}$	18-63	500	[108]
PCS		470	SiC	-	14.3		[112]
PCS	200	500	SiC	$5.5*10^{-7}$	6.7	400	[113]
PDMS	200	300	SiOC	$8.9*10^{-8}$	<100		[114]

Figure 1.13 reports some examples of PDC membranes.

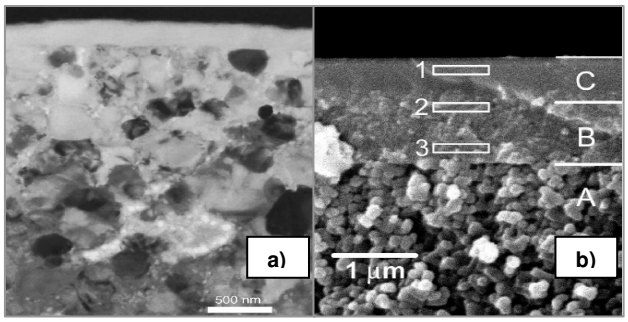

Figure 1.13- PDCs membranes: (a) Cross-sectional TEM image of PSZ-derived amorphous silica membrane fabricated on a Si_3N_4 porous substrate [107]. (b) SEM picture of a cross-section of the coated plate. The cross-section components are denoted as: A – γ-alumina, 100 nm grade; B –α-alumina, 10 nm grade; C – SiC coating [111].

References

[1] Bernardo E., Colombo P., Cellular structures, in "Ceramic Science and Technology", Volume 1, R. Riedel, I.-W. Chen eds, WILEY-VCH Verlag GmbH, Weinheim, Germany, in press (ISBN 3-527-31149-1)

[2] a) Haber, J. *Pure & Appl. Chem. 63*, 1227-1246 (1991); b) Rouquerol, J., Avnir, D., Fairbridge, C.W., Everett, D. H., Haynes, J.M., Pernicone N., Ramsay, J.D.F., Sing, K.S.W., Unger, K.K. *Pure & Appl. Chem.*, *66*, 1739-1758 (1994).

[3] Ashby, M. F., *Cellular Solids Scaling of Properties*, in *Cellular Ceramics*, Sheaffler, M. and Colombo, P. Ed. 3, Wiley- VCH Verlag Gmbh, (2005).

[4] Riedel, R., *Advanced Ceramics from inorganic polymers*. In: Brook RJ editor. Materials science and technology, a comprehensive treatment, vol. 17B. Processing of Ceramics. Part II. Weinheim: Wiley-VCH; 1-50 (1995).

[5] Richter, R., Roewer, G., Bohme, U., Busch, K. et al., *Applied Organometallic Chemistry*, 11, 71 (1997)

[6] Lange, F. F., *Science,* 273 (1996) 903

[7] Harshe, R., Balan, C., Riedel, R., *J. Eur. Ceram. Soc.* 24, 3471 (2004).

[8] Colombo, P. and Hellmann, J. R., *Mat. Res. Innovat*. 6, 260 (2002).

[9] Colombo, P., Bernardo, E. and Biasetto, L., *J. Am. Ceram. Soc.* 87-1, 152 (2004)

[10] Greil, P., *Adv. Eng. Mat.* 2-6 (2000) 339

[11] Bernard, S., Weinmann, M., Cornu, D., Miele, P. and Aldinger, F., *J. Eur. Ceram. Soc.,* 25 (2-3), p 251 (2003)

[12] Yajima S., Hasegawa Y., Okamura K, and Matsusawa T., *Nature*, 273, 525-7 (1978)

[13] R. Riedel and W. Dressler, *Ceramics International,* 22 (1996) 233-239

[14] Yajima, S.., Hayashi, J., Omori, M. and Okamura, K., *Nature (London)*, 261, 683 (1976)

[15] Seyferth, D., Wiseman, G. H. and Prud' Homme, C., *J. Am. Ceram. Soc.,* 66, C-13 (1983)

[16] Peuckert, M., Vaahs, t. and Bruck, M., *Adv. Mater.*, 2, 398 (1990)

[17] Monthioux M, Delverdier O *J Europ Ceram Soc* 16: 721 (1996).

[18] Danko GA, Silberglitt R, Colombo P, Pippel E, Woltersdorf J.., *J Amer Ceram Soc,* 83, 1617 (2000)

[19] Jacubenas K, Marcus HL *J Am Ceram Soc* 78, 2263 (1995)

[20] Pivin, J. C. and Colombo, P., *J. Mater. Sci.* 32, 6163-6173 (1997)

[21] Kleebe H.-J., Braue, W., Schmidt h, Pezzotti G., Ziegler G., *J. Europ. Ceram. Soc.* 16, 339-51 (1996)

[22] R. Peña-Alonso, G.D. Sorarù, R. Raj, *J. Am. Ceram. Soc.*, 89, 2473-2480 (2006).

[23] Gregori, G., Kleebe, H.-J., Brequel, H., Enzo, S., Ziegler, G., *J. Non- Crystalline Solids*, 351, 1393-1402, (2005)

[24] Lynch C. T., *Practical Handbook of Materilas Science*, CRC Press Inc. Boca Raton, Florida US, (1989)

[25] Wu S., Cheng L., Zhang Q., Zhang L., Xu Y., *Applied Cermic Tech*., 3, 75-79 (2006)

[26] Le Coustumer P., Monthioux M., Oberlin A., J. Eur. Ceram. Soc., 11, 95-103 (1993)

[27] Renlund GM, Prochazka S, Doremus RH. J. Mater. Res., 6, 2723-34 (1991)

[28] Riedel, R., Mera, C., Hauser, R., *J. Ceram. Soc. of Japan,* 114, 425-444 (2006)

[29] Saha A., Raj R. and Williamson D. L., *J. Am. Ceram. Soc*., 89, 2188-95 (2006)

[30] Saha A., Raj R., Williamson D. L. and Kleebe H-J, *J. Am. Ceram. Soc.,* 88, 232-34 (2005)

[31] Gibson, LJ, Ashby MF, *Cellular Solids, structure and properties*, 2nd edn. Cambridge University Press, UK (1999)

[32] Gaukler L, Waeber MM, Conti C, Jacob-Duliere M, Light Metals 1985, in: Proc. Of the technical sessions at the 114th annual meeting of the metallurgical society of AIME. New York, 1261-1283 (1985)

[33] Saracco G, Russo N, Ambrogio M, Badini C, Specchia V, *Cat Today*, 60, 33 (2000)

[34] Studart A. R.,Gonzenbach U. T. ,Tervoort E. and Gauckler L., J, Am. Ceram. Soc. 89,1771-89 (2006)

[35] Schwartzwalder K.and Somers A. V., *Method of Making Porous Ceramic Articles,* US Pat. No. 3090094, May 21(1963).

[36] Bao X., Nangrejo MR, Edirisinghe MJ, *J. Mater. Sci.* 35, 4365 (2000)
[37] Nangrejo MR, Bao X, Edirsinghe J, *J. Mater. Sci. Letters,* 19, 787 (2000)
[38] Wood L. L., Messina P., and Frisch K. ''Method of Preparing Porous Ceramic Structures by Firing a Polyurethane Foam that is Impregnated with Organic Materia.'' U.S. Patent, 1974.
[39] Wu M. X .and Messing L. G., *J. Am. Ceram. Soc.*, 73, 3497–9 (1990).
[40] Binner, J., *Cellular Ceramics,* edited by Scheaffler , M.& Colombo, P., 33 (2005) Wiley-Vch, Germany.
[41] Gregorova E., Pabst W., Bohacenko I., *J. Europ. Ceram. Soc.,* 26, 1301-09 (2006)
[42] Imhof A. and Pine D. J., *Nature*, 389, 948–51 (1997).
[43] Imhof A. and Pine D. J., *Adv.Mater.*, 11, 311–4 (1999).
[44] Akartuna I., Studart A. R., Gonzenbach U. T., Tervoort E., and Gauckler L. J., ''Porous Ceramics from Particle-Stabilized Emulsions,'' Adv. Mater., (2006), submitted.
[45] Sepulveda, P., *Am. Ceram. Bull.*, 76, 1997
[46] Sherman AJ, Tuffias RH, Kaplan RB, *Bull. Am. Ceram. Soc*. 70, 1025, (1991)
[47] Green DJ, *J. Am. Ceram. Soc*. 73, 85 (1985)
[48] Aoki Y, McEnaney B, *Brit. Ceram. Transactions* 94, 133 (1995)
[49] Kehr, C. I., US Patent 3,660,217, 1972.
[50] Frost, R. L., McBrayer, R.D. and Prujari , V. K., US Patent 4,381,815 (1983).
[51] Nangrejo M.R. et al., *J. Europ. Ceram. Soc*. 20, 1777-85 (2000)
[52] Nangrejo M.R. et al., *Int. J. Inorg. Mat.*, 3, 37-45 (2001)
[53] Renlund GM, Minnear WP, Bracco AA (1991) US Patent # 4,981,820, January 1
[54] Renlund GM, Lewis LN, Stein J, Bracco AA (1993) US Patent # 5,180,694, January 19
[55] Daws DE, Castellucci NT, Carpenter HW, Colby MW (1997) US Patent # 5,643,512, July 1
[56] Colombo, P., Hellmann, JR, *Mat. Res. Inn.*, 6, 260-72 (2002)
[57] Takahashi, T., Munstedt, H., Colombo, P. and Modesti, M., *J. Mat Sci.*, 36, 1627-39 (2001)
[58] Gibson, L.J. and Ashby, M. F., *Cellular solids, structure and properties*, 2nd ed. Cambridge University Press (1999)
[59] Colombo, P. and Bernardo, E., *Comp. Sci. and Tech.*, 62, 2353-59 (2003)
[60] Gambaryan-Roisman, T., Scheffler, M., Buhler, P. and Greil, P., *Ceram. Trans.*, 108, pp. 121-30 (2000)
[61] Gambaryan-Roisman, T., Scheffler,M., Takahashi, T., Buhler, P. and Greil, P., in Muller, G.editor, *Euromat 99*, 12 (Ceramics Processing, Reliability, Tribology and wear), 247-51 (2000)
[62] Greil P., *J. Amer. Ceram. Soc.*, 78, 835 (1995)
[63] Zeschky, J, Goetz-Neunhoeffer, F., Neubauer, J., Jason Lo, S. H., Kummer, B., Scheaffler, M. and Greil, P., *Comp. Sci. and Tech.*, 63, 2361-70 (2003)
[64] Gambaryan-Roisman, T., Scheffler T., Buhler, P. Greil, P., Colombo P., *J. Am. Ceram. Soc.*, 84, 2265-68 (2001)
[65] Peng, H.X., Fan, Z. and Evans, J.R.G., Mat. Sci. and Tech., 16, 903-7 (2000)
[66] Zeschky, J., Hofner, T., Arnold, C., Weiβmann, R., Bahloul, D., Scheaffler, M. and Greil, P., *Acta Mater*., 53, 927-37 (2005).
[67] Shibuya A., Takahashi T., Koyama K, *Comp. Sci. and Tech.*, 67, 119-24 (2007)
[68] Martini-Vedensky, J.E., Suh, N.P. and Waldman F.A.., US Patent no. 4,473,665, Sep 25 (1984)
[69] LeMay, J.D., Hopper, R.W., Hrubesh, L.W., Pekala and R.W., *MRS Bull* 15, 19-45 (1990)
[70] Fitzgerald T. J., Michaud V. J., Mortensen A., *J. Mater. Sci.*, 30, 1037-45 (1995)
[71] Colombo, P., Bernardo E.
[72] Kim Y-W, Kim S-H, Kim H-D, Park C B, *J. Mater. Sci*. ,39, 5647-52 (2004)
[73] Kim Y-W, Jin Y-J, Chun Y-S, Song I-H, Kim H-D, *Scripta Materialia*, 53, 921-25 (2005)
[74] Kim Y-W, Kim S-H, Song I-H, Kim H-D, Park C B., *J. Am. Ceram. Soc.*, 88, 2949-51 (2005)
[75] Jang D-H, Kim Y-W, Song I-H, Kim H-D, Park C B, *J. Ceram. Soc. of Japan*, 114, 549-53 (2006)
[76] Song I-H, Kim M-J, Kim h-D, Kim Y-W, *Scripta Materialia*, submitted (2006)
[77] Kim Y-W, Kim H-D, Park C B, J. Am. Ceram. Soc., 88, 3311-3315 (2005)

[78] Kim Y-W, Kim S-H, Xu X, Choi C- H, Park C-B, *J. Mater. Sci. Letters*, 21, 1667-69 (2002)
[79] Kim Y-W, Kim S-H, Wang C, Park C B, J. Am. Ceram. Soc., 86, 2231-33 (2003)
[80] Kim Y-W, Park C-B, *Composites Science and Technology,* 63, 2371-77 (2003)
[81] Wang C, Wang J, Park C B, Kim Y-W, *J. Mater. Sci.*, submitted (2006)
[82] Sung I-K, Yoon S-B, Yu J-S, Kim D-P, *Chem. Commun.*, 1480-81 (2002)
[83] Soled S., Mc Vicker g. B., *Catal. Today*, 14, 189-94 (1992)
[84] Kokubu T., Yamane M., *J. Mater. Sci*., 22, 2583-88 (1987)
[85] Tan Y., dou L., Lu D., Wu D., *J. Catal*., 129, 447-56 (1991)
[86] Leboda R., *Mater. Chem. Phys*., 31, 243-55 (1992)
[87] Singh A. K. and Pantano C., *J. Am. Ceram. Soc.,* 79, 2696-704 (1996)
[88] Liu C., Chen H. Z., Komarneni S., Pantano C. G., *J. of Porous Materials,* 2, 245-52 (1996)
[89] Yao H., Kovenklioglu S., Kalyon D. M., *Chem. Eng. Commun*., 86, 155-75, (1990)
[90] Wan, J., Gasch, M. J. and Mukherjee, A. K., *J. Am. Ceram. Soc.*, 84, 2165-69 (2001)
[91] Konetschny C, Galusck D., Reschke S., Fasel C. and Riedel R., *J. Eur. Ceram. Soc.*, 19, 2789-96 (1999)
[92] Seitz J. and Bill J., *J. Mater. Sci. Lett.*, 15, 391-93 (1996)
[93] Schmidt H., Koch D., Gratwohl G., *Ceramic Transactions*, 101, Am. Ceram. Soc., Westerville, pp. 275-84 (2000)
[94] Schmidt H., Koch D. and Grathwohl G., Chem. Eng. Technol., 23, 959-64 (2000)
[95] Scmidth H., Koch D., Grathwohl G. and Colombo P., *J. Am. Ceram. Soc.*, 84, 2252-55 (2001)
[96] Vollmer O., Lefebvre F. and Bradley J., *J. Mol. Cat. A: Chem.*,146, 87-96 (1999)
[97] Wilhelm, M., Soltmann, C., koch, D.and Grthwohl, G., *J. Eur. Ceram. Soc.*, 25, 271-276, (2005).
[98] Williams H. M., Dawson E. A., Barnes P.A., Rand B., brydson R. M. D., Brough a. R., *J. Mater. Chem.*,12, 3754-60 (2002)
[99] Zampieri A., Colombo P., Mabande GPT, Selvam T, Shwieger W, Scheffler F, *Adv. Mater*., 16, 819-23 (2004)
[100] Bhave, R.R., *Inorganic Membranes: Synthesys and Applications*, Van Nostrand Reinhold, New York (1991).
[101] Bhave R.R., (Ed), Synthesis of Inorganic Membranes, in *Inorganic Membranes- Synthesis, Characteristics and Applications*, van nostrand-Reinfold, New York (1991)
[102] Van Veen, H. M., Bracht, M., Hamoen, E. and Alderliesten, P. T., *Inorganic Membrane Science and Technology, Membrane Science and Technology Series,* 4, 641-676, ed. A. J. Burgraaf and L. Cot. Elsevier, Amsterdam, (1996)
[103] Prabhu, A. K. and Oyama, S. T., *J. Membr. Sci.*, 176, 233-248 (2000).
[104] Kurungot, S., Yamaguchi, T. and Nakao, S., *Catal. Lett.*, 86, 273-278 (2003)
[105] Tsai D.and Hsieh C.C., *J. Am. Ceram. Soc*., 74, 830-36 (1991)
[106] Saracco G., Versteeg G. F. and Sawaaji W. P. M., *J. Membr. Sci.*, 95, 105-23 (1994)
[107] Iwamoto, Y., Sato, K., Kato, T., Inada, T. and Kubo, Y., *J. Eur. Ceram. Soc.*, 25, 257-264 (2005)
[108] Li Z., Kusakabe, K. and Morooka, S., *J. Memb. Sci.*,118, 159-168 (1996)
[109] Suda H., Yamauchi H., Uchimaru Y., Fujiwara i., Haraya K., *J. Cer. Soc. of Japan*,114, 539-44 (2006)
[110] Nagano T., Sato k., Saitoh T., Iwamoto Y., *J. Cer. Soc. of Japan*,114, 533-38 (2006)
[111] Wach R. A., Sugimoto M., Yoshikawa M., submitted to *J. Am.Ceram. Soc*. (2006)
[112] Shelekhin A. B., Grosgogeat E. J., Hwang S. T., *J. Membr. Sci*., 66, 129-41 (1991)
[113] Kusakabe K., Li Z.Y., Maeda H., Morooka S., j. Membr. Sci.,103, 175-80 (1995)
[114] Lee L.-L., Tsai D.-H., *J. Am. Ceram. Soc.*, 82, 2796-800 (1999)

Chapter 2

Fabrication of Microcellular Ceramic Foams and their Characterization

2.1 Introduction

As reported in §1.3.3 microcellular ceramics deriving from preceramic-polymers, are mainly produced by the sacrificial template method. Moreover, new techniques have been developed, such as inducing a thermodynamical instability. This novel approach is currently under investigation since a better control on the process parameters (crosslinking time and temperature, temperature and pressure effect of CO_2 on pores formation) is necessary in order to extend this process to an industrial scale.

This research group has recently reported the use of preceramic polymers and sacrificial microbeads to produce microcellular foams[1]. This process allows for a very good control on cell and cell-window size distribuition, degree of interconnecitvity, porosity percentage and consequently properties of the porous ceramic component.

The interest in the development of microcellular structures rises from the improved properties compared to the ones of macrocellular foams[1].

Their increased cell-densitiy and smaller cell size compared to macrocellular foams opens wide range of new applications. In Tab.2.1 an overview of the applications, involving micro and macrocellular ceramic foams is reported.

Table2.1-Typical applications for macro and microcellular ceramic foams

Applications	
Macrocellular	**Microcellular**
Melt metal Filters	Hypervelocity Impact Shields
Heating Elements	Microreactors
Porous Burners	Thermal Protection Systems
Aereation of Liquids	Electromagnetic filters
Bone Replacement	Radar Active Materials
Host for Interpenetrating Composites	Solid-fluid Separation Processes

Since the main goal of this research was to functionalize microcellular SiOC foams for specific applications, a complete characterization was needed. The properties here analyzed are mainly related to morphology. As reported in Appendix 1, beside composition, morphology is for cellular structures, the main responsable of the final material properties (mechanical, thermal, acoustic and permeability).

The high geometric surface available makes them a very promising host for the deposition of functionalized coatings. Moreover, the use of microcellular ceramic foams seems to be particularly promising in solid-fluid separation processes, in which the filtering layer must present low pressure drop and high particle collection efficiency. The high porosity level provides a large volume of flow paths and therefore a suitable permeability level for an economic large-scale operation. On the other hand, the micro-sized pores ensure an efficient barrier for superficial collection of particles, avoiding depth filtration and subsequent permanent clogging of filter.

In order to be effectively employed in fluid flow applications, microcellular ceramic foams must have their permeability analyzed, and preferably related to other structural properties, such as porosity and average pore size[2].

In this chapter, the permeability to gas flow of microcellular ceramic foams, prepared using a polysiloxane as SiOC precursor and poly-methylmetacrylate (PMMA) microbeads as sacrificial fillers, is reported. Forchheimer's equation for flow of compressible fluids was applied to fit permeability constants. A model available in the literature for predicting permeability from structural parameters was tested and compared to experimental data. Preliminary investigation on the feasibility of prepared samples for aerosol filtration applications was also conducted.

2.2 Experimental

2.2.1 *Materials and Production Process*

The polymer used for this research is a product from Wacker Chemie GmbH, Burghausen, with the trade name Wacker-Bensil PMS MK (MK polymer). The MK polymer is a solid solvent free poly(methylsilsesquioxane) polymer with [CH3SiO1.5]*n* basic structure and falls under the silicone resin group. The odorless, colorless flakes of MK-polymer have a softening range between 45 and 60 °C and a good solubility in organic solvents, namely, aromatic solvents and ketones. The polymer possesses approximately 2 mol.% hydroxy and ethoxy groups, as functional units. Accordingly, the possible structure of the used resin along with its functional groups is illustrated in Fig. 2.1.

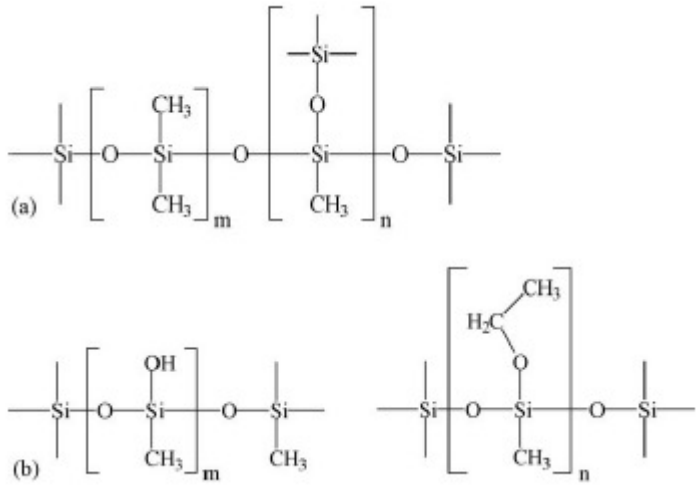

Figure2.1- Section of the molecular structure of the commercial poly(methylsilsesquioxane) Wacker-Bensil PMS MK: (a) linear and crosslinked polymer network units; (b) structural units containing OH- and OEt-functional groups which are used for cross-linking.

With evolution of water and ethanol by polycondensation reaction, the formation of a three dimensional network with Si–O–Si alternating units as the backbone takes place. In order to achieve an acceptable process regime, the addition of a suitable crosslinking agent in sufficient amount and a specific thermal treatment[3] are necessary mainly for the production of fully bulk components. As concern foam production process, crosslinking can proceed in air at T < 200 °C, without any catalyst addition.

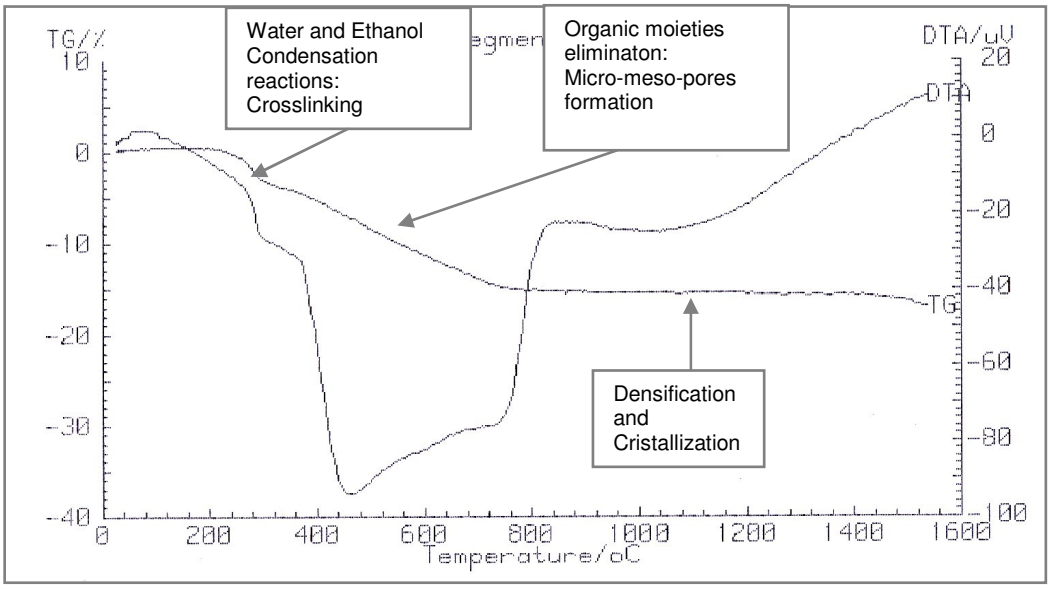

Figure 2.3- TGA-DTA measurements on a.r. MK

In Fig.2.3 TGA-DTA measurements on a.r. MK is reported (heating rate 10°C/min under nitrogen flow, using a METZSCH STA 409)

As can be observed in Fig.2.3 there is a first consistent weight loss in the range 200-300°C corresponding to crosslinking reactions of the polymer (water and ethanol condensation) and a second consistent weight loss in the temperature range 300-700°C. This weight loss can be attribuited to $-CH_3$ elimination, that is the true polymer pyrolysis. During this step mainly mesopores are formed (see §1.4.1) and further heating causes pore collapse and densification.

In Tab.2.2 a comparison of some of the processing parameters between SiOC bulk and foamed is reported.The bulk SiOC was crosslinked by Zr-catalyst and warm-pressed[3] while the SiOC foam was crosslinked during warm pressing and further annealing at 300°C in air (conducted in order to eliminate the PMMA microbeads).

Table 2.2-Comparison of some processing parameters of SiOC both bulk and foam

	T Pyrolysis °C	Cross-linking	Mass loss wt.%	Axial Shrinkage[a] %	Radial Shrinkage[a] %	Green Density g/cc	Pyrolyzed[b] Density g/cc	Ref
SiOC bulk	1100	Zr-catalyst, Warm-pressing	11.48	16.75	19.45	1.26	2.16	[3]
SiOC foam	1200	Warm-pressing Annealing in air	86.3	15.56	21.93	1.01	0.29	[1]

a Average values of ten samples
b Pyrolysys temperature of 1100°C for SiOC bulk and 1200°C for SiOC foam

The higher mass loss of SiOC foam compared to SiOC bulk is of course due to the presence of 80 wt.% PMMA in the starting mixture.

In Tab.2.3 the final composition of SiOC bulk after pyrolysis at 1100°C is reported.

Table 2.3-SiOC composition after pyrolysis at 1100°C in inert atmosphere [3]

Material	Composition			Empirical Fomula
	Si	O	C	
SiOC	45.5	39.3	14.8	$Si_{1.00}O_{1.60}C_{0.80}$

In order to evaluate the effect of cell sizes on the gas permeability properties of microcellular ceramic foams, samples were prepared using poly-methylmetacrylate (PMMA) microbeads (Altuglas BS, Altuglas International, Arkema Group, Rho (MI), Italy) of different nominal sizes (10, 25, 50, 100, 185 μm, samples named S10, S25, S50, S100, S185, respectively) acting as sacrificial filler[1]. The powders were mixed at a constant weight ratio (20 wt% MK, 80 wt% PMMA) by ball milling for 1 hour and then

warm pressed (120°-180°C, 20 MPa). Warm pressing temperature was adjusted as function of PMMA microbeads size, in order to optimize the viscous flow of the molten polymer through the beads. In Fig.2.4, some SEM pictures showing the effect of warm-pressing temperature on the final cells shape for PMMA 25 µm is reported.

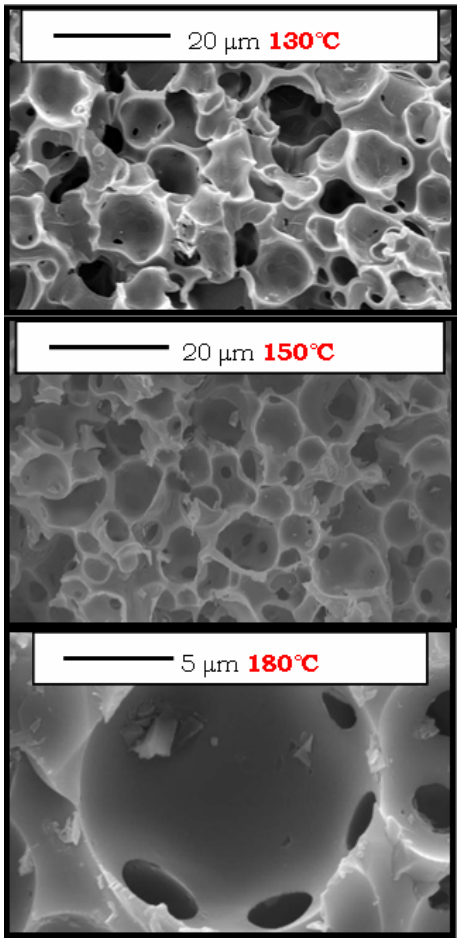

The green samples were then treated in air at 300°C for 2h (0.5°C/min) in order to burn out the PMMA microbeads and allow for the preceramic polymer crosslinking.

Details on the process production can be found in [1]. The silicone foams still in their polymeric stage were then pyrolyzed under nitrogen flow at 1200°C for 2 hours (heating rate = 2°C/min). During pyrolysis, the preceramic polymer samples were subjected to a large volume shrinkage (~50%; about 23% linear shrinkage) due to the polymer-to-ceramic transformation, occurring with the elimination of organic moieties and leading to the formation of an amorphous Si-O-C ceramic[12]. Cylindrical samples of 40 mm diameter and 5 mm thickness (before pyrolysis) were prepared.

Figure 2.4- The effect of warm-pressing temperature on cells shape, for PMMA 25 µm.

The effect of warm-pressing temperature and consequently degree of crosslinking of the MK polymer on the compression strength of the pyrolyzed foams has been investigated (Fig.2.6). The MK / PMMA ratio and the PMMA size were kept constant at 20/80 and 25 µm, respectively. These values were suggested by previous work reported in [1]. The crushing strength of the foams was measured at room temperature by compression testing, using UTM (Model 1121, Instron Danvers, MA) with a cross-head speed of 0.5 mm/min, on samples of nominal size of 10x5x3.5 mm. Each data point represents the average value of five individuals tests.

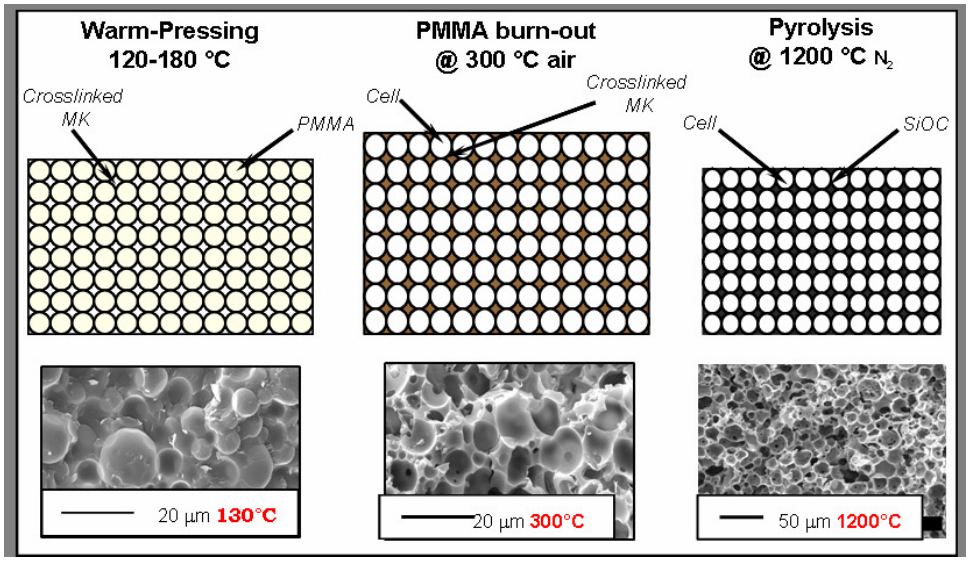

Figure 2.5- A schematic overview of the SiOC foams process production and correspondent SEM images. Linear dimensional changes in the scheme reflects linear shrinkage during the processing.

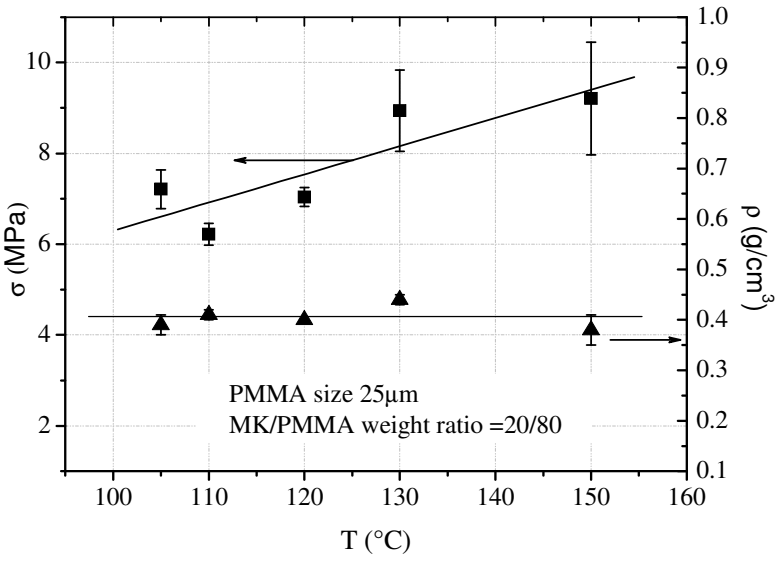

Figure 2.6- Compression strength (σ) and bulk density (ρ) as function of warm-pressing temperature.

As can be observed in Fig.2.6, increasing the warm-pressing temperature and consequently the degree of crosslinking of MK polymer, compression strength increases (from 6 up to 9.2 MPa) at constant bulk density. Warm-pressing temperature may be related to a double effect: since at the pressing temperatures the polymer melt, the pressure applied on the mixture allows for viscous flow of the MK through the beads, so granting an uniform coating on the beads.

Even though an excessive heating can be responsable of a uniform coating, it can also cause an excessive degree of crosslinking of the MK polymer, resulting in cracks formation during the PMMA burn-out. The most critical step in this process production is then related to warm-pressing temperature and microbeads burnt-out. A more detailed study of the warm-pressing temperature effects on polymer crosslinking would be then necessary in order to grant a faithful reproducibility of the process. The use of a dedicated instrument where temperature control is well defined has already been suggested.

In Fig.2.7 a comparison between microcellular and macrocellular SiOC foams compression strength as function of relative density is reported[4].

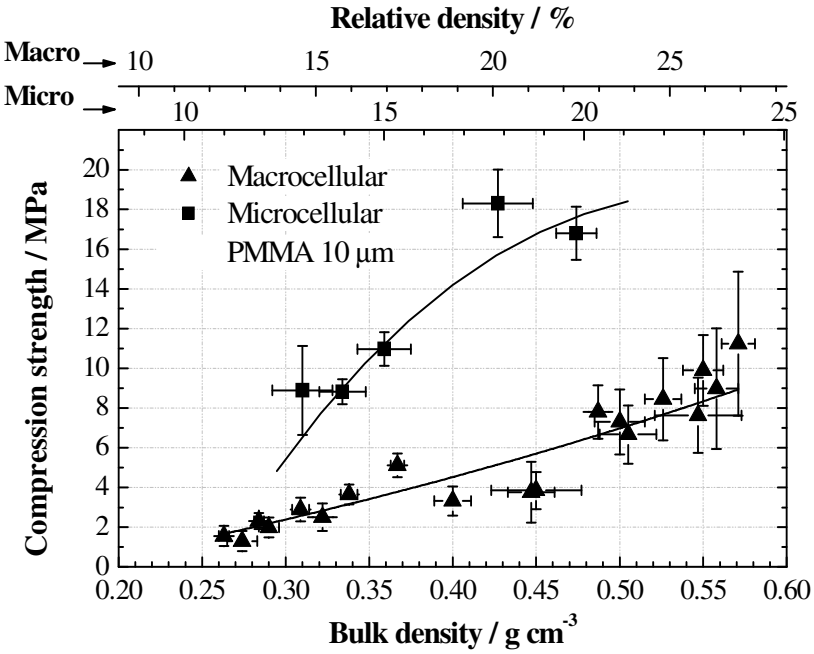

Figure 2.7- Macrocellular and microcellular SiOC foams compression strength as function of bulk density [4].

As expected, there is an increase of the compression strength with increasing relative density for both materials. Gibson and Ashby[56] proposed a correlation of the relative strength of foams with their relative density according to an exponential function. The value of the exponent is 1.5 for open cell foams, and ranges from 1 to 1.5 for closed cell foam, depending on the volume fraction of the solid contained in the cell edges.

The data collected for the microcellular foam samples are at the moment too few and dispersed to allow for a reliable estimate of the power exponent. What can be said with certainty is that the compression strength of microcellular foams is 2 to 5 times higher than that of macrocellular foams of similar density. One likely reason is that, in microcellular foams, the strut strength is higher because the strut surface area is much

smaller thus affecting the statistical distribution of flaws in the material(decreased probability of finding a flaw with critical dimension). In fact, the cell surface area is, for microcellular foams, 1-2 order of magnitude smaller than that of macrocellular foams, because of their smaller cell size. Another reason is that, with increasing relative density, it is the strut and the cell wall thickness that increase in microcellular foams,

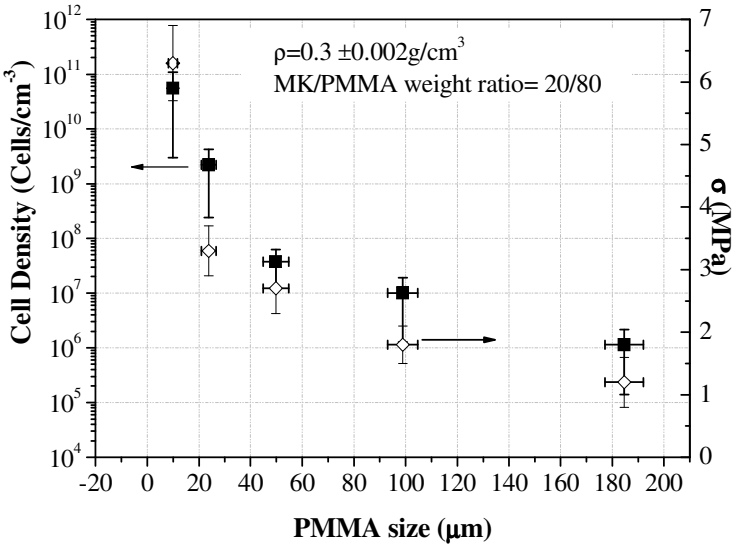

Figure 2.8- Compression strength and cell density as function of PMMA size.

In this work, the effect of PMMA size on cell density (number of cells per unit volume) and compression strength was studied (Figure 2.8). Cell density was calculated as reported in A.2.3 The crushing strength of the foams was measured as previously reported.

2.2.2 Methods

The size of the PMMA microbeads was measured by laser diffraction (Series 2600c droplet and particle sizer, Malvern Instruments Ltd., Worcestershire, United Kingdom). The cell window size (i.e. the size of the pore connecting adjacent cells) and total porosity of foams were measured by Mercury Porosimetry (Autoscan 33 Porosimeter, Quantachrome, Hook, United Kingdom) whereas the cell size was measured by Image Analysis (IA) (KS400, Carl Zeiss AG, Oberkochen, Germany) using a Field Emission Scanning Electron Microscope (FESEM: 6340F, Jeol, Tokyo, Japan). Micrographs were taken after impregnation of the porous ceramic samples with a polymeric resin in

order to obtain well-defined 2D images. Details on the Image Analysis process have been reported in A.2.2.

Gas permeability was measured under a nitrogen flow (CFP-1200-A PMI Capillary Flow Porometer, Porous Materials Inc., Ithaca, NY, USA). Permeability constants were fitted from Forchheimer's equation, expressed for flow of compressible fluids as[7,8]:

$$\frac{P_i^2 - P_o^2}{2 P_o L} = \frac{\mu}{k_1} v_s + \frac{\rho}{k_2} v_s^2 \qquad (1)$$

In which P_i and P_o are, respectively, the absolute gas pressures at the entrance and exit of the sample; v_s is the superficial fluid velocity, determined by $v_s = Q/A$, where Q is the volumetric flow rate and A is the exposed surface area of the porous medium perpendicular to flow direction; L is the sample's thickness (0.25 to 0.51 cm); μ is the gas viscosity (1.77×10^{-5} Pa*s) and ρ is the gas density (1.15 kg/m^3), evaluated for P_o=760 mmHg and T=24°C. The parameters k_1 and k_2 are usually known as Darcian and non-Darcian permeabilities, in reference to Darcy's law. They incorporate only the structural features of the porous medium and therefore are considered constant even if changing the fluid or the flow conditions. It is important to note that both parameters are dimensionally distinct: In SI units, k_1 is expressed in m^2, whereas k_2 is expressed in m.

The first term of Forchheimer's equation [$\mu v_s/k_1$] represents viscous energy losses and prevails at low fluid velocities, while the quadratic term [$\rho v_s^2/k_2$] represents the kinetic energy losses and is more significant at higher velocities. The relative contribution of each term on the total pressure drop also depends on the values of k_1 and k_2, which can change significantly according to processing conditions. Therefore, the knowledge of the predominant relationship (linear or quadratic) for the pressure drop curve is critical for designing the best driving equipment for fluid flow in a given application[2].

Permeability constants k_1 and k_2 were obtained in this work by fitting the experimental data of $[P_i^2-P_o^2]/2P_oL$ *versus* v_s in Equation (1), using the least-square method. At least 10 sets of P_i, P_o and v_s values were acquired in a stationary gas flow regime for each test. Details on permeability properties of cellular ceramics have been reported in Appendix1.

Before performing permeability measurements, the outer layer (a few hundred microns) was removed from the top and bottom surface of the samples, because it might possess a different morphology from the bulk of the specimen, due to the fabrication procedure (uniaxial pressing with possible accumulation of silicone polymer on the pressed surfaces). Preliminary measurements performed on selected samples without removing this surface layer revealed indeed much lower values for k_1 and k_2

2.3 Results and discussions

In order to evaluate the effect of the foam morphology on the values of permeability constants, the samples were characterized by means of image analysis. Fig. 2.9 a) reports a SEM micrograph of a typical cell of the microcellular ceramic foam samples (sample S25), showing the interconnecting pores between adjacent cells (cell windows). Figure 2.9 b) shows the aspect of sample S10 after impregnation (for performing image analysis).

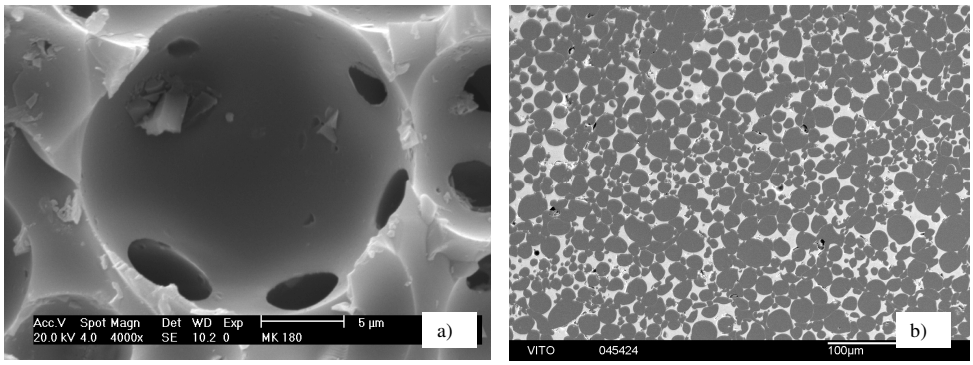

Figure 2.9-SEM pictures of a) sample S25 after pyrolysis (1200°C, N_2); b) sample S10 after impregnation for performing 2D image analysis.

The raw data obtained by image analysis were converted to 3D values to obtain the effective cell dimension using the following stereological equation[9,10]

$$D_{sphere} = \frac{D_{circle}}{0.785} \quad (2)$$

A more detailed description of the IA process can be found in Appendix 2.

In Figure 2.10 is shown the linear relationship existing between the cell size and the PMMA microbeads size (R^2=0.992) and between the cell window and the PMMA microbeads size (R^2= 0.95). The error bars for the cell and cell window size reflect the PMMA size distribution, and indicate a higher scattering of cell size data, which can be related to either a non-uniform cell formation during polymer burnout or the intrinsic difficulties in measuring three-dimensional objects from 2D pictures[9,11].

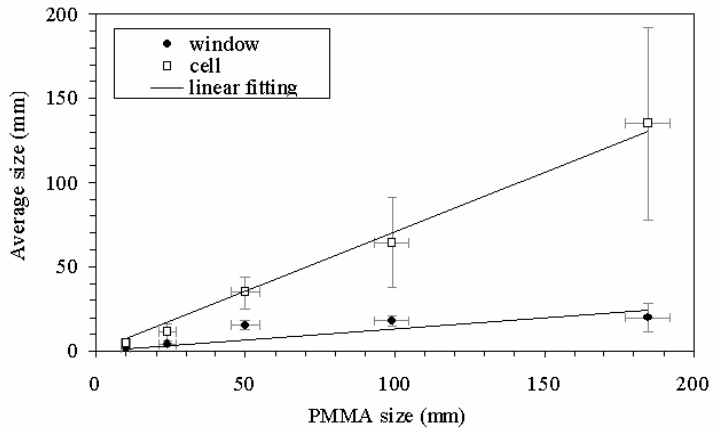

Figure 2.10- Dependence found between average cell and cell window size with PMMA microbeads size. PMMA microbeads average size is the value measured by Laser Diffraction, Cell average size is the value measured by Image Analysis, Cell window average size is the Value measured by Mercury Porosimetry.

Cell-windows seem to be originated by the contact of adjacent microspheres[1,4]. A limited increase in the cell window size is observed with increasing microbeads size. Besides the processing conditions, it has to be noted that further influence on the cell window size derives from the actual size distribution of the PMMA microbeads, which of course affects the packing factor under uniaxial pressing. Fig. 2.11 shows a typical pressure drop curve from which are fitted permeability constants k_1 and k_2. The parabolic trend of curve is confirmed by the exceptional correlation coefficient R^2 = 0.9992, which validates Forchheimer's equation, instead of the linear model expressed by Darcy's law. Such correlation agreement was observed for all tested samples.

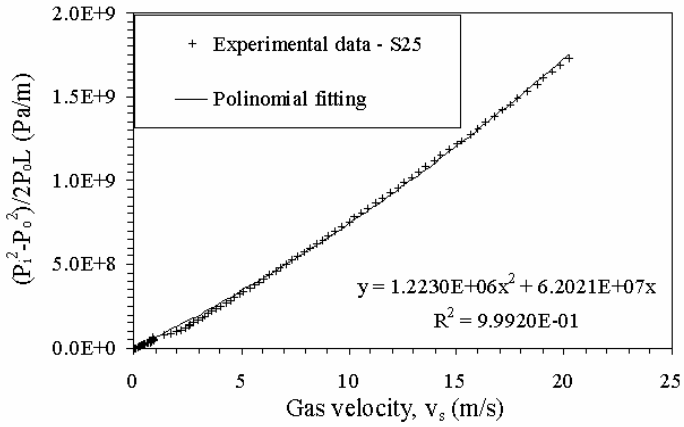

Figure 2.11-Experimental permeability curve for S25 sample. Solid line represents fitting of Forchheimer's equation (Eq. 1).

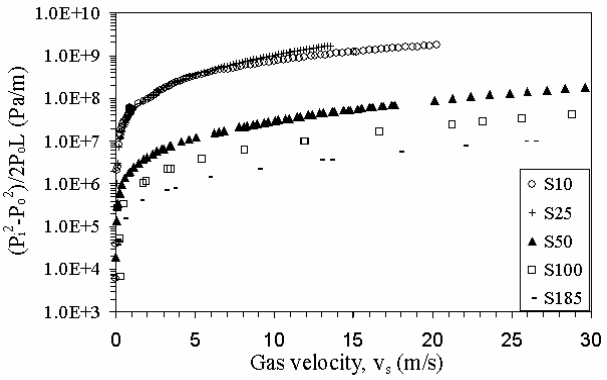

Figure 2.12-Experimental pressure drop curves for all samples tested in this work.

In Fig. 2.12, permeability curves for all samples analyzed in this work are shown for a large velocity range. The pressure drop parameter is plotted in a logarithm scale, since permeability level changed significantly depending on the size of PMMA microbeads.

A summary of the main microstructural and permeability results is reported in Table 2.4.

Table 2.4- Summary of the main physical characterization of microcellular foams. Where ε_o is the volume percentage of open porosity measured by Mercury Porosimetry, ρ is the bulk density measured after pyrolysis at 1200°C, $\rho_{rel} = \rho/\rho^*$ where $\rho^* = 2.24 g/cm^3$ is the density of SiOC dense sample pyrolized at 1200°C) ε_t is the total porosity expressed by Eq.3, k_1 and k_2 the Darcian and non-Darcian permeability constants coming from the interpolation of experimental values.

Sample	ε_0 (vol %)	ρ (g/cm^3)	ρ_{rel} (ρ/ρ^*)	ε_t (vol%)	k_1 (10^{-12} m^2)	k_2 (10^{-5} m)
S10	81.2	0.390 ± 0.022	0.174 ± 0.014	82.6	0.29	0.09
S25	78.4	0.260 ± 0.013	0.116 ± 0.008	88.4	0.45	0.02
S50	67.1	0.341 ± 0.024	0.152 ± 0.015	84.8	11.62	0.78
S100	91.8	0.284 ± 0.026	0.127 ± 0.016	87.3	37.15	3.69
S185	89.0	0.241 ± 0.015	0.108 ± 0.009	89.2	92.00	17.11

Some differences among the porosity data directly obtained from mercury porosimetry measurements and by computing it using the following equations were observed:

$$\varepsilon = 1-\rho_{rel} \quad (3)$$

$$\rho_{rel} = \rho/\rho^* \quad (4)$$

Where ε is the total porosity, ρ is the bulk density measured after pyrolysis at 1200°C and $\rho^* = 2.24$ g/cm^3 is the density of a dense MK-derived SiOC sample measured after pyrolysis at 1200°C. The low values measured for samples S25 and S50 can be

related to the presence of some closed porosity, while the higher porosity obtained by mercury porosimetry for sample S100 could possibly be attributed to the formation of some cracks during the measurement. Only the data obtained from mercury porosimetry, corresponding to the actual total open porosity, were used when plotting the permeability data.

Except for samples S10 and S25, a marked increase of permeability was observed with the increase in the PMMA filler size, as it can be indirectly inferred by the increase in cell and window sizes. No consistent direct correlation was observed between permeability and porosity values, possibly due to the limited range of total porosity available for this set of samples.

Experimental values of permeability constants k_1 and k_2 were then compared with those predicted by a model available in the literature, originally developed for granular beds.

Ergun, in 1952[12], proposed expressions to describe k_1 and k_2 for loose beds made of spheres, cylinders, tablets, nodules, round sand and crushed materials (glass, coke, coal, etc.) as a function of the volumetric void fraction, *i.e.*, porosity (ε), and the equivalent particle size (d_p). Nowadays, the major challenge in derivation of similar permeability models for ceramic foams is identifying a characteristic length that represents the cellular media realistically and thus replaces the particle size (d_p) of granular media.

A common approach in the literature suggests that d_p could be replaced by an equivalent pore or cell size, d_c, usually represented by the cylindrical form of the hydraulic diameter[2]. Therefore, Ergun equations for predicting permeability constants k_1 and k_2 for cellular media could be expressed as:

$$k_1 = \frac{2.25}{150}\varepsilon {d_c}^2 \qquad (5)$$

$$k_2 = \frac{1.5}{1.75}\varepsilon^2 d_c \qquad (6)$$

The numerical values 150 and 1.75 in Equations (5) and (6) are based on granular beds and may be replaced by values experimentally determined for each cellular material. In this work, both cell size and window cell size were tested as representative values for d_c in equations (5) and (6).

Figs.2.13 and 2.14 reveal that, despite the few experimental data available, Ergun equations give indeed a preliminary approximation for permeability constants of microcellular ceramic foams. The best prediction was achieved for d_c based on cell

size rather than on window cell size. For the Darcian constant, k_1, all calculated values displayed similar divergence from experimental data. On the other hand, for the non-Darcian constant, k_2, deviation seemed to increase with the reduction in cell size.

There are some factors that might help to explain the deviation found, and the most important are: a) not all the measured pore fraction may be available for fluid flow; b) the average pore size and average window size are in fact gross simplifications of a whole size distribution, in which each pore has its own weight on fluid flow; c) since Forchheimer's equation was firstly developed for granular beds, the use of just one parameter may not be sufficient to describe complex structures such as cellular media; d) the cell-windows density (the number of cell-windows per unit volume) is deeply affected by the size of PMMA microbeads, increasing with decreasing the microbeads size[10]. As previously observed in Fig. 2.10, the divergence between cell and cell window size is almost negligible for sample S10 and increases for larger cell sizes. The deviation from the Ergun model, considering the cell window size, increases for samples S100 and S185.

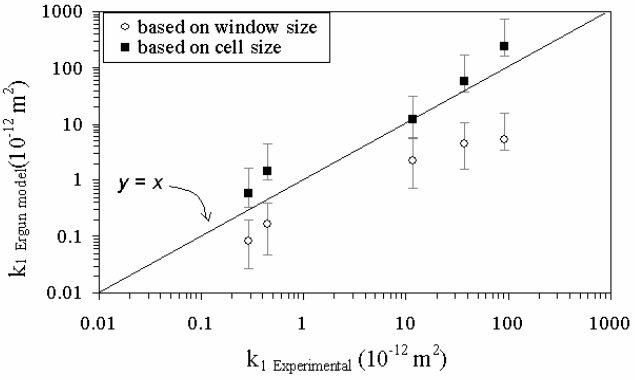

Figure 2.13-Comparison between the experimental Darcian permeability data and values predicted by Ergun equation (Eq. 3), utilizing the total porosity, cell size and cell window size.

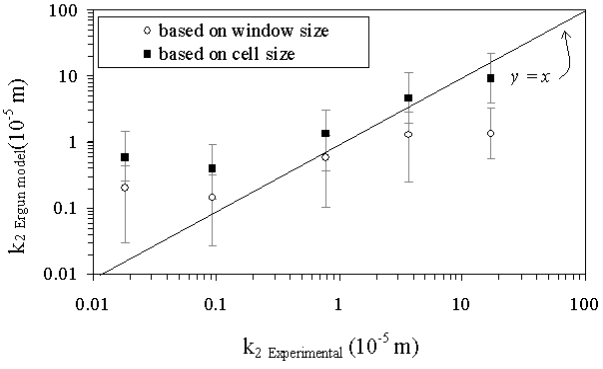

Figure 2.14-Comparison between the experimental non-Darcian permeability data and values predicted by Ergun model (Eq. 4), utilizing the total porosity, cell size and cell window size.

It is noteworthy to observe that the use of cell size values in predicting permeability constants gave consistently a better performance. The point is that for fluid flow

purposes, the pressure drop is the consequence of irreversible energy dissipation as heat, and caused by turbulence, changes in flow direction or in fluid velocity and by friction or shocks between fluid and solid walls. Therefore, it would be expected that pressure drop was higher for the more abrupt constrictions in the flow path, i.e., the smaller orifices, represented exactly by the cell windows, and not by the cell itself. In other words, pressure drop should be ruled by the size of windows instead of that of cells. The data reported in Fig.2.10 and Tab.2.4 show that the measurement of window size (a nearly 2D parameter) is more accurate than the measurement of cell size (a 3D parameter). This is because the cell window is obtained by an actual (physical) measurement rather than by the analysis of a SEM image, where some parameters (narrow cell size distribution, spherical cells, etc.) must be assumed in order to obtain the 2D to 3D transformation. Furthermore, before performing IA, some digital image processing, such as grey scale thresholding, must be realized in order to get a suitably contrasted image. This step can introduce some artifacts in the cell size distribution.

Even though an insufficient number of samples was available for a reliable statistical analysis, numerical values in Ergun equations (5) and (6) were fitted according to the least-squares method to represent the particular permeability data set obtained in this work. Corrected Ergun equations were:

$$k_1 = \frac{2.25}{357.1}\varepsilon d_c{}^2 \tag{7}$$

$$k_2 = \frac{1.5}{3.63}\varepsilon^2 d_c \tag{8}$$

It is important to note that such corrections referred only to a linear shift in all calculated data, and not to a change in trends. The poorer correlation found between experimental and calculated values for the non-Darcian constant k_2, even after adjustment of Ergun equation, is coherent with the fact that this parameter is always much more sensitive to structural parameters than k_1, and therefore much more susceptible to inaccuracies in measured values of porosity and pore size. Thus, although an improvement is achieved in predictability, Equations (7) and (8) must not be generalized or indistinctly employed for other microcellular bodies. Figs.2.15 and 2.16 show the apparent improvement in prediction obtained after correction of numerical values in Equations (5) and (6).

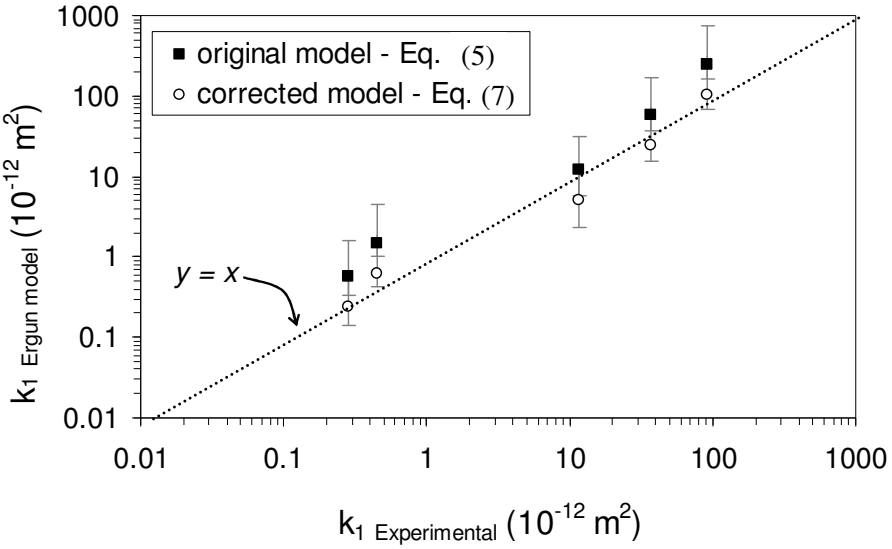

Figure 2.15-Comparison of original and corrected Ergun equations for predicting Darcian permeability constant k_1.

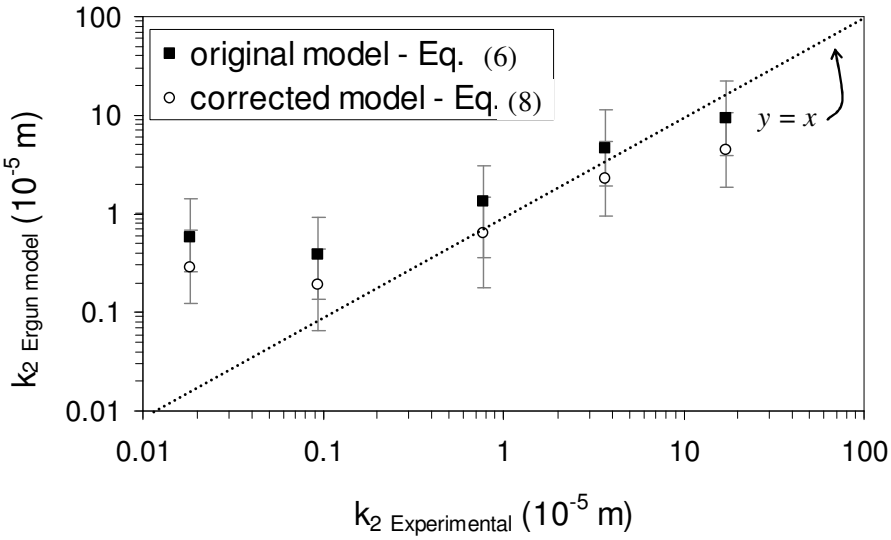

Figure 2.16-Comparison of original and corrected Ergun equations for predicting non-Darcian permeability constant k_2.

Recently, Innocentini et al.[2] have shown that there is a noticeable numerical relationship between permeability constants k_1 and k_2 for a large collection of porous media, from concretes to ceramic foams (Fig. 2.17). The reasons for this unique trend have not yet been fully explained, but it is helpful to classify porous media in groups of similar permeability levels or to establish a permeability target for processing a porous ceramic to a specified application. It can be observed in Fig.2.17 that samples

prepared in this work match the category of granular and fibrous filters, which in fact confirms microcellular foams as alternative filtering membranes for aerosol and liquid filtration processes. Furthermore, permeability level varied several orders of magnitude according to the chosen processing variable (size of polymeric microbeads), indicating the feasibility of the technique for permeability optimization and for expanding the range of fluid dynamic applications for microcellular ceramic foams.

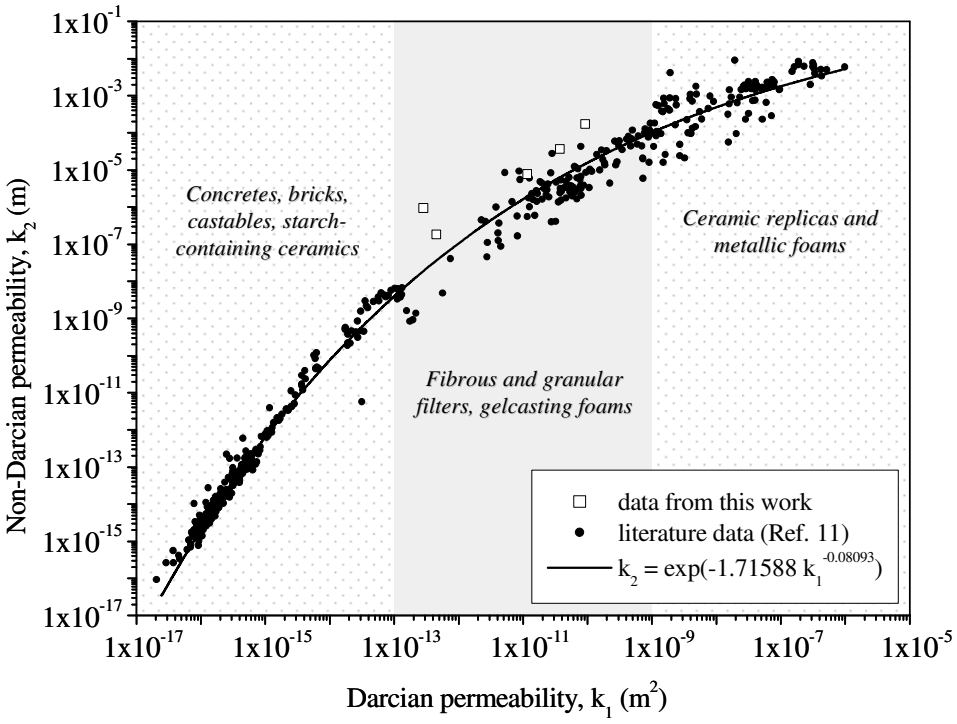

Figure 2.17-Location of permeability data of microcellular ceramic foams obtained in this work in a comprehensive data map available in the literature[11].

Concerning the use of microcellular ceramic foams developed in this work as filtering media, two important fluid dynamic aspects that must be evaluated are the pressure drop level for a typical filtration velocity and the verification of the dominant term in Forchheimer's equation (either the linear term $\mu v_s/k_1$ or the quadratic term $\rho v_s^2/k_2$). The former aspect is important to quantify the power requirements (blower, compressor or pump) for an industrial application, whereas the latter aspect regards how oscillations in pressure drop due to particle accumulation on filter surface may affect the operational flow rate or vice-versa.

Fig.2.18 shows pressure drop curves simulated from permeability data of samples S10 to S185 for a typical aerosol filtration at ambient conditions (absolute gas pressure of 760 mmHg and air temperature of 25°C). For this process, gas velocity is usually lower than 10 cm/s and pressure drop for the clean filter does not exceed 20

cmH_2O (2000 Pa). According to Fig.2.18, only samples S10 and S25 do not match these specifications, even though their pore size ranges are interesting for collecting fine particles. An alternative in this case would be the production of a thinner filtering layer or of monolithic bodies with varied geometries, since pressure drop is reduced linearly with the membrane thickness. Another possibility would be the use of microcellular foams S10 and S25 in filtration processes in which flue gases are already at higher pressures, such as in catalytic combustion or in diesel exhaust systems[13]. Indeed, SiOC-based ceramic foams possess a good thermal shock resistance and refractoriness, making them good candidates for filtration applications in severe environments[14].

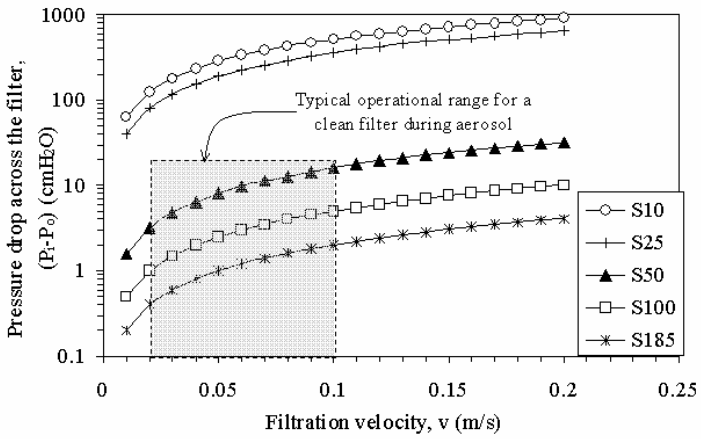

Figure 2.18-Simulation of pressure drop curves across clean filtering membranes based on permeability data of samples prepared in this work. Assumed conditions were: Fluid: dust laden air, P_o = 760 mmHg, $T_i = T_o$ = 25°C, $\mu = 1.86x10^{-5}$ Pa*s, ρ = 1.19 kg/m^3, L = 1 cm

In Fig.2.19 the relative contribution of the linear and quadratic terms of Forchheimer's equation on total pressure drop of each sample is shown. In all cases, it is observed that for typical filtration velocity below 10 cm/s, pressure drop is at least 98% due to viscous effects, which implies that Darcy's law for compressible fluids, $[P_i^2-P_o^2]/2PL = \mu v_s/k_1$, could be correctly used for simulation and control of operational flow conditions.

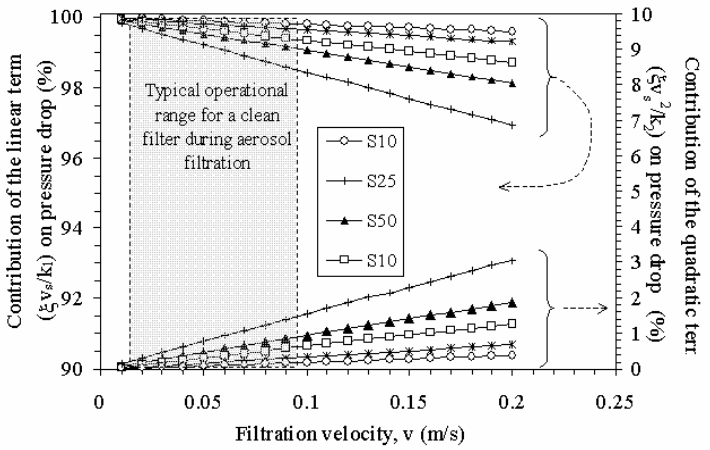

Figure 2.19-Relative weight of linear and quadratic terms of Forchheimer's equation for a typical aerosol filtration process.

2.4 Conclusions

Microcellular SiOC foams were produced by the sacrificial template method. Warm-pressing temperature and the sacrificial filler (PMMA) burn-out were the most critical steps in the production process. Warm-pressing temperature can be considered a double purpose step: it allows for preceramic polymer crosslinking and for the moltent preceramic polymer flow through the beads. By this route an uniform coating of the PMMA spheres is realized. Crosslinking is responsable of shape retention during the PMMA burn-out. The compression strength of the foams revealed a linear dependance with the PMMA size used as pores source ranging from 6.3 to 1.2 MPa. Cell-size (measured by the IA method) and cell-window size (measured by mercury porosimetry) revealed a linear dependance with PMMA size and a spherical shape.

The gas permeability of SiOC microcellular ceramic foams was evaluated as a function of morphological parameters (average cell and cell window size), for samples with a restricted range of relative density values. The results show that permeability increases with increasing cell window and cell window size. Furthermore, permeability varied several orders of magnitude according to the size of the sacrificial filler used to generate the porosity in the ceramic material, indicating that it is possible to tailor this parameter according to requirements of the specific application considered.

Permeability constants fitted according to Ergun equations for granular media showed a reasonable agreement with experimental data, despite the differences in morphology of microcellular foams and granular media. Preliminary analysis of permeability data for airflow at velocities below 10 cm/s revealed that the pressure drop is mostly ruled by viscous effects, which validates Darcy's law for this type of

application and suggests the feasibility of microcellular SiOC foams as filtering media for typical aerosol filtration processes.

The good control on the process parameter opens a wide variety of new applications mainly related to the functionalization for a specific application.In the next chapter the functinalization of SiOC microcellular foams by the addition of magnetic nano- and micro-particles will be discussed.

In chapter 4 SiOC foams possessing hierarchical porosity will be discussed.

Acknowledgements: this work, with the title “Gas Permeability of Microcellular Ceramic Foams” was submitted on October 2006 and accepted on February 2007, to the *Journal of Industrial and Engineering Chemical Research*. I wish to acknowledge the authors: M.D.M. Innocentini, Universidade Federal de Sao Carlos-Brazil and S. Mullens, VITO, Mol-Belgium.

References

[1] Colombo, P., Bernardo E., Biasetto L. *J. Am. Ceram. Soc.*, 87, 152-54 (2004)
[2] Innocentini, M. D. M.; Sepulveda, P. and Ortega, F. S. in *Cellular Ceramics: Structure, Manufacturing, Properties and Applications*, Scheaffler, M. and Colombo, P. eds., WILEY-VCH Verlag GmbH, Vehineim, Germany, 313-341(2005)
[3] Harshe R. et al. *J. of the Eu. Ceram. Soc.,* 24, 3471–3482 (2004)
[4] Colombo P, Bernardo E, *Composites science and technology,* 63, 2353-59 (2003)
[5] Gibson LJ, Ashby MF, *Cellular solids, structure and properties*. 2nd edition Cambridge University Press (1999)
[6] Brezny R., Green DJ, Mechanical behavior of cellular ceramics. In: Swain M, editor. Materials science and technology, a comprehensive treatment, vol.11 Structure and Properties of Ceramics. Weinheim: Wiley-VCH, 463-516 (1993)
[7] Innocentini, M. D. M.; Salvini, V. R.; Pandolfelli, V. C. and Coury, J. R., The Permeability of Ceramic Foams, *Am. Ceram. Soc. Bull.*, *9*, 78-84 (1999)
[8] Moreira, E. A.; Innocentini, M. D. M. and Coury, J. R. Permeability of ceramic foams to compressible and incompressible flow, *J. Eur. Ceram. Soc.*, *24*, 3209-3218 (2004)
[9] Mullens, S.; Luyten, J. and Zeschky, J. in Cellular Ceramics: Structure, Manufacturing, Properties and Applications, Scheaffler, M. and Colombo, P. eds., WILEY-VCH Verlag GmbH, Vehineim, Germany, 227-66 (2005)
[10] ASTM standards, Standard test method for cell size of rigid cellular plastics, ASTM D 3576, 919-922 (1997)
[11] Innocentini, M. D. M.; Salvini, V. R.; Macedo, A. and Pandolfelli, V. C., Prediction of Ceramic Foams Permeability using Ergun's Equation, *Mater. Res.*, *4*, 283-89 (1999)
[12] Ergun, S., Flow Through packed columns, *Chem. Eng. Progress*, *2*, 89-94 (1952)
[13] Fino, D. and Saracco, G. in Cellular Ceramics: Structure, Manufacturing, Properties and Applications, Scheaffler, M. and Colombo, P. eds., WILEY-VCH Verlag GmbH, Vehineim, Germany, 416-38 (2005)
[14] Colombo, P.; Hellmann, J. R. and Shelleman, D. L. Thermal Shock Behavior of Silicon Oxycarbide Foams, *J. Amer. Soc.*, *9*, 2306-12 (2002)

Chapter 3

Magnetic Functionalization

3.1 The effect of filler addiction on the electromagnetic properties of PDCs

Ceramic manufacturing from Si-containing preceramic polymers based on poly(silanes), -(carbosilanes), -(silazanes), -(borosilazanes) and mixtures thereof have gained growing interest due to their unique combination of low temperature processing, versatile shaping, microstructure and property tailoring capabilities[1,2,3]. As reported in §1.2, processing preceramic polymers into ceramic products involves shaping of a low viscous polymer precursor, subsequent curing and pyrolysis at temperatures above 800 °C. Due the pronounced density differences between the polymer (1–1.2 $g \cdot cm^{-3}$) and the ceramic phases (2–3 $g \cdot cm^{-3}$), shrinkage of up to 70 vol.% may occur which gives rise for extended porosity formation or even cracking in the pyrolyzed ceramic residue material. Manufacturing of bulk components from preceramic polymers, however, is facilitated when the polymer is loaded with a filler powder typically in the range 30–50 vol.% (Figure 3. 1). Inert filler powders such Al_2O_3, SiC, B_4C, Si_3N_4, etc., as well as reactive fillers like Ti, Cr, Mo, B, $MoSi_2$, etc., which may react with the solid and gaseous decomposition products of the polymer precursor to form carbides, oxides, etc., were successfully used to reduce the polymer-to-ceramic shrinkage and to improve the mechanical properties of non-oxide as well as oxide based polymer-derived ceramics[4,5,6].

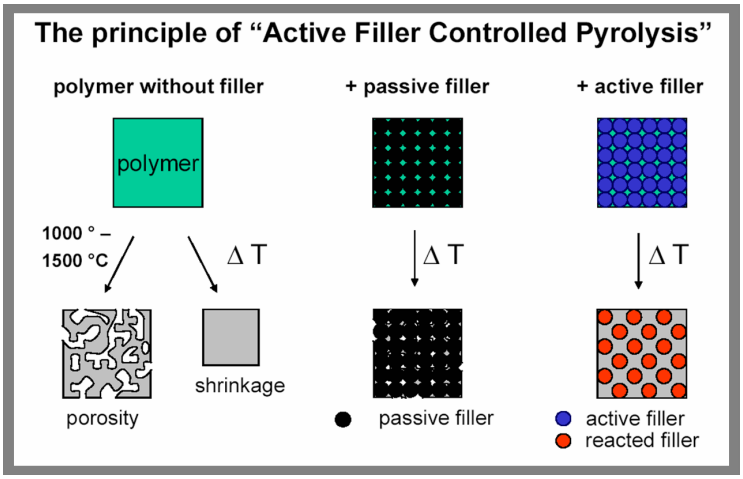

Figure 3. 1- Left: shrinkage after pyrolysi of a preceramic polymer[7]; right: passive and active filler controlled pyrolysis[4].

By this route near net-shape polymer derived ceramic components were produced and moreover additional functional properties (electrical, magnetic, corrosion resistance) can be obtained.

The filler/matrix interactions as function of pyrolysis temperature are a key point for the final composite material.

For exemple, Wei et al.[8] have recently studied these interactions in a Si-filler-loaded polymethilsiloxane.

Depending on the processing temperature and atmosphere, the Si-filler may remain unreacted or react to form SiC or Si_3N_4, respectively. While nitride and oxinitride ceramic compositions are formed in nitrogen reaction atmosphere, carbide and oxicarbide ceramics result when the pyrolysis is carried out in argon atmosphere.

In the reported work, the effect of pyrolysis temperature (1000, 1250, 1400 °C, Argon atmosphere) on the interfacial bonding and β-SiC formation was investigated.

Below 1000 °C, no reactions occurred and Si can be considered as an inert filler dispersed in the Si–O–C matrix. Above 1000 °C, ß-SiC formed on the Si-filler surface gave rise for an intimate filler-to-matrix bonding. The SiC formation is likely to proceed via a solid–gas reaction involving CO as the major carbon source. CO formation and transport to the reaction site at the filler/matrix interface is facilitated by a high porosity in the polymer-derived Si–O–C matrix. Thus, control of the activity of elemental carbon in the Si–O–C matrix material is a key factor to influence the partial pressure of CO and hence the interface bonding process in carbide forming active filler systems. In Figure 3. 2 a schematic overview of the reactions mechanism is reported.

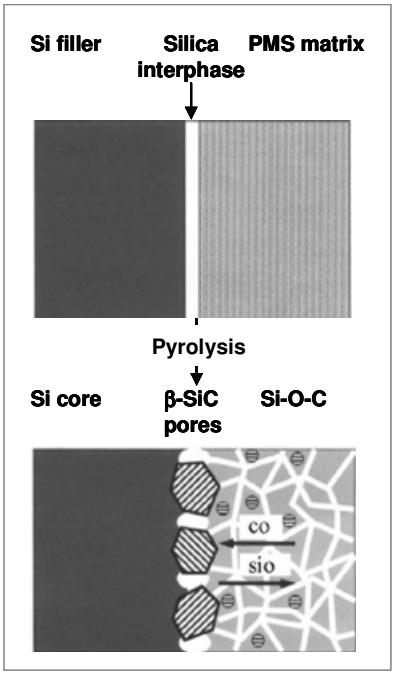

Figure 3. 2- A schematic model of the SiC formation reaction at the filler/matrix interface[8].

Depending on the composition of the preceramic polymer and the processing conditions, the electrical properties of the pyrolyzed ceramic material may vary over a wide range of specific electrical resistance. Amorphous Si-C-N and Si-B-C-N pyrolysis products of polysilazanes and borosilazanes were found to behave as semiconductors over a wide temperature range[9].

The electrical conductivity of polysiloxane-derived Si-O-C ceramics was found to be dominated by the precipitation of excessive carbon at temperatures above 800°C (polyphenylsiloxane) and 1400°C (polymethylsiloxane), respectively[10]. Decomposition of hydrocarbon fragments resulting from the cleavage of the functional groups bonded to silicon ($Si–C_6H_5$, $Si–CH_3$) resulted in the precipitation of clusters of turbostratic carbon. With increasing temperature these carbon clusters grow and may coalesce by edge-to-edge linkage of neighboring basic structural units to form an interconnected, percolating network (cluster size to infinity) of turbostratic carbon ribbons[11]. Above the percolation threshold direct contact of carbon particles allows electron conduction, whereas at lower carbon fractions semiconducting behavior is attributed to thermal-fluctuation-induced tunneling of electrons among evenly distributed charge carrier clusters in the amorphous Si-O-C-H network.

Adding filler materials with a high electrical conductivity such as metals or intermetallics offers the possibility of creating polymer-derived ceramic composite materials of low resistance even at low heat treatment temperatures.

Polysiloxanes loaded with 40–50 vol% of $MoSi_2$ filler powder had a specific electrical resistance of less than $10^{-4}\Omega$ cm after pyrolysis at temperatures above 1000 °C[12]. The $MoSi_2$-containing Si-O-C composite ceramics exhibit excellent oxidation stability and creep resistance up to 1500°C and they offer reasonable strength (modulus of rupture ≈ 450 MPa) and toughness (critical stress intensity factor ≈ 4 $MPa \cdot m^{1/2}$) at a $MoSi_2$ volume fraction of 40%. These properties make them an interesting material for novel heating devices of complex geometrical shapes, in the electrical and automotive industries.

As reported by Cordelair et al.[13], during heating of a polymethylsiloxane/$MoSi_2$-filler mixture in inert atmosphere a series of irreversible structural rearrangement and interface reactions occur which give rise to a complex, nonlinear behavior of the electrical resistance with temperature.

Saha et al.[14] prepared polymer-derived SiCN-Fe composites by mixing a liquid ceramic precursor and Fe_3O_4 particles and then reducing ferrite to α-iron during pyrolysis.

This processing route takes advantage of the transient reactivity of the polymer during pyrolysis (related to the evolution of hydrocarbons) to allow for “chemical” incorporation of the dispersed phase into the composite. By this technique soft ferromagnetic bulk components were produced.

Hauser et al.[15] realized soft-ferromagnetic SiCN-Fe and SiCN-Co composites by addiction of metal carbonyl compounds $Fe(CO)_5$ and $Co_2(CO)_8$ in the ceramic precursor. By this route nanocrystals of Fe and Co were produced inside the SiCN matrix.

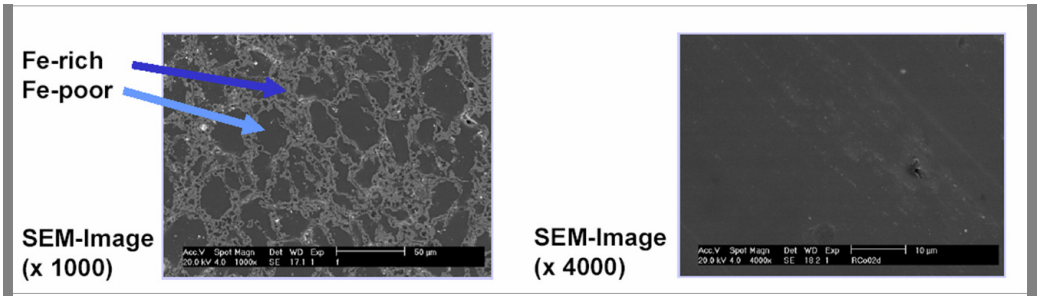

Figure 3. 3- Left: SiCN-Fe compoite loaded with Fe powders; right: SiCN-Fe composite loaded with $Fe(CO)_3$ [15]

In Figure 3. 3 a comparison between SiCN loaded by Fe powders filler (left) and by metal carbonyl compounds (right) is reported. As can be observed, the metal carbonyl compounds provide for an intimate mixing between the liquid ceramic precursor and the carbonyl compounds, this resulting in a homogeneous structure after pyrolysis.

Colombo et al.[16] reported on the electrical functionalization of SiOC macrocellular ceramic fomas by addiction of $MoSi_2$, α-SiC, graphite, copper acetate and Cu_2O.

Macrocellular ceramic foams were produced by the polyurethane direct foaming technique and fillers were added in the starting mixture.

No reports in the leterature are available for such functionalization in microcellular ceramic foams.

Ceramic foams possessing magnetic properties can find applications as Electromagnetic Filters, Radar Active Materials for stealth components, Induction Heating Elements, and Catalysts.

In the present work we propose two simple processing route to produce PDCs microcellular ceramic foams belonging to the class of the soft-ferromagnetic materials. This goal has been reached by adding Iron Silicide micro-particles to the starting mixture (PMS and PMMA) and then processing as reported in Chapter 2.

The second approach consists in the deposition of metalcarbonyl compounds on the surface of SiOC microcellular foams and the pyrolysis of the organic compounds at different temperatures.

3.2 Magnetic SiOC microcellular ceramic foams by addiction of Iron Silicide powders

3.2.1 Experimental

SiOC Microcellular Ceramic Magnetic Foams (MCMFs) were prepared using a commercially available poly-siloxane (MK, Waker Chemie, Burgausen, Germany) with a structure comprised of Si-O bonds with -OH and -CH_3 substituting groups (denominated as Preceramic Polymer, PP, in the following).

The PP was dry mixed with Iron Silicide (IS) micro-sized powders (Iron Silicide Type 1, Steward Advanced Materials, Chattanooga, TN, average diameter 9 μm) and Poly-methyl-methacrylate microbeads (PMMA) with 25 μm nominal dimension (Altuglas BS, Altuglas International, Arkema Group, Rho (MI), Italy) by mechanical ball-milling for 1 hour. The mixture was then warm-pressed at 130°C, 15 MPa for 15 min and then rapidly cooled for 5 minutes.

After warm-pressing the samples were heat treated in air at 300°C for 2 hours at a heating rate of 0.5°C/min in order to burn-out the PMMA microbeads. By this route, preceramic microcellular foams were obtained[17]. The polymer to ceramic conversion was realized by heating under nitrogen flow up to 1200°C for 2 hours at a rate 2°C/min, producing ceramic samples of 32 mm diameter and 5.5 mm thickness.

In Table 3. 1 an overview of the prepared samples is reported. The sample labelled S100 is constituted of the as received IS powders. Samples S10010 and S10012 are constituted by the as received iron silicide powders heat treated under nitrogen flow at 1000°C and 1200°C, respectively. Sample labelled as S40300 was prepared by mixing 40 wt.% of IS and 60 wt.% of PP, powders were ball-milled for 20 min and then heat treted in air at 300°C (heating rate 2°C/mmin, 120min). As concern samples S3012, S4010, S4012, S5012 and S6012, the weight ratio between PMMA and PP + IS was kept constant at 80 to 20. The IS weight percentage in the table refers to the PP and IS total amount (i.e. sample labelled S3012 is 30 wt% IS, 70 wt% PP, pyrolyzed at 1200°C).

Table 3. 1-Overview of the prepared samples

Sample	IS wt. %	PP wt.%	Pyrolysis T (°C)
S100	100	0	RT
S10010	100	0	1000
S10012	100	0	1200
S40300	40	60	1200
S3012	30	70	1200
S4010	40	60	1000
S4012	40	60	1200
S5012	50	50	1200
S6012	60	40	1200

TGA-DTA analysis (10°C/min, 1210°C, nitrogen flow, STA 410 NETZSCH-Gerätebau GmbH, Selb, Germany) were performed on the as received iron silicide powders (S100) and on IS and PP polymer mixture (S40300) to study the phase transformation temperatures during pyrolysis. TGA-DTA analysis during the polymer to ceramic conversion of the MK polymer were previously reported (Chapter 2, Fig.2.3). X-Ray Diffractometry (Philips PW 1710, Cu Kα radiation) was performed in order to detect the phase composition of the as received iron silicide powders and the possible interactions with the SiOC matrix. The structure of the as received iron silicide powders and of the Fe-Si alloys formed within the SiOC ceramic matrix were also investigated by Mossbauer Spectroscopy (at room temperature, using a ^{57}Co:Rh source, at constant acceleration). The magnetic hysteresis parameters were measured at room temperature using a vibrating sample magnetometer (VSM – Model 9600-1, LDJ Electronics, Inc., Mich., USA) up to an applied field H =1.6 Tesla. The operating principle requires oscillating the sample being tested at an uniform frequency and displacement while exposing the sample to a magnetic drive field which is slowly progressing through a pre-programmed cycle. The magnetometer was operating at room temperature at a frequency of 85Hz using nickel sphere reference. The samples were desiccated before the analysis. Scanning Electron Microscopy (Cambdridge Stereoscan 120) was performed to observe the morphology of the foams. Sample shrinkage during processing was calculated by comparing samples dimension before PMMA burn-out and after pyrolysis.

The crushing strength of the foams was measured at room temperature by compression testing, using UTM (Model 1121, Instron Danvers, MA) with a cross-head speed of 0.5 mm/min, on samples of nominal size of 10x5x3.5 mm. Each data point represents the average value of five individuals tests.

3.2.2 Results and Discussion

In Table 3. 2 the main properties of the IS powders, as reported in the manufacturer's technical data sheet, are shown.

Table 3. 2- Technical data sheet for the iron silicide powders

SSA (m^2/g)	0.45
M_s (Emu/g)	84
True Density (g/cm^3)	6.08
Moisture %	0.03
Average Dimension (μm)	9±5

DTA-TGA investigations on sample S100 revealed the presence of one exothermic peak at 494°C, and two endothermic peaks at 1053°C and 1210°C, respectively. The weight loss was negligebele (Figure 3. 4 a).

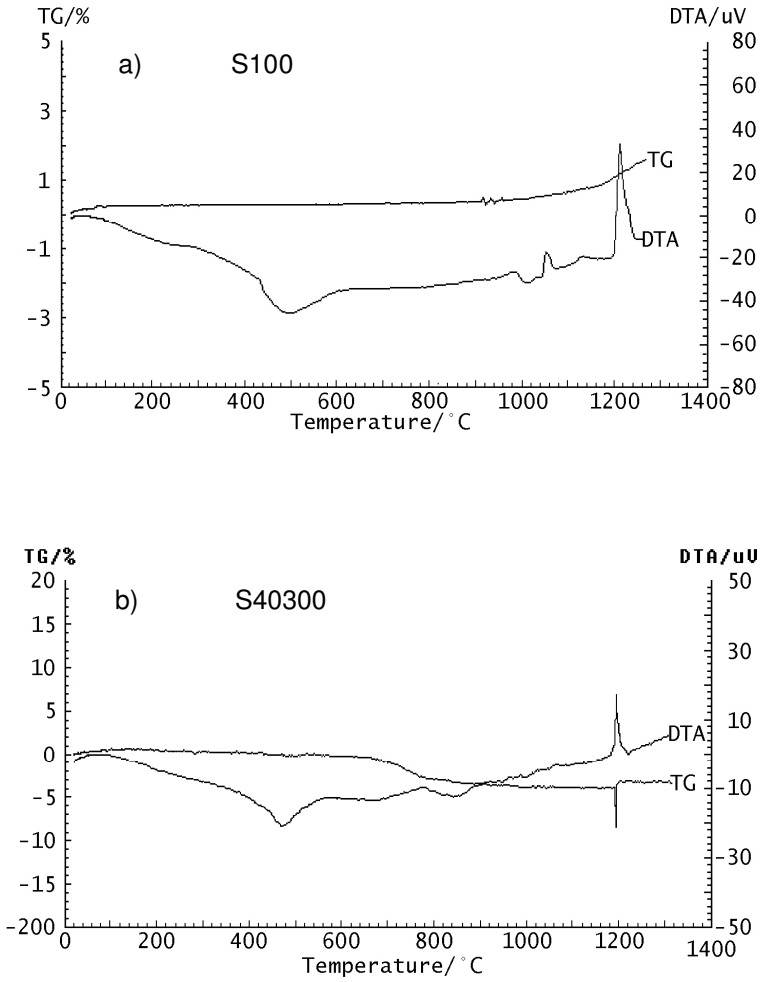

Figure 3. 4- TGA, DTA measurements on: a) sample S100 and b) sample S40300.

In Figure 3. 5 XRD diffraction spectra of the as received IS powders and of IS powder after heat treatment up to 1000°C and 1200°C under nitrogen flow (heating rate 10°C/min, dwelling time 10 minutes) are reported.

The as received iron silicide powders were confirmed to be $Fe_{1-x}Si_x$ ($0.25 < x < 0.50$) alloys. Inside this compositional range three main phases were detected: FeSi, Fe_5Si_3 and Fe_3Si (see Figure 3. 5).

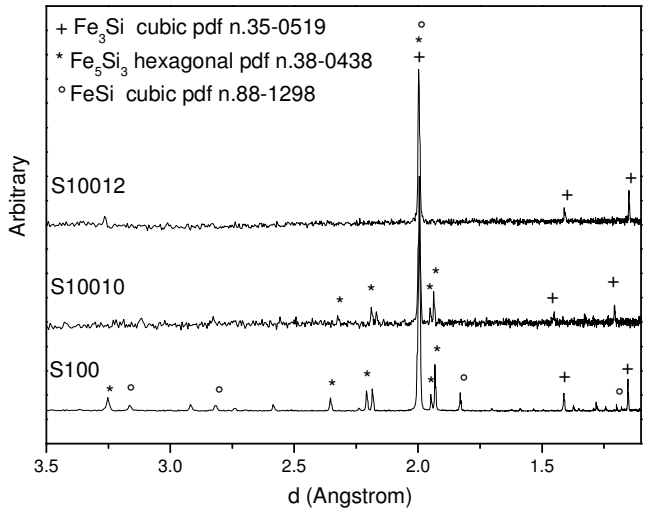

Figure 3. 5- Diffractometre spectra of IS powders as function of heat treatement conditions. S100, as received powders, S10010, IS heat treated up to 1060°C under N_2 flow, S10012, IS powders heat treated under nitrogen flow up to 1210°C.

The FeSi phase, Si 50 at.%, is a narrow-gap non-magnetic semiconductor.[18,19] The bulk stable iron-monosilicide has a simple cubic Bravais lattice with four Fe atoms and four Si atoms in unit cell with the lattice constant a= 0.4493 nm.[20] The DO_3 cubic symmetry (typical for Fe_3Si structure) can be obtained for Si content up to Si 34% although traces of Fe_5Si_3 can also be generally detected.[21] The Fe_3Si cubic structure can be decomposed in two elementary cubic sub-networks made up of BCC and CsCl-type sub-cubes, where the main cubic sites are entirely occupied by iron and the other sub-cubic sites are occupied by both iron and silicon acting as substitutent.[22] The typical symmetry for Fe_5Si_3 is hexagonal.

As it can be observed in Figure 3. 5, after heating the pure iron silicide powder at 1000°C the metastable FeSi phase was converted to Fe_3Si and Fe_5Si_3 phases; this phase transformation can be related to the peak at 494°C from DTA analysis. After heating up to 1200°C the only phase detected was the Fe_3Si cubic structure.The first endothermic peak at 1053°C from DTA measurements can then be related to the transformation of the Fe_5Si_3 phase in the Fe_3Si cubic structure. The high intensity endothermic peak from DTA at 1200°C can be attribuited to the melting of the Fe_3Si phase (Figure 3. 6).[23]

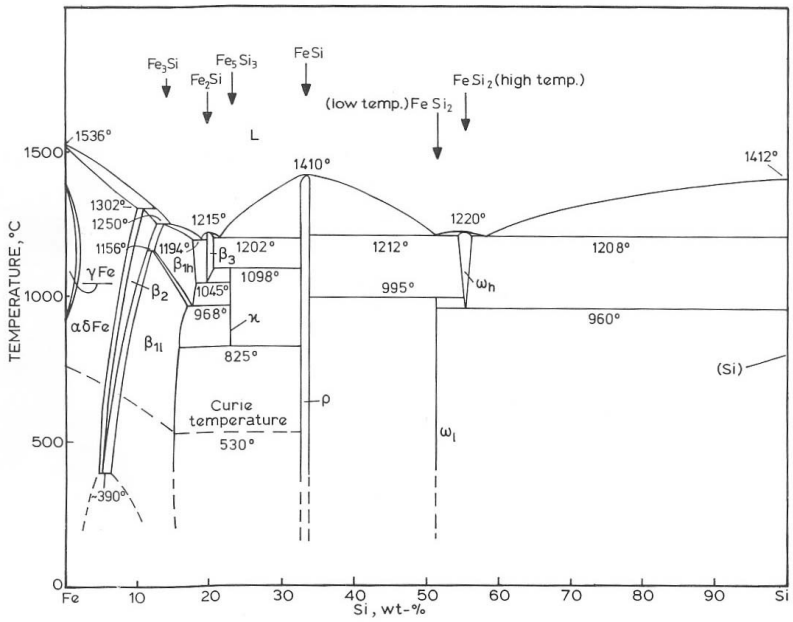

Figure 3. 6- Fe-Si Phase diagram [23].

Table 3. 3 shows the magnetic parameters of the as received powders and after heating at the above-mentioned temperatures.

Table 3. 3-Magnetic properties of the IS powders. B_s , B_r , H_c and μ are the maximum Magnetic Saturation, Remanence , Coercivity and Permeability, respectively.

Sample	Bs (emu/g)	Br (emu/g)	Hc, Oersted	μ, Permeability
S100	10.95	0.053	14.54	4.926
S10010	11.01	0.04	6.55	3.864
S10012	11	0.044	8.20	3.557

As can be observed from Table 3.3, no relationship between annealing temperature and H_c values can be extrapolated. The decrease of H_c with increase of temperature might be due to the reduction of the anisotropy constant K and B_s with annealing temperature. The minor changes in the magnetic properties of IS powder can be attributed the modification of the average size of the micro(nano)crystallites with the annealing temperature.

The phase transformation occurring in the iron silicide powders upon heating was responsible for the increase of B_s values. The paramagnetic phase (Si 50 at.%) was converted to the ferromagnetic Fe_3Si and Fe_5Si_3 after 1000℃, and a second transformation occurred at 1210℃. At this temperature the only phase detected was Fe_3Si.

In order to verify the effects and possible interactions of the SiOC matrix with the IS powders during pyrolysis, samples with different IS wt. % were prepared. DTA-TGA analysis on sample S40300 (Figure 3. 4b), revealed an endothermic peak at 470℃

and two exothermic peaks at 767°C and 1193°C respectively (weight loss 4.10%), these corresponding to the phase transformation detected in the pure IS powders. The limited shift of phase transformation temperatures to lower values can be related to the presence of the PP and its decomposition products deriving from pyrolysis.

In Figure 3. 7, the XRD patterns of samples S3012, S4010, S4012, S5012, S6012 are reported. The only Fe-Si phase detected for samples pyrolyzed at 1200°C was the Fe_3Si cubic structure. However starting from sample S4012, the formation of Cristobalite and $\alpha-$ Quartz was observed. This behavior was more evident with increasing the Fe-Si weight amount. These spurious phases were detected only at the surface of the ceramized specimens; indeed, after removing a few hundred microns from the surface of the specimens, no pure silica phases were detected. In samples S5012 and S6012, the shoulder in the main peak can be attribuited to the presence of α-Fe in the structure.

This finding points to the fact that the silicon employed in the Cristobalite and $\tilde{\alpha}$-Quartz formation was given by the IS powders, that after pyrolysis gave rise to high Fe containing phases. The SiO_2 crystalline phases started forming at temperature higher than 1000°C, and were never detected in sample S4010. Moreover, being the IS phases evolution driving from low to high Fe content, we are induced to think that the silicon employed in the reactions is coming from the IS powders and not from the matrix.

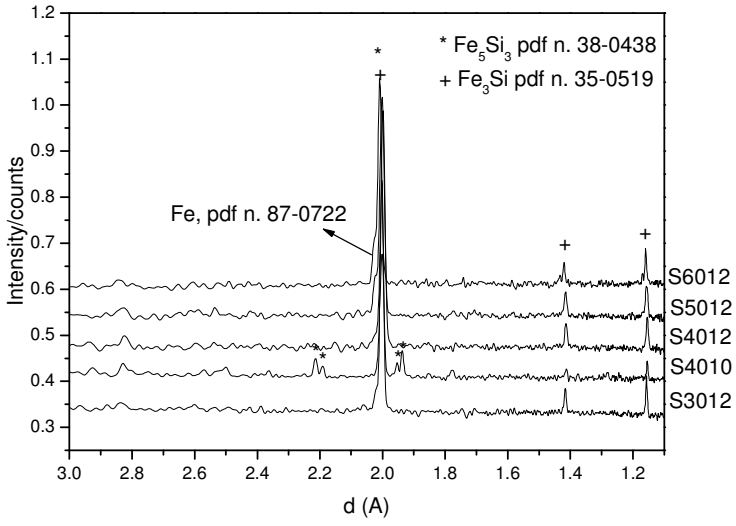

Figure 3. 7- XRD plots of SiOC/Fe-Si microcellular foams.

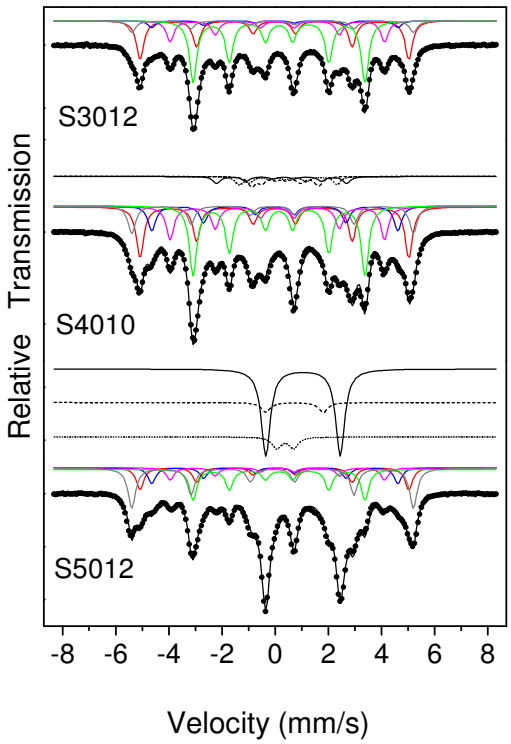

Figure 3. 8- Comparison of Mossbauer spectra for samples S3012, S4010 and S5012

Mossbauer Spectroscopy performed on S3012, S4010, S5012 confirmed these results (Figure 3.8). S3012 contained only disordered Fe_3Si in which Fe exhibited 5 different local enviroments. S4010 contained 89 wt. % disordered Fe_3Si and 11 wt. % Fe_5Si_3, as calculated from the Mossbauer spectra area. S5012 (with surface layer) contained majoritary disordered Fe_3Si (65.1% of Mossbauer spectra area), Fe-Si-O phases where Fe valence is +2 (31.2% of Mossbauer spectra area), and some minor Fe-Si-O phase where Fe valence is +3 (3.5% of Mossbauer spectra area). In all the samples there were 5 inequivalent positions, such as for a disordered Fe-Si solid solution (Table 3. 4). The 5 inequivalent positions correspond to 0, 1, 2, 3, 4 Si nearest neighbour atoms for the central Fe with respectivly hyperfine magnetic fields of about 33T, 31T, 29T, 25T, and 20T.

Table 3. 4- Magnetic parameters from Mossbauer measurements: nn, nearest neighbours; IS, isomer shift; QS, quadrupole splitting; HF, hyperfine magnetic field.

Si nn for Fe	IS (mm/s)	QS(mm/s)	HF (T)	Occupancy	Sample
0 Si	0.00	-	32.85	0.08 0.13 0.32	S3012 S4010 S5012
1 Si	0.07	-	31.35	0.28 0.25 0.18	S3012 S4010 S5012
2 Si	0.09	-	28.70	0.05 0.12 0.13	S3012 S4010 S5012
3 Si	0.18	-	25.01	0.15 0.16 0.11	S3012 S4010 S5012
4 Si	0.25	-	20.04	0.44 0.34 0.26	S3012 S4010 S5012

Table 3. 5 shows the value of the magnetic parameters at a moment range of 1emu.

It is well known that magnetic properties of materials and in particular ferrites are influenced by numerous factors such as cationic composition, microstructure, purity, homogeneity and non-stoichiometry. In the literature there is no report about the preparation and characterization of SiOC ceramics possessing magnetic properties, but Saha et al. recently investigated polymer-derived SiCN materials containing α-Fe[14].

Table 3. 5- Magnetization parameters measured by VSM: B_s is the magnetic induction of the measured sample, B_s^{IS} is the recalculated value, as function of the IS wt.% after pyrolysis, B_r is the remaining induction magnetization, H_c the coercive force and B_r/B_s the magnetic susceptivity.

Sample	IS wt% After pyrolysis	B_s , emu/g	B_s^{IS} emu/g	B_r, emu/g	H_c , Oersted	B_r/B_s
S0012	-	0.027	-	0.0045	10.57	0.166
S3012	33.5	12.14	36.24	0.047	3.974	0.0038
S4012	43.9	11.62	26.47	0.05	16.19	0.0043
S4010	43.9	10.5	23.92	0.051	7.873	0.0048
S5012	54.05	9.485	17.55	0.12	11.4	0.0126
S6012	63.8	17.02	26.68	0.063	8.81	0.0037

The Bs values indicate that Fe_3Si and Fe_5Si_3 are the predominant magnetic phases at higher temperature. However their values are found to be lower than would have been expected for Fe-Si powder. The reasons may be due to the mechanical constraint imposed on the Fe-Si particles by the SiOC matrix that restricts domain rotation or to the interfaces between the particles and the matrix that pin the magnetization and therefore resist the rotation and motion of the magnetic domain[14]. Generally, a pore in a magnetic material affects the permeability via the decrease in magnetization per unit

volume and moreover via the increase in the demagnetising field. The two above reasons, act together to lower the magnetization of the ceramic composite.

The variation in the coercive force can be attributed to the variation of the iron silicides multidomain structure, where the B_r/B_s increased to 0.0126 for the heat-treated S50 sample at 1200˚C. When the IS wt.% increases in the samples, the saturation magnetization decreases, probably due to imperfections in the crystal lattice.

Saturation magnetization (B_s) is a measure of the total amount of magnetic material in the sample. The coercivity, H_c, is a measure of magnetic stability. The ratio B_r/B_s is commonly used as indicators of domain states and, indirectly, grain size. High values of B_r/B_s (>0.5) indicate small (<0.1 μm or so) single-domain (SD) grains, and low values (<0.1) are characteristic of large (>15-20 μm) multidomain (MD) grains. Magnetic properties depend on the microsopic and macroscopic structure (crystal grain structure, grain boundaries). The microstructure of the solid controls the wanted or unwanted movement of magnetic domain boundaries and therefore affects the possibility of magnetic (re-) ordering processes and the magnetizability. Since the measurement of the magnetization depends on the investigated amount of material one has to relate the magnetization to the mass or the volume.

In order to reveal the nature of the domain states existing in our system, we can summarise as follows the data related to compositional and thermal variation of the hysteresis parameters (Figure 3. **9**): 1) the hysteresis loops of all the compositions investigated are very narrow; 2) the shape of the loop does not change appreciably with temperature 1000 and 1200℃; 3) the remanence ratio B_r/B_s of all the compositions is less than 0.01 and does not vary with temperature, and 4) the coercivity is small and almost temperature independent but depends on the IS content.

All the above observations support the presence of multidomain (M-D) grains and hence we conclude that all the compositions investigated by us contain M-D grains in predominance.

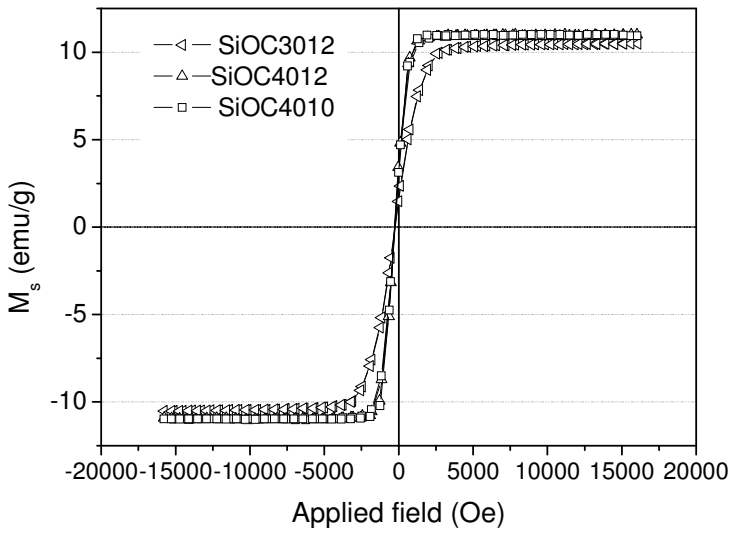

Figure 3. 9- Magnetization curves, upto 16.000 Oe.

There is just a tangible effect on the morphology and the shrinkage when we added 60% IS to the poly-siloxane preceramic polymer yielding the SiOC ceramic phase.

In Figure 3.7 Scanning Electron Microscope images of SiOC foam samples are reported. All the samples in the figure were pyrolyzed at 1200°C in nitrogen, containing different amounts of iron silicide powders (30, 40 and 60 wt%).

It can be noted that IS particles can be observed to be present on the cell walls and inside the struts. As it can be observed in Figure 3.7b IS particles present smaller size compare to the as received powders. This size reduction can be related to the fact that during pyrolysis at 1200°C the IS particles melt, thus resulting in new .Fe_3Si particles uniformily dispersed inside the matrix. The foam morphology was affected by the presence of magnetic particles, resulting in samples with a much less regular porosity with increasing amount of iron silicide filler, due to the change in the rheological behaviour of the preceramic polymer (increased viscosity in the warm-pressing forming stage). However, well defined cell-walls and struts could still be observed in the S6012 sample, in spite of the high IS powder content (see Figure 3. 10c).

Figure 3. 10- SEM pictures of: a) IS as received powders, b) S4012 (40 wt% IS, 1200℃, Nitrogen), c) S6012 (60 wt% IS, 1200℃, Nitrogen)

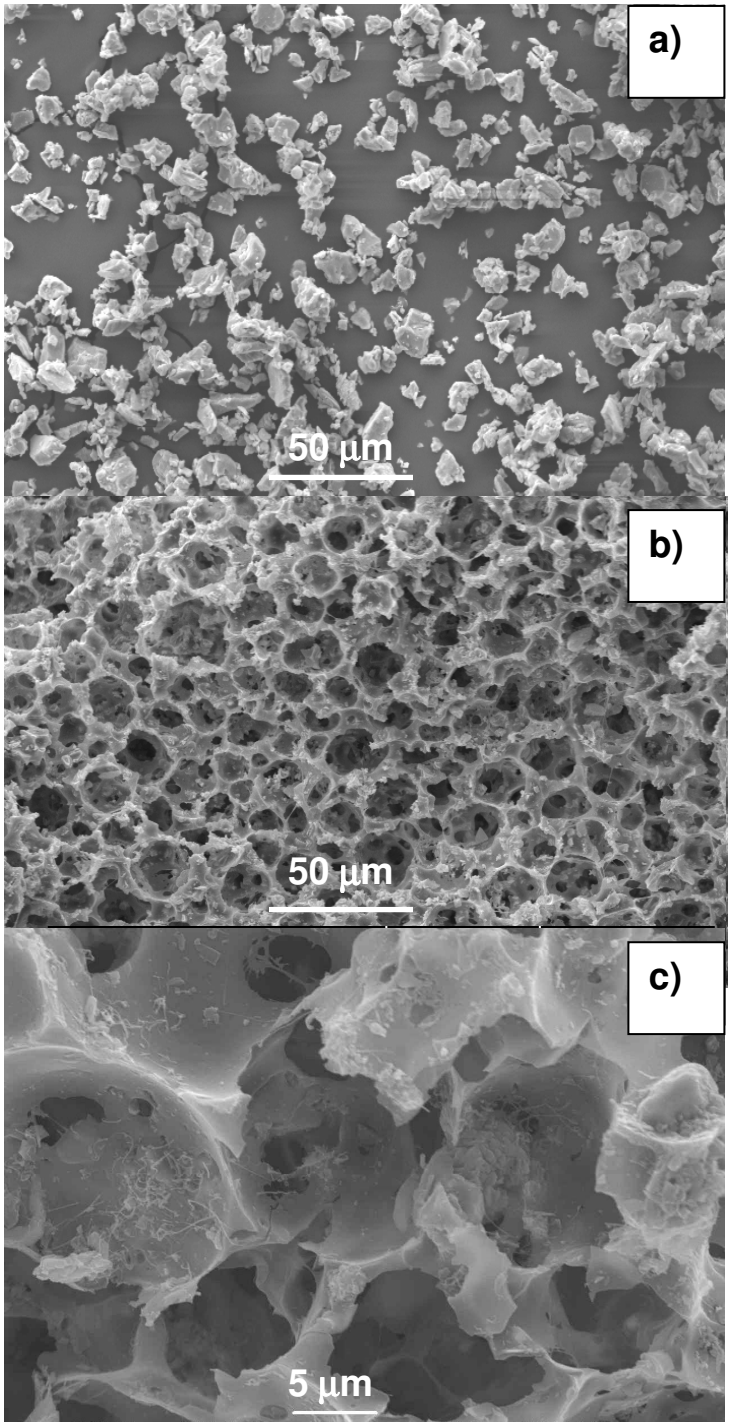

As expected, the relative density value increased with increasing amount of iron silicide, while the shrinkage decreased due to the presence of the inert filler. Compression strength values, see Table 3. 6, decreased with increasing IS wt%, certainly due to the disruption of the porous macrostructure as the associate increase of defects in the ceramic struts. The strength values, however, were quite high considering the fact that the samples have a porosity > 70 vol%.

Table 3. 6- Physico-Mechanical characterization data. S0012 refers to a SiOC MCF (no fillers), PMMA 25 μm pyrolyzed at 1200°C

Sample	ρ ± 0.01 (g/cm^3)	ΔV % (shrinkage)	σ± 0.3 (MPa)
S3012	0.37	42.2	2.2
S4012	0.39	41.52	3.1
S5012	0.42	41.02	1.8
S6012	0.45	39.55	1.3
S0012	0.26	64.4	10

In Figure 3. 11 a picture of a magnetic SiOC foam after pyrolysis is reported.

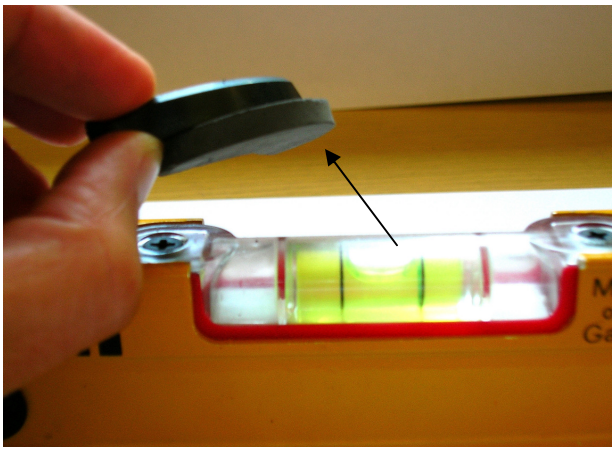

Figure 3. 11- Picture of a SiOC magnetic foam attached to a magnet

3.2.3 Conclusions

Ceramic foams possessing magnetic functionalization were produced from a preceramic polymer and iron silicide filler.

Iron silicide powders during pyrolysis were subjected to phase transformation and melting, this leading to a final iron silicide composition of cubic Fe_3Si of smaller size compared to the one of the a.r. powders.

Microstructural characterization by means of Mossbauer and XRD indicated that no significant reaction occurred between the SiOC matrix and the iron silicide filler. With increasing iron silicide content, the magnetic response was proportionally increased. The magnetic parameters such as H_c and B_r/B_s revealed the presence of a multi

domain grain structure, thus affecting the magnetic response of the composite material.

The foam morphology became more inhomogeneous and the compression strength decreased, increasing the iron silicide amount in the starting mixture.

This procedure allowed to prepare soft ferromagnetic SiOC microcellular foams, possessing a reasonable compression strength (1.3-3.1 MPa) and a saturation magnetization in the range 9.5-17 emu/g, depending on the amount of fillers introduced.

3.3 Magnetic SiOC microfoams by deposition of Iron and Cobalt Nanoparticles

3.3.1 Functionalized porous SiOC ceramics from pre-ceramic polymers

SiOC microcellular ceramic foams fabricated as reported in Chapter 2 possess an interconnected porosity and a homogeneous morphology. Moreover, they are an ideal substrate for the deposition of sensing / functional coatings. They possess a very high geometric surface (much larger than any flat substrate can offer on a unit weight basis), due to the very small size of the cells (in the range 5 to 40 µm) and the porosity is completely open / interconnected.

The main goal of this project is the synthesis of PDCs with magnetic properties by infiltration of those porous materials with metal carbonyl compounds solutions and subsequent thermal decomposition of these compounds. The advantage of using as precursors carbonyl compounds instead of nano-sized metal particles is the easier handling, solubility in organic solvents and lower sensitivity against air and moisture.

Polymer-derived SiOC micro foams with uniform cell size were used as starting materials. The synthesis of the micro foams follows the same procedure as reported in §2.2.

After mixing and warm pressing of the polysiloxane /PMMA microbeads composition, the sacrificial fillers were burned out from the green body in air at 300 °C. Subsequent pyrolysis in Argon at 1100 °C led to amorphous SiOC foams with a cell size of 10 µm.

The magnetisation of the as synthesised foams was carried out by infiltration in vacuum of the foams with THF solutions of iron and cobalt carbonyl compounds

followed by a heat treatment in argon or a argon / hydrogen mixture up to 800 °C. Figure 3. 12 shows the flow-chart diagram of the infiltration and Figure 3. 13 the structures of the used carbonyl compounds.

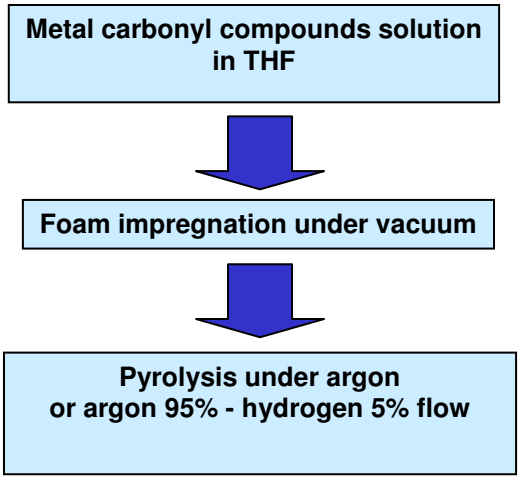

Figure 3. 12-Flow-chart of the foam infiltration

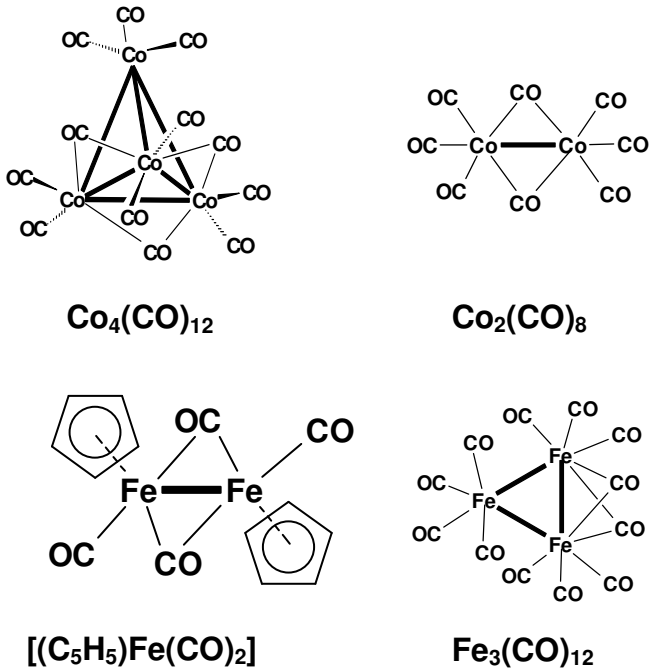

Figure 3. 13- Fe and Co carbonyl compounds used

The SEM images presented in Figure 3. 14 show the coated SiOC foams after heat treatment. No changes in the morphology of the foams in comparison with the uncoated materials were observable. Small particles were formed on the surface of the foam cells. The presence of iron and cobalt on the surface was checked with EDX. The results of the XRD measurements assign, the formation of Fe (BCC) and Co (FCC) respectively. The carbonyl compounds are decomposed through cleavage of

the CO groups and nano-sized metal particles are formed. No other crystalline phases are observed by XRD measurements. This result is evidence of the remaining amorphous state of the polymer-derived SiOC foam during the heat treatment.

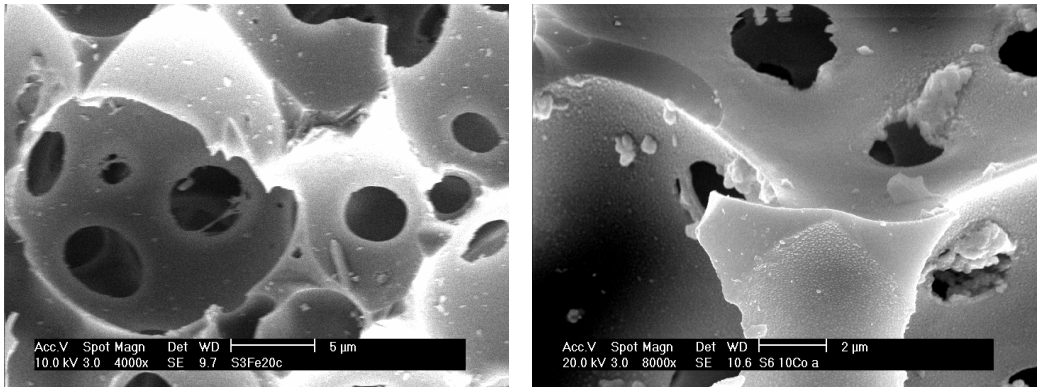

Figure 3. 14-SEM pictures of the metal carbonyl infiltrated micro-foams (left: iron, right: cobalt).

Magnetic measurements carried out on the iron and cobalt containing samples detect a soft magnetic behaviour of booth samples. The characteristic hysteresis curves of the Fe and Co containing samples are presented in Figure 3.12 and the results of the magnetic and XRD measurements are combined in Table 3.7. The reason for the small amount of metal on the foam surface is the poor solubility of the metal precursors.

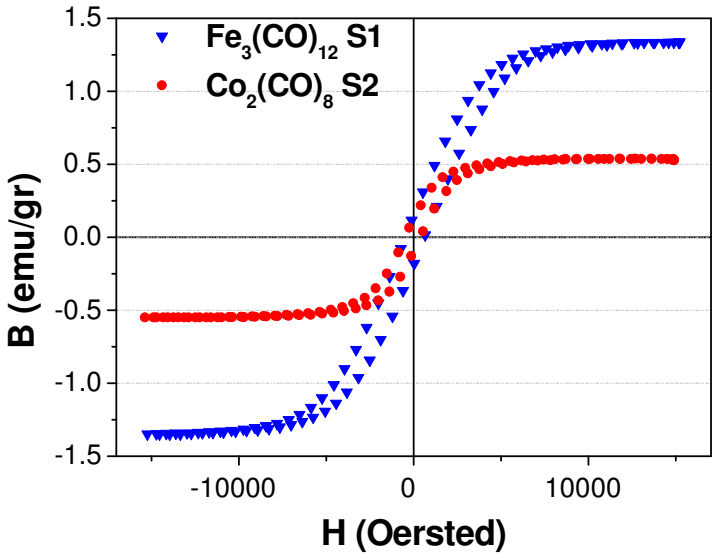

Figure 3. 15-Hysteresis cycles from VSM measurements at room temperature of SiOC foams infiltrated by $Fe_3(CO)_{12}$ and $Co_2(CO)_8$ solution.

Table 3. 7-Overview of magnetic measurements and XRD results.

Sample	S1	S2
Sol	$Fe_3(CO)_{12}$	$Co_2(CO)_8$
Concentration	2 g in 20 ml	1 g in 10 ml
Metal (wt.%)	1.12	8.74
μ	3.1	5.5
Bs (emu/gr)	1.36	0.55
Hc (Oe)	6.1	180.5
Br (emu/gr)	0.007	0.055
Br/Bs	0.005	0.100
XRD results	Fe (BCC)	Co (FCC)

To increase the metal amount for further experiments, precursors with a higher solubility as well as $[(C_5H_5)Fe(CO)_2]_2$ and $Co_4(CO)_{12}$ were used.To investigate the influence of the temperature on the particle size, the SiOC foams were infiltrated by metal carbonyl solutions with constant concentration (1g of carbonyl compound on 20 ml of dried THF) and heat treated at 400, 600 and 800 °C in argon with a holding time of 30 min. The results of the SEM investigations, presented in Figure 3.14, show a strong temperature dependence on the particle size. In the case of the iron containing samples, the particle size rises from 10-70 nm at 300 °C to 140-200 nm at 800 °C.
The nucleation and growth of the nanoparticles can be related to a migration mechanism on the SiOC surface, since no strong bonds between the Iron particles and the SiOC matrix are expected.

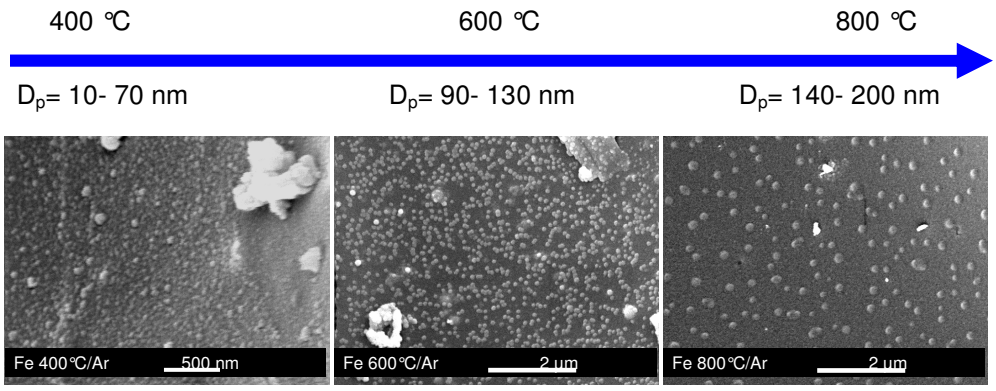

Figure 3. 16-SEM pictures of SiOC-micro-foam (PMMA 50 µm) impregnated with $[(C_5H_5)Fe(CO)_2]_2$ solution and annealed under Argon flow at 400 °C (left), 600 °C (middle), 800 °C (right).

The cobalt containing samples show in principle the same behaviour (Figure 3.15). However, because of the form and the agglomeration of particles the accuracy of the

measurements is not as high as the iron containing samples. The size of the cobalt particles ranges from 80 – 250 nm at 300 °C to more than 350nm at 700°C.

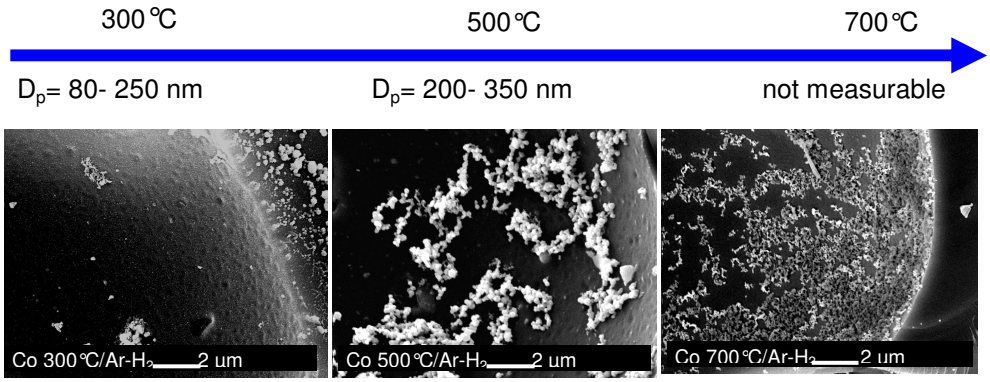

Figure 3. 17-SEM pictures of SiOC-micro-foam (PMMA 50 µm) impregnated with $Co_4(CO)_{12}$ solution and annealed under Argon 95 % -H_2 5 % flow at 300 °C (left), 500 °C (middle), 700 °C (right).

In conclusion, the infiltration of PDCs micro-foams is a successful method to produce magnetic functionalized ceramics. Thermal decomposition of metal carbonyl compounds leads to the formation of iron or cobalt containing nano-particles on the foams' cell-walls. The high geometrical surface of the ceramic foams offers a stable support to the particles. The particles size can be controlled by heat treatment conditions during thermal decomposition of the metal carbonyl compounds.

Acknowledgements: the work reported in §3.2 was supported by MIUR, programma di collaborazione bilaterale Italia-Egitto, Project n. 13 *"Preparation and Properties of Nanocomposites SiON- and SiOC- Based Ceramic Materials".*
The work reported in §3.3 was presented as a poster with the title "*Magnetic Material by the Infiltration of Polymer-Derived Ceramic Foams"* at the CIMTEC, 4-9 June 2006, Acireale (CT), Italy and was supported by MIUR Ateneo Italo-Tedesco in the VIGONI Program and DAAD, German Science Foundation.
L.B. wish to thank Prof. G. Prncipi, Dr. P.Palade and Dr. S. Sartori, Università di Padova- Italy, Dr. R. Hauser, Darmstadt University, Darmstadt-Germany and Dr. Adel Francis, CMRDI, Cairo-Egypt.
Moreover L.B. wish to thank Dr. M. Baricco, Politecnico di Torino, Italy for XRD investigations and helpful discussions.

References

[1] Wynne K.J, Rice, Ann R.W.. *Rev. Mater. Sci*. 14, 297 (1984).
[2] Bill J, Aldinger F, *Adv. Mater*,7, 775 (1995)
[3] Greil P, *Adv Eng Mater*, 2, 339 (2000)
[4] Greil P., *J. Am. Ceram. Soc.* 78, 835 (1995).
[5] Seyferth D., Bryson N., Workman D.P., Sobon C.A., *J. Am. Ceram.Soc.* 74, 2687 (1991).
[6] Suttor D., Kleebe H.-J., Ziegler G., *J. Am. Ceram. Soc*. 80, 2541 (1997).
[7] Riedel R, Nature, 355, 714 (1992)
[8] Wei Q, Pippel E, Woltersdorf J, Scheffler M, Greil P, *Mater. Chem. and Phys.*, 73, 281-89 (2002)
[9] Haluschka C., "Examination of the Electrical Properties of Multinary Ceramics in the Systems Si-C-N and Si-B-C-N"; Ph.D. Thesis. Technical University of Darmstadt, Darmstadt, Germany, 1997.
[10] Cordelair J.and Greil P, *J. Eur. Ceram. Soc.*, 20, 1947 (2000).
[11] Monthioux M.and Delverdier O, *J. Eur. Ceram. Soc.*, 16, 721 (1996).
[12] Cordelair J., "Electrical Properties of Polymer/Filler Derived Ceramics"; Ph.D. Thesis. University of Erlangen-Nuernberg, Erlangen, Germany, 1999.
[13] Cordelair J, Geil P, *J Am Ceram Soc*, 84, 2256-59 (2001)
[14] Saha A, Shah S and Raj R, *J. Mater. Res*., 18, 2549-51 (2003)
[15] Hauser R, Francis A, Riedel R, "Synthesis and Properties of Polymer Derived Metal/SiCN Ceramic Micro- and Nano- Composites", Proceedings of the E-MRS Spring Meeting, Strasbourg, France, 24-28 May (2004)
[16] Colombo P, Gambaryan-Roisman T, Scheffler M, Buhler P and Greil P, *J Am Ceram Soc*, 84, 2265-68 (2001)
[17] Colombo, P., Bernardo, E. and Biasetto, L., *J. Am. Cer. Soc*., 87, 152-54 (2004).
[18] Wertheim, G. K., Jaccarino, V., Wernick, J.H.et al. *Phys. Lett.*, 89, (1965)
[19] Jaccarino, V., Wertheim, G. K., Wernick, J. H. et al. *Phys. Rev*. 160, 476 (1967)
[20] Watanabe, H., Yamamoto, H. and Ito, K., *J. Phys. Soc. Jpn.*, 18, 995 (1963)
[21] Varga, L. K., Mazaleyrat, F., Kovac, J. and Greneche, J. M, *J. Phys.: Condens. Matter* 14, 1985-2000 (2002).
[22] Starke, U., Schardt, J., Weiss, W., Meier, W. et al, *Europhys. Lett.*, 56, 822-828 (2001)
[23] Raghavan V, *Phase Diagram of Ternary Iron Alloys*, ASM International (1987)

Chapter 4

High Specific Surface Area SiOC microcellular foams

4.1 Hierarchical Porosity Components by Infiltration of a Ceramic Foam

4.1.1 Introduction

Porous materials containing interconnected cavities in the nanometer to millimeter range (e.g. zeolites, honeycombs, foams) hold a significant position in industry owing to their widespread use in several industrial processes and household products. Applications include catalysis, filtration (of liquids or gases), extraction, separation, sorption, thermal management, scaffolds for biological applications and low-specific gravity components for structural applications. In all these cases, the synthesis procedure of a porous material must allow for the control of both pore dimension and pore size distribution, which generally are required to be narrowly centered on a specific value. Advanced applications may require pores that are interconnected and thus open to the external environment, to allow for a diffusing specie to flow through the porous material, or isolated and not accessible from the outside, e.g. in low dielectric constant materials in microelectronics. Graded or oriented porosity is also sometimes required for specialized applications[1]. According to IUPAC classification[2,3],porous solids fall into three categories according to their pore dimension (d): micro- ($d < 2$ nm), meso- (2 nm < d < 50 nm) and macroporous ($d > 50$ nm).

The synthesis of mesoporous materials is generally based on a templated self-assembly strategy, where the polycondensation of molecular inorganic nano-building blocks is guided by the presence of supramolecular structure-directing agents formed by the self-assembly of amphiphilic species. Mesoporous silica with large (~10 nm) ordered interconnected pores can be obtained reproducibly in the form of powders, films and monoliths using self-assembling amphiphilic block copolymers as the templating species. Pore size and shape can be precisely adjusted by selecting a copolymer with suitable architecture and composition[4]. Due to the typically large specific surface area, which can be as much as 700 m^2g^{-1}, mesoporous silicas have applications as molecular sieves, while the large pores allow catalyzing reactions involving macromolecules, thus overcoming the restrains imposed by the small pore dimension in zeolites[5]. Moreover, the possibility to functionalize the pore surface with

species bearing specific chemical units opens the way to more functional applications, for example as sensors or selective filters for removing pollutants[6].

A special category of macroporous solids is that of cellular materials (foams, honeycombs, fiber mats). In particular, ceramic foams, because of their morphology, possess an unique combination of different properties, such as low density, thermal conductivity, dielectric constant, thermal mass and high geometric surface area, thermal shock resistance, permeability (if open cells), specific strength, dimensional stability, hardness / wear resistance, resistance to chemical corrosion, fire resistance, tortuosity of flow paths, which permits them to satisfy specific functional purposes of significant industrial interest[7].

A material with hierarchical bimodal pore size distribution in the meso and macro range (2-50 nm and >50 nm respectively) offers interesting properties compared to a monomodal porosity material. Of particular interest is the case of a macroporous monolith serving as a support within which a material having smaller pores is coated. Ideally, the macroporous framework ensures the chemical and mechanical stability, as well as good mass transport properties due to interconnections between the macropores, while the coating with smaller pores provides the functionality for a given application, for example it may show enhanced catalytic properties or selectively bind an analyte.

One-pot strategies for the synthesis of materials with this type of hierarchical porosity have been devised: for instance, Danumah et al. obtained silica powders showing high surface area with a bimodal meso- and macro- porosity by a dual templating approach[8], while the synthesis of trimodal (micro-meso-macro) silica using an ionic liquid, KLE block copolymer[1] and polystyrene (PS) spheres as the templating agents was reported[9]. Another interesting approach is to infiltrate a template made of colloidal PS spheres, with a gel containing the silica source and a block copolymer: thus, a macroporous materials with mesoporous walls is obtained after calcination[10]. Moreover, if suitable precursors are used in the infiltration step, other chemical compositions of the walls can be obtained, such as TiO_2, ZrO_2 and aluminophosphates[11]. However, the use of one-pot or infiltration synthesis strategies leads to the presence of porosity in the whole macroporous framework, which may impair the mechanical strength of the final material. Moreover, catalyitic applications involve chemical reactions at the very surface of the macropores, thus the presence of active sites inside the framework walls is not beneficial.

Ceramic foams are optimal candidate as substrates for the development of porous bodies with hierarchical (micro-, meso- and macro-) porosity. Their very large

[1] KLE is a [poly(ethylene-co-butylene)-block-poly(ethylene oxide)] block copolymer, with the chemical formula $[H(CH_2CH_2)_{0.67}(CH_2(CH)CH_2CH_3)_{0.33}]_{100}(OCH_2CH_2)_{86}$-OH.

geometric surface area (of the order of a few $m \cdot cm^{-3}$ for micro-cellular foams) provides a wide region for the deposition of coatings of suitable materials possessing micro-/meso-porosity, the complete interconnection of the porosity provides easy access to the precursors for obtaining such coatings and their chemical inertness allows processing and use in harsh environments. Furthermore, in comparison to the conventional packed beds used as catalyst support in chemical engineering applications, these cellular macro-porous materials afford a lower pressure drop, a higher external mass transfer rate, greater turbulence and increased convective heat transfer.[12,13,14,15]

In the recent past, we pursued the development of ceramic bodies possessing hierarchical porosity either by a controlled thermal treatment and/or the addition of suitable fillers[16] or by depositing zeolites onto the cell walls of SiOC microcellular foams.[17] The approach we followed in this work was to prepare a silicon oxycarbide (SiOC) macroporous (microcellular) foam, which was shown to have good mechanical properties and high chemical durability,[18] and deposit a mesoporous SiO_2 coating on the cell walls by impregnation.

4.1.2 Experimental

Synthesis

An ordered mesoporous SiO_2 coating was deposited on the walls of a macroporous SiOC foam obtained from preceramic precursors. The interconnection among the mesopores provides microporosity to the material. The SiOC foam was synthesized from preceramic polymers using PMMA spheres (macro)pore formers, while the mesoporous silica coating was obtained by a templated self-assembly strategy using tetraethoxysilane as the silicon source and block copolymer Pluronic F127 as the structure-directing agent. SiOC ceramic foams were prepare das reported in 2.2, by mean of 185 μm PMMA. Cylindrical samples of 30 mm diameter and 4 mm thickness (after pyrolysis) were prepared. SiOC samples were then cut in smaller pieces by a cutting tool. The mesoporous silica precursor solution contained tetraethyl orthosilicate (TEOS) as the silica source and block copolymer Pluronic F127 (EO106-PO70-EO106, EO=CH2CH2O, PO=CH(CH3)CH2O) as the structure-directing agent. A starting solution was prepared by mixing 4 g TEOS and 2.5 g EtOH, and successively adding 0.355 g of a 0.768 M HCl solution. This solution was stirred for 45 minutes in order to pre-hydrolize the silane units, and added to a solution containing 12 gr EtOH, 1.3 gr Pluronic F127 and a 0.057 M HCl solution. This was stirred for further 15 minutes before impregnation. SiOC foams were immersed into the silica solution and withdrawn after 1 minute, excess solution was then removed from the samples with

absorbing paper. The impregnated samples were dried in air at ambient temperature for 20 days. A thermal treatment was performed on the impregnated samples in order to remove the surfactant from the mesopores and promote further condensation of the silica framework. Calcination was carried out in air at 350°C for 1 hour (heating rate = 1°C·min^{-1}).

Characterization

Scanning Electron Microscopy (JEOL, Japan) was performed in order to detect the morphology of the foams and the coating homogeneity. Samples were cut with a razor blade and the fracture surface was investigated.

For imaging and characterizing the mesopores formed on the coated inner surfaces of the ceramic foams high resolution transmission electron microscopy (TEM) was used. The investigations were performed in a Philips CM20 FEG microscope, operated at 200 keV.

Specimens for TEM were prepared by cutting thin slices (100 µm) with some foam/coating interfaces of interest oriented perpendicular to the sample surface (cross section technique).

To stabilize the porous samples for cutting and grinding and to enable the ion thinning process the foam was infiltrated with epoxy resin before starting the preparation procedure. Residues of the epoxy can be seen in most of the TEM images. Thereafter the slices were

mounted on copper rings, followed by grinding dimpling and final Ar-ion thinning down to electron transparency using a segmental method in the PIPS (precision ion polishing system, Gatan 691).

Small angle X-ray scattering (SAXS) measurements were performed at the Austrian beamline at ELETTRA synchrotron in Trieste, Italy, using an incident energy of 8 keV. Slices of approximately 3 mm thickness were cut from the samples and inserted in the beam path (transmission mode). SAXS patterns were acquired with a CCD detector (Photonic Science, UK). Calibration was performed with a silver behenate powder standard (d = 58.38 Å) in a capillary glass. Prior to analysis, each image was corrected for background intensity and spatial distortion due to the finite curvature of the CCD detector.

Specific Surface Area (SSA) and Pore Size Distribution (PSD) of the coated and uncoated samples were obtained from nitrogen adsorption-desorption measurements at 77 K using an ASAP 2020 (Micromeritics, Norcross, GA) instrument. The samples were previously degassed at 120°C for at least 8 h before analysis. The nitrogen adsorption data were collected in the relative pressure range (P/P0) of 10-5< P/P0< 1. To obtain an accurate characterization of the microporous region, sufficient data points in the low pressures regime are needed, which requires the addition of constant

small nitrogen volumes. Hence, successive nitrogen doses of 1 cm^3g^{-1} were added until P/P0 = 0.01 was reached.

Subsequently, further nitrogen was added and the gas volumes required to obtain a fixed set of relative pressures, up to a value of 1.00, were measured. SSA was determined from a BET (Brunauer, Emmet, and Teller) analysis[18] in the P/P0 range of 0.05–0.2 with a correlation coefficient of 0.999, using a molecular cross-sectional area for N2 of 0.162 nm2 and a minimum of five data points. The pore size distributions were obtained from the desorption branch of the isotherm through the BJH (Barret, Joyner, and Halenda) analysis[19],which takes into account the KJS equation for the calculation of the layer thickness and Faas correction[20]. The micropores size distribution was calculated using the Horvath-Kawazoe analysis for cylindrical pore geometry[21].

4.1.3 Results and Discussion

SiOC ceramic foams belong to the wider class of materials named cellular solids. The properties of this specific class of materials are deeply influenced by the morphology (porosity percentage, cell size, cell size distribution, degree of interconnectivity) and by the relative density of the foam, defined as the ratio between the apparent density (given by the ratio between the weight and the size of the sample) of the foam and that of the solid from which it is made[7]. By means of the processing route described above it is possible to produce SiOC microcellular ceramics possessing a high degree of interconnectivity and a wide range of cell sizes, just by varying the size and amount of the PMMA sacrificial microbeads[22].

Since the goal of the present work was to verify the feasibility of the proposed method, foams with the largest pores size (PMMA 185 μm) were chosen in order to favor the impregnation step, as smaller macropores could possibly lead to a more difficult uptake of the mesoporous silica precursor solution. On the other hand, mechanical strength scales with the inverse of the pore size; therefore the choice of a PMMA size of 185 μm is a trade-off between the two issues.

Structural characterization of the mesoporous silica coating

Scanning Electron Microscopy investigations revealed the presence of a coating on the foam surface (Figure 4. *1*a and b). Few cracks were detected at the surface curvatures, where stresses concentrate preferentially during drying. The coating appears to be delaminated in some areas; however this could likely have been induced by sample cutting before SEM analysis. The film thickness ranges from ≈ 1 μm to ≈ 5 μm in correspondence of the struts (Figure 4. *1*b).

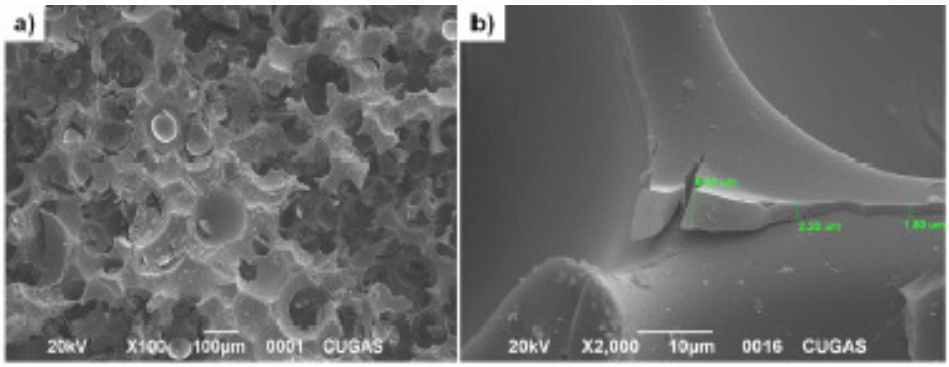

Figure 4. 1- a) Low magnification image of the S185 sample after calcination in air at 350°C.b) Detail of the film thickness on the strut surface.

From TEM images, the coating appears to be ordered throughout the whole thickness, with less ordered regions located close to the coating-foam interface (Figure 4. 2). In few cases, poor order is observed at the coating-foam interface. There is a good agreement between thickness values measured by TEM (thickness ≈700 nm, Figure 4. 2) and SEM images (µm range, Figure 4. 1), even though the latter gives more reliable information revealing that the film is somewhat inhomogeneus in thickness depending on the macropore region considered.

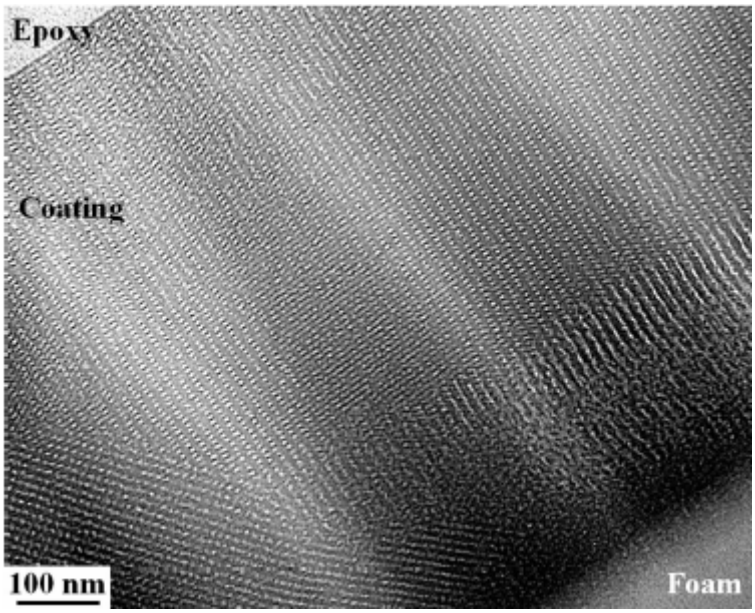

Figure 4. 2- Cross sectional TEM image showing a regulare pore arrangment in the coating (middle part) on the foam (lower right).

TEM images of mesoporous coatings in samples treated at 350°C, taken at different projection planes, show 4-fold (Figure 4. 3 a) and 6-fold (Figure 4. 3 b) symmetry axes: this is compatible with a cubic lattice, based on the assumption that the symmetry of the mesostructure is constant in the whole material.

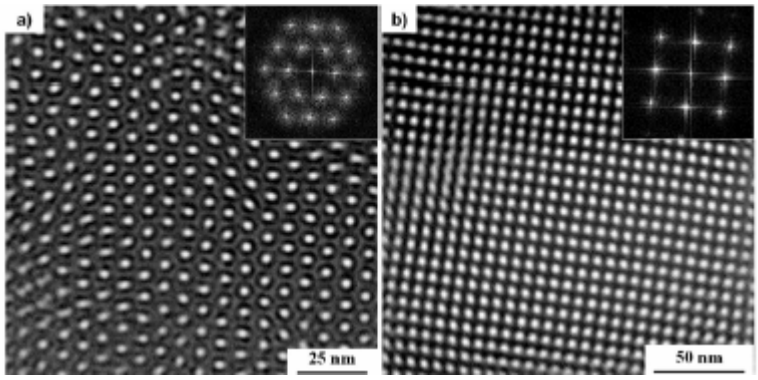

Figure 4. 3- a) and b): TEM images of selected pore arrangements in the coating (inset: calculated FFT diffraction pattern demonstrating the well arranged pores with individual lattice orientations).

As TEM gives information about order on a strictly local scale (a few hundred of nanometers), we performed also two-dimensional small angle X-ray scattering (SAXS) measurements in order to obtain structural information averaged on a larger volume of sample. SAXS is a technique which collects the X-rays elastically scattered at a very low angle (typically 0.1 - 5°) by a sample containing features in the nanometer range (e.g. biologic macromolecules, ordered materials). The probed region extends on the volume of matter interested by the interaction with the impinging X-ray beam. In our case, SAXS was performed in transmission mode, i.e. a slice of the sample was placed in the beam path at a given distance from the CCD detector. The lateral dimension of the X-ray beam was ≈ 3 mm^2 so that the volume probed by SAXS was $\approx$ 10 mm^3. SAXS diffraction patterns of foams impregnated with the mesoporous silica solution display a ring, both for thermally treated and untreated samples (Figure 4. 4 a). As a matter of fact, these SAXS patterns can be considered to be the intersection of the Ewald sphere with the reciprocal lattice, which describes the periodic modulations in the electronic density of matter (here, the periodicity of the silica mesoporous coating) in the reciprocal space. Since the structure is made of ordered domains lying on curved polyoriented surfaces, the reciprocal lattice appears as a set of concentrical spheres, and its intersection with the Ewald sphere yields a set of concentrical rings. On the other hand, SAXS patterns of foams that were not impregnated do not show any feature, which is a further confirmation that the ring is related to the ordered mesoporous silica coating.

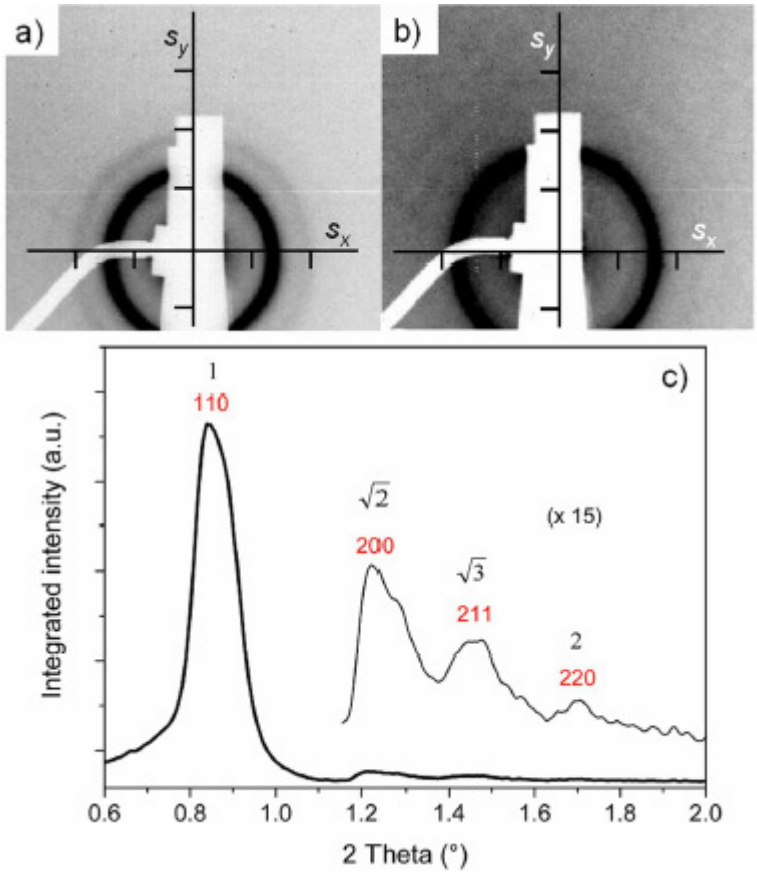

Figure 4. 4- Diffraction patterns of impregnated samples: with no thermal treatment (a) and after calcination (b); the scattering vector axes sx and sy are reported, with the scale bar corresponding to 0.007 Å-1. The radial integration of the diffraction pattern in (a) is reported in (c), where each peak shows its Im3m Miller index and its d-spacing relative to the main peak position.

The radial integration of diffraction patterns, starting from the beam center towards the outer region, yields an intensity vs. 2-theta curve (Figure 4. 4 b) showing the presence of three additional peaks that are not immediately visible in the patterns, related to the presence of the ordered mesostructure. The d-spacings relative to these three smaller peaks can be related to the d-spacing of the most intense, with ratios 2 , 3 and 2. In thermally treated samples the d-spacings are smaller than in untreated samples, but the proportions remain constant.

This is consistent with a BCC unit cell with *Im*3*m* space group having no preferential orientation with respect to the laboratory frame ("powder-like"). Simulations were performed with CMPR program[23] in order to reproduce diffraction data, selectively choosing space groups according to those most often observed in mesoporous silica[24]. These simulations were found to be consistent with SAXS data only when choosing an *Im*3*m* unit cell with lattice parameter a = 18 nm in untreated samples, and a = 14 nm in treated samples. The peaks were thus assigned to the 110, 200, 211, 220 reflections.

Based on these results, representative images relative to different projection planes were selected and the BCC cell parameter was calculated from their FFT by from simple geometric considerations, assuming that planes merge due to the depth of field of the electron microscopy (see Figure 4. 3). Due to the merging of planes, the {111} and {100} projection planes (Figure 4. 3 a and b, respectively) show the pores at the cube vertices as well as the pores located in the centre of the unit cell. Therefore, the {100} interpore distance represents the diagonal of a face of the cubic unit cell, and must be multiplied by 2 in order to get the cell parameter *a*, while the {111} interpore distance must be multiplied by 2 / 3 . This calculation yields $a = (13 \pm 1)$ nm, which is in agreement with the present SAXS data, as well as with previously reported data relative to mesoporous silica membranes prepared by a similar procedure.26[25] The average diameter of mesopores was estimated with a line profile analysis of representative TEM images, as the average FWHM of the intensity distribution along a line passing through the centers of the pores, obtaining a value of (4.5 ± 0.8) nm.

Nitrogen adsorption

The nitrogen adsorption-desorption isotherms for coated samples are reported in Figure 4. 5 a. The uncoated SiOC foam possesses a SSA of 3.4 m^2g^{-1}, and pores having size <100 nm were not detected. Concerning the coated samples, the isotherm follows the typical behavior of mesoporous materials. The fast rise at low relative pressure values reflects the presence of micropores (< 2 nm). The hysteresis loop shape is typical for interconnected pores that give rise to a 3D network[26].

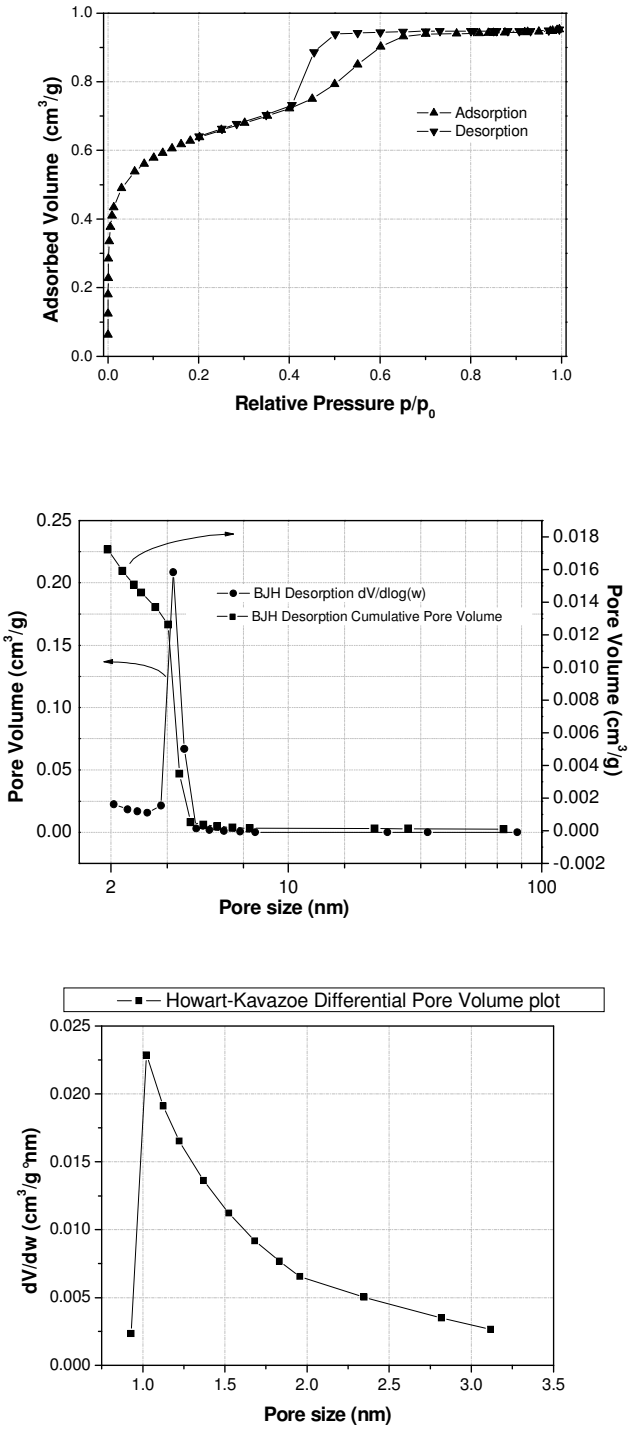

Figure 4. 5- a) Adsorption-desorption isotherm for coated samples. Sample was measured after calcination in air at 350°C. b) BJH Desorption cumulative Pore Volume and BJH desorption dV / d(logD). c) H-K micropore cumulative pore size.

BJH desorption cumulative pore volume as a function of the pore size is reported in Figure 4. 5 b. The pore size distribution is quite narrow and the main pore diameter measures (3.2± 0.3) nm, in reasonable agreement with the data obtained using Image

Analysis on TEM micrographs. The underestimation of pore size compared to the values measured from TEM investigations is a typical inconvenience of the method, even after the introduction of the Faas correction for layer thickness[26].

Micropores volume and size were calculated using the Horwat-Kawazoe method, for cylindrical pore shape, resulting in a median pores size of 1.3 nm (see Table 4. 1).

Table 4. 1- Overview of the results obtained from the analysis of the nitrogen adsorptiondesorption isotherm and TEM investigations, performed on samples after calcination.

SSA (m^2g^{-1})	$V_{micropore}$ (cm^3g^{-1})	$d_{micropore}$ (nm)	$V_{mesopore}$ (cm^3g^{-1})	$d_{mesopore}$ (nm)	$d_{mesoporeTEM}$ (nm)
60.2	0.01	1.1	0.026	3.2 ± 0.3	4.5 ± 0.8

The Specific Surface Area (SSA) measured by the BET method gave a value of (60.2 ±0.3) m^2g^{-1}. However, considering that the effective weight of the mesoporous material is the weight of the mesoporous silica film coating the macroporous SiOC foam, the SSA value was recalculated considering the weight difference of the sample before and after impregnation and calcination. This gave a SSA value of (564.9 ±2.5) m^2g^{-1}, which is two orders of magnitude higher than that of SiOC foams with the same macropore size (3.4 m^2g^{-1}), and is comparable to the typical SSA values of mesoporous silica powders found in the literature[5].

4.1.4 Conclusions

We produced a ceramic component possessing hierarchical meso- and macro-porosity by depositing a mesoporous silica coating on the surface of an open-cell SiOC foam. The walls of the macropore substrate are covered uniformly by the mesoporous silica layer having a thickness ranging from <1 _m to ~5 _m. The mesostructure has a high degree of order almost everywhere in the coating, and it can be described by a body-centered cubic cell with *Im*3*m* space group with no preferential orientation with respect to the macropore curved surface. The mesopores exhibit a narrow size distribution, and appear to be interconnected through micropores, giving rise to an interconnected 3D porous network in the coating. The specific surface area of the component increased of one order of magnitude due to the presence of the mesoporosity in the coating. This material with a hierarchical porosity can be of use in applications where high specific surface area as well as high permeability are required, e.g. catalysis and sorption, or as a scaffold for the immobilization of biological species.

4.2 Development of porosity by HF etching on SiOC ceramic foams

Ternary PDCs systems, such as SiCN and SiOC, have attracted considerable attention in the last years especially because of their unusual properties e.g. the absence of steady-state creep, the presence of viscoelasticity at very high temperatures[27,28,29], oxidation resistance[30] and outstanding chemical durability even in harsh enviroments[31].

The reasons of these unique properties lay on their specific structure at the nano-scale, however a comprehension of such micro-nanostructure has not been fully reached yet. Even though X-ray diffraction pattern from these materials is usuallly featureless, they are not strictly amorphous and short-range structural order have been detected as a form of nanodomains.

The presence of free carbon seems to be the first responsible of PDCs' properties. The carbon present in the preceramic precursor used for the PDCs synthesis normally segregates during the redistribution reactions occurring in the high temperature processing of the gel or polymer. As a matter of fact, upon pyrolysis the polymer releases predominatly hydrogen (instead of hydrocarbons), leaving behind excess carbon in the ceramic. The presence and role of the free carbon phase in this type of materials has been recently studied by Saha et al.[32]

In the reported work, SiOC samples with different free carbon content, have been studied by means of nuclear magnetic resonance (NMR), small angle X Ray scattering (SAXS), transmission electron microscopy (TEM) and Fourier Transform Infrared Spectrometry (FTIR). The model consists on a cellular nanostructure of silica domains surrounded by domain walls. The domain walls consist of graphene layers and mixed-bond silica tetrahedra of SiO_mC_{4-m}, where m= 1, 2, or 3 (Figure 4. 6).

This model is consistent with the creep and crystallization behavior of SiOC: the graphene network would prevent long-term creep, as the flow in the silica domains will gradually shed load on to the graphene network, which can deform only by elastic deformation. Thus long-term, steday-state creep is not admissable. At the same time, this structure would exhibit viscoelastic behavior as, upon unloading, the elastic strain stored in the graphene network would release back the applied strain as the silica domains are restored to their original shape.

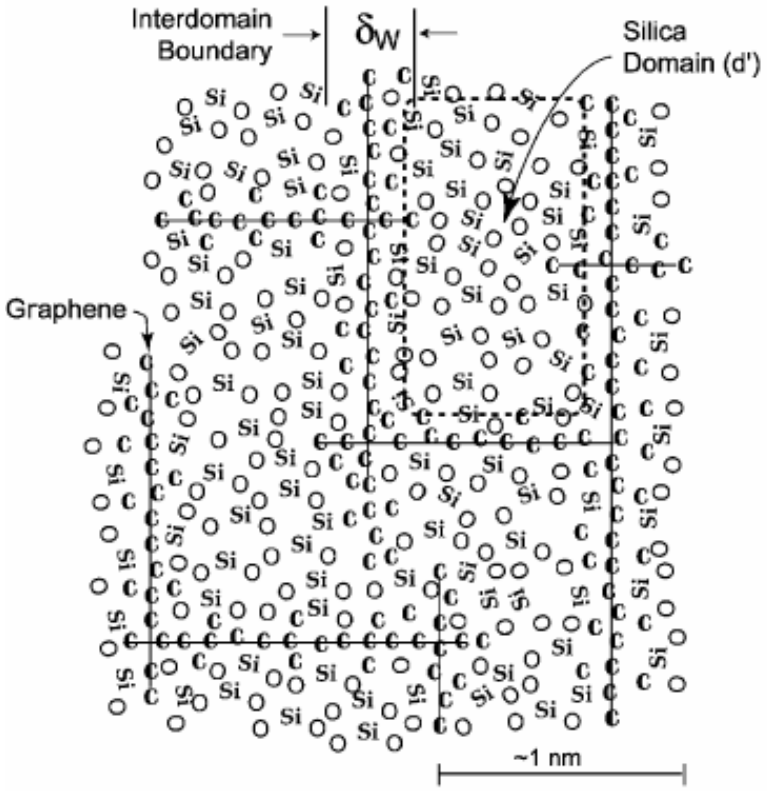

Figure 4. 6- A concept of the molecular make-up of the nanodomains. Note that the interdomain boundary consists of graphene layers with mixed Si–C–O bonds forming the interface with the silica domains.

concerning the crystallization behavior, the materials are thermally stable up to temperatures as high as 1450°C. Above this temperature, SiO_2 can crystallize to cristoballite and the carbothermal reduction reaction yields SiC crystals. In the model proposed in [32], the finite domain size of silica may inhibit crystallization if the domain size is comparable to the critical size for the nucleation of the crystalline phase. Moreover, it is also important to consider the energy of the SiOxCy mixed bonds which forms the interface between the carbon layers and the clusters of silica

tetrahedra. It seems that this interface has a particularly low interfacial energy that inhibits the heterogeneous nucleation of cristoballite.

Further evidence in the nanodomain model of Saha et al. has been reported by Pena-Alonso *et al*.[33]

Hydrofluoric acid etching of SiOC ceramics with moderate carbon content removes silica without removing any carbon. Furthermore, the pores left behind the etching process, are in the same range as the size of the nanodomains described in the above model. By this chemical route, the nanodomains size can be detected and compared to the model of Saha *et al*. Morover, it was found that the nanodomain size can represent a key factor on the etchability of SiOC systems. If they are too small, then the inward diffusional access of the etchant and the outward diffusion of the etching

products can become too slow. The studies show that the SiO_2 nanodomains have an average size of 4-6 nm and are not usually larger than 10 nm.
In any of the studied samples, nitrogen adsorption-desorption measurements reveled a SSA ranging between 150 and 615 m^2/g after etching and the presence of a large amount of micro and mesopores with a broad size distribuition.
These findings point out the possibility to develop micro and mesoporosity on SiOC structures by the etching technique. The present work deals with the HF etching of SiOC microcellular foams, in order to develop components with a hierarchical porosity.

4.2.1 Experimental

SiOC microcellular ceramic foams were prepared by the synthetic route reported in 2.2., by mean of PMMA microbeads with average size 50 μm, sample labelled SiOC50.
The sample labelled as MTES, was obtain from pyrolysis of a sol-gel derived hybrid as reported in [33] and the results have been used for comparison.
The etching of the SiOC materials (bulk and ground SiOC50 foams and MTES) was performed using an HF solution (20 vol% in H_2O). Samples were placed in a polypropylene container with the hydrofluoric acid (HF) solution. The weight ratio between the SiOC samples and the HF solution was kept constant to 1:50. The solution was stirred at room temperature for 9 h and then filtered and rinsed off with distilled water to remove any residual HF. The etched powders were heated up to 110°C to remove the residual products.
After pyrolysis further annealing was performed on SiOC50 samples in order to verify the effect of the heat treatment on the etching. Thus, those samples undergone the following treatments:
i) Oxidation in air at 650°C for 2 hours (so called -***ox*** labelled samples)
ii) Pyrolysis at 1300°C under nitrogen flow in an alumina tube furnace (***-pyr*** labelled samples)
iii) Pyrolysis at 1300°C in a HIP (Hot Isostatic Press) under nitrogen atmosphere. (***-HIP*** labelled samples), following the cycle reported in Figure 4.7.

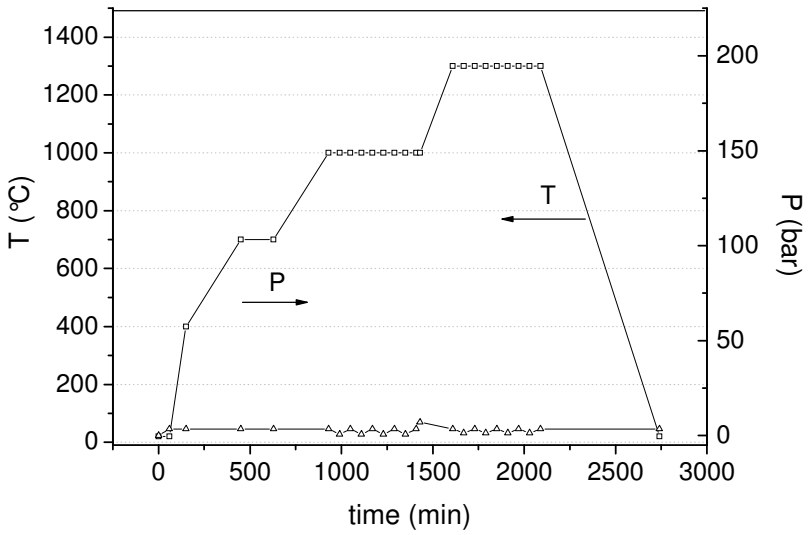

Figure 4. 7- Hot Isostatic Pressing cycle under nitrogen atmosphere.

As can be observed in Figure 4.7 three main heating steps were followed:

1. T_1= 700ºC, dwelling time 3h, P=3.5 bar
2. T_2= 1000ºC, where pressure was varied every hour from 3.5 to 0.7 bar, for eight hours total,
3. T_3= 1300ºC, where pressure was varied from 3.5 to 1.4 bar every hour for eight hours total.

All samples were analysed by nitrogen adsorption-desorption. The isotherms were collected at 77 K using an ASAP 2010 (Micromeritics) instrument on previously degassed specimens at 200ºC for at least 4 hours. SSA was determined from a BET (Brunauer, Emmet and Teller)[34] analysis in the P/P_0 range of 0.05 - 0.30 and the pore size distributions (PSDs) were obtained from the adsorption branch of the isotherm through the BJH (Barret, Joyner and Halenda) analysis[35]. The mesopore volume represents the cumulative volume of the pores with radii ranging from 1.8 to 100 nm and the average pore diameter has been obtained from 4V/A, where, V is the volume and A is the surface area of the mesopores.

4.2.2 Results and Discussion

The etching efficiency of the foams is certainly related to the cells size and the degree of interconnectivity of the foam. Thus, the increase of the degree of interconnectivity and the size of the openings between adjacent cells would produce a better renewal of old solution with fresh one.

In order to test the etching efficiency on bulk and powdered samples, the SiOC foam was also griound (SiOC50-p) and then etched. As reported in table, no significant variation in the SSA value was detected respect the etched bulk sample, this confirming the good pores interconnectivity of the foam. Since no appreciable differences between SiOC50-b and SiOC50-p were detected, all etching tests were performed on SiOC50-b samples.

Figure 4. 8 a) shows the isotherms curve obtained for the etched foam SiOC50-p. The observed type II isotherm accounts for adsorption by macroporous adsorbents with strong adsorbate-adsorbent interaction according to the IUPAC classification[36]. The isotherm present a slight steep increase at low values of relative pressure which indicates the presence of some micropores and a hysteresis loop characteristic of mesoporous samples. The pore size distribution (PSD) in the mesopore range (2-300 nm) shows the increasing presence of pores from 10 nm of diameter to lower size pores Figure 4. 8 b). Figure 4. 8 is rapresentative of the behaviour of all the samples tested.

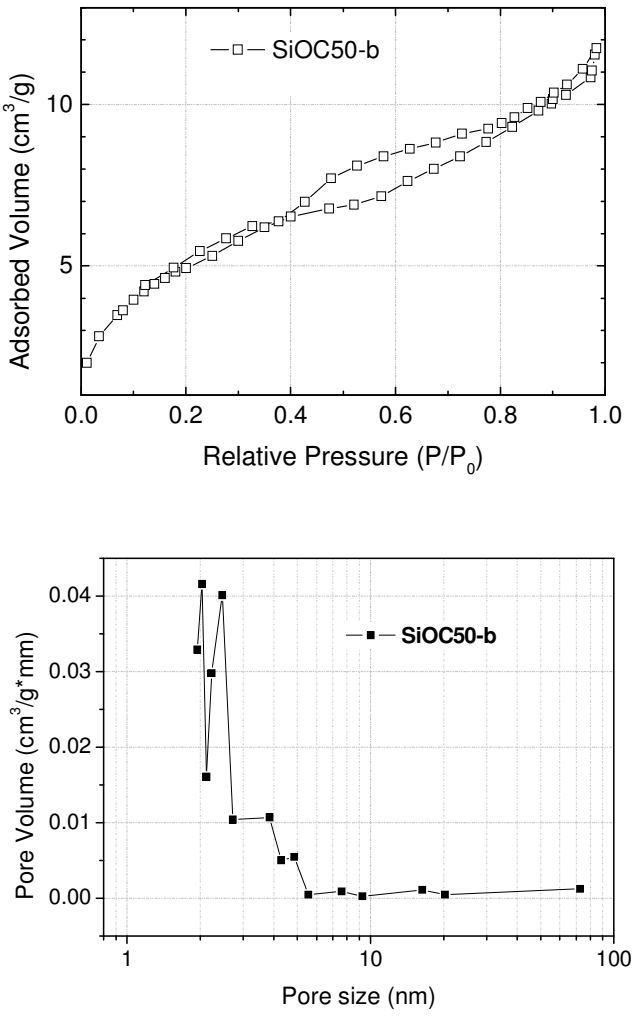

Figure 4. 8- Isotherm plot and Pore Size Distribuition, for sample SiOC50-b

The efficiency of the etching was studied by analysing the SSA of samples etched at increasing times from 9h to 24h. According to Zank et al. [37], which showed that no further etching is observed in SiOC specimens after 5 hours of attack, the SiOC foams displayed also similar values of SSA for the different etching times studied, thus showing that etching is complete after 9 hours of stirring

In an attempt to improve the etching ability of the foams, further thermal treatments (ox, pyr, HIP) were performed on the SiOC50 foam as described in the experimental part. The bases of the applied thermal treatments comes from the thought that the smaller amount of SSAs and pore volumes developed in the present foams with respect to already published data on SiOC powder specimens obtained from full dense bulk glasses [31,33] can be due to different facts:

a) The different micro/nano-structure of the foams respects the bulk glasses.
b) The different arrangement of the free C present in a more protective barrier for the etching.

As an experimental fact, it has been noticed the lower wettability of the foams, respect to the bulk oxycarbide material, MTES, which can make difficult the penetration of the HF solution into the porous structure. This smaller wettability could be attributed to the higher presence of carbon and oxycarbide phase at the surface of the materials, which protects the specimens against the HF attack.

The air thermal treatment (process ***-ox***) was performed to remove part of the carbon by direct oxidation of the samples; on the other hand the higher temperature pyrolysis processes ***-pyr***, and higher temperature and pressure, ***-HIP*** focus on the development of phase separation of the oxycarbide structure.

Table 4. 2- SSA and porosity results overview.

Sample	Further Treatment	SSA (m^2/g)	V_{micro} (cm^3/g)	V_{meso} (cm^3/g)	$d_{averag\ meso}$ (nm)
SiOC50-b	-	30.3	0.017	0.026	4.5
SiOC50-p	-	37.0	0.007	0.031	3.8
SiOC50-b-ox	650°C air	46.0	0.017	0.048	5.3
SiOC50-b-pyr	1300°C N_2	64.7	0.023	0.090	7.7
SiOC50-b-HIP	HIP-1300°C N_2	56.5	0.028	0.031	4.0
MTES		194.4	0.107	0.067	3.3

The oxidation of the SiOC50 foam (SiOC50-b-ox specimen) produce a slight increase in the SSA values mainly due to an increase of the mesoporosity respect to the non oxidized sample (see Table 4.1) . However, a further increase of those values is found when the samples are pyrolyzed at higher temperature previously to the oxidation. Thus, SiOC-b-pyr possesses 64.7 m^2/g and some increase of both meso and micropores.

On the other hand, the HIP treated foam do not develop a pronounced SSA value. In this case, we postulate that, even if the phase separation can be effective in foamed specimens after the HIP treatment, the high chemical durability of the foam material can be due to the protective effect of the PMMA residual carbon on the surface, which can block the entering of the solution inside the nanostructure.

As reported in [31] and [33], free carbon deriving from the pyrolysis of a ceramic presursor can exhibit a double role on the etching efficiency: first, the free-carbon phase provides an interphase between SiO_2 nanocrystallites and, thereby can inhibit their growth; this condition has an effect on leaching, because it limits any decomposition of the SiOC phase to form the more soluble SiO_2. Moreover, as

reported in [33] the nanodomain size is a critical parameter for etching efficinecy. Second, free carbon is insoluble in HF solutions; therefore, it will act as a chemical barrier, hindering the attack or diffusion of F^- ions at and within the surface.

Thirdly, C-containing surfaces have a lower wettability by water than oxide surfaces.

MK-derived SiOC ceramics exhibit a carbon content after pyrolysis[38] comparable to the MTES derived SiOCs, however, the SiOC studied foams do not develop so high SSA values as the MTES material.; as far as free carbon inhibits the etching efficiency, for the above reported reasons. We are induced to think that the free carbon deriving from burn-out PMMA may interact with the matrix surface during pyrolysis, thus increasing the amount of free carbon on the SiOC surface, carbon which can act as physical barrier to HF etching.

One more reason can be related to the polymer architecture, which can increase the number of nanodomains and decrease their dimension, so leading to the etching unefficiency, however a more detailed study is necessary to prove this hypothesis. As a preliminary study of this hypothesis some trials of etching several MK samples pyrolyzed without the foaming PMMA agent have been performed. The SSA analyses on them displayed values comparable to the results reported in Table 4.2 on the SiOC50 foam samples. Thus, the assumption of having a smaller nanodomain size in SiOCs from MK derived materials that inhibits the etching must be considered as the main reason for the behaviorof the material.

Acknowledgments: the work reported in § 4.1 was submitted on December 2006 and accepted on February 2007, to the Journal of American Ceramic Society, with the title “Hierarchical Porosity Components by infiltration of a ceramic foam”
The work reported on § 4.2 was supported by Marco Polo Program, Università di Bologna, Italy.
L.B. wish to thank S. Costacurta, Università di Sassari-Italy, E. Pippel and Prof. J. Woltersdorf, Max Plank Institute, Germany, Dr. S. Carturan, LNL, INFN, Legnaro-Italy, Dr. R. DeLaPena, Università di Trento-Italy and Prof. G.D. Sorarù, Università di Trento-Italy.

References

[1] Schüth F.,. Sing K. S. W, and Weitkamp J., *Handbook of porous solids*, p. 3191. Wiley-VCH Verlag GmbH, Weinheim, Germany, 2002
[2] J. Haber, *Pure and Appl. Chem.*, **63**, 1227-1246 (1991).
[3] J. Roquerol, D. Avnir, C. W. Fairbridge, D. H. Everett, J. H. Haynes, N. Pernicone, J. D. F. Ramsay, K. S. W. Sing, and K. K. Unger, *Pure and Appl. Chem.*, **66**, 1739-1758 (1994).
[4] G. J. de A. A. Soler-Illia; E. L. Crepaldi, D. Grosso, and C. Sanchez, *Curr. Opinion Colloid Interf. Sci.*, **8**, 109-126 (2003).
[5] G. J. de A. A. Soler-Illia, C. Sanchez, B. Lebeau, and J. Patarin, *Chem. Rev.*, **102**, 4093-4138 (2002).
[6] L. Nicole, C. Boissière, D. Grosso, P. Hesemann, J. Moreau, and C. Sanchez, *Chem. Commun.*, 2312-2313 (2004).
[7] M. F. Ashby, "Cellular solids - Scaling of properties"; pp. 3-17 in *Cellular Ceramics: Structure, Manufacturing, Properties and Applications*. Edited by M. Scheffler and P. Colombo. Wiley-VCH Verlag GmbH: Weinheim, Germany, 2004.
[8] C. Danumah, S. Vaudreuil, L. Bonneviot, M. Bousmina, S. Giasson, and S. Kaliaguine, *Microp. Mesop. Materials*, **44-45**, 241-247 (2001).
[9] D. Kuang, T. Brezesinski, and B. Smarsly, *J. Am. Chem. Soc.*, **126**, 10534-10535 (2004).
[10] T. Sen, G. J. T. Tiddy, J. L. Casci, and M. T. Anderson, *Angew. Chem. Int. Ed. Engl.*, **42**, 4649-4653 (2003).
[11] B. T. Holland, C. F. Blanford, T. Do, and A. Stein, *Chem. Mater.*, **11**, 795-805 (1999).
[12] J. T. Richardson, Y. Peng, and D. Remue, *Appl. Catal. A: General*, **204**, 19-32 (2000).
[13] J. T. Richardson, M. Garrait, and J.-K. Hung, *Appl. Catal. A: General*, **266**, 235-244 (2004).
[14] B. Schimmoeller, H. Schulz, S. E. Pratsinis, A. Bareiss, A. Reitzmann, and B. Kraushaar-Czarnetzki, *J. Catal.*, **243**, 82-92 (2006).
[15] W. M. Carty and P. W. Lednor, *Curr. Opinion Solid State Mater. Sci*, **1**, 88-95 (1996).
[16] H. M. Schmidt, D. Koch, G. Grathwohl, and P. Colombo, *J. Am. Cer. Soc.*, **84**, 2252-2255 (2001).
[17] A. Zampieri, P. Colombo, G. T. P. Mabande, T. Selvam, W. Schwieger, and F. Scheffler, *Adv. Mater.*, **16**, 819-823 (2004).
[18] S. J. Gregg and K. S. W. Sing, *Adsorption, surface area and porosity*, pp. 285-286. Academic Press, London, 1982.
[19] E. P. Barret, L. G. Joyner, and P. H. Halenda, *J. Am. Chem. Soc.*, **53**, 373-380 (1951)
[20] M. Kruk, M. Jaroniec M., and A. Sayari, *J. Phys. Chem. B*, **101**, 583-589 (1997).
[21] G. Hovarth and K. Kawazoe, *J. Chem. Eng. Jpn.*, **16**, 470-475 (1983).
[22] P. Colombo and E. Bernardo, *Comp. Sci. Tech.*, **63**, 2353-2359 (2003).
[23] http://www.ncnr.nist.gov/programs/crystallography/software/cmpr/ (accessed December 2006)
[24] B. W. Eggiman, M. P. Tate, and H. W. Hillhouse, *J. Phys. Chem. B*, **18**, 723-730 (2006).
[25] L. Malfatti, T. Kidchob, P. Falcaro, S. Costacurta, M. Piccinini, M. C. Guidi, A. Marcelli, A. Corrias, M. F. Casula, H. Amenitsch, P. Innocenzi, submitted to *Microp. Mesop. Mat.*
[26] S. Lowell, J. E. Shields, M. A. Thomas, and M. Thommes, *Characterization of porous solids and powders: surface area, pore size and density*, p. 349. Kluwer Academic Publishers, 2004.
[27] Rouxel T, Sorarù G D, and Vicens J, , *J Am Ceram Soc*. 84, 1052-58 (2001)
[28] Rouxel T, massouras G, and Sorarù G D, *J Sol-gel Sci Tech* 14, 87-94 (1999)
[29] Scarmi A, Sorarù G D, and Raj R, *J. Non-Cryst Solids*, 351, 2238-43 (2005)
[30] Chollon G, Aldacourrou B, and Capes l, *J Mater Sci*, 33, 901 (1998)
[31] Sorarù G D, Modena S, Guadagnino E, and Colombo P, *J Am Ceram Soc*, 85, 1529-36 (2002)
[32] Saha A, Raj R, and Williamson D L, *J Am Ceram Soc*, 89, 2188-95 (2006)
[33] Pena-Alonso R, Sorarù GD, Raj R, *J Am Ceram Soc*, 89, 2473-80 (2006)
[34] S. J. Gregg and K. S. W. Sing, "Adsorption, Surface Area and Porosity" pp. 285-286, Academic Press, London, 1982.

[35] E. P. Barret, L. G. Joyner and P. H. Halenda, "The determination of pore volume and area distributions in porous substances. I. Computations from nitrogen isotherms", *J. Am Chem. Soc.,* 53**,** 373-380 (1951)
[36] IUPAC Recommendations, Pure Appl. Chem. 1994, 66, 1739
[37] A. M. Wilson, G. Zank, K. Eguch, W. Xing, B. Yates, J. R. Dahn, Chem. Mater. 9 (1997) 2139-2144
[38] Harshe R, Balan C, and Riedel R, *J. Europ. Ceram. Soc.,* 24, 3471-82 (2004)

Appendix 1

Properties of Cellular Ceramics

A.1.1 Mechanical Properties

The dependence of mechanical properties, such as Young's modulus, bending (or flexural) strength and compressive (or crushing) strength, on the porosity and pore morphology of cellular ceramics is of vital importance for structural applications. In particular, a property/porosity relationship is important for predicting the values of the considered property, thus allowing for the tailoring of the cellular structure for fulfilling specific mechanical requirements. Several models have been proposed in the last 10 years[1,2], but there are still uncertainties, mainly in the description of the mechanical behaviour of closed-cell foams[3]. It was found, for example, that the use of a single model, or even the numerical fitting coefficients in the equation describing the same model, is not so satisfactory when employed over a large range of porosity values. In fact, variations in the porosity content may be accompanied by changes in the pore structure (and size)[3,4], so that data extrapolation and affordable predictions may be extremely difficult.

The two main models for the interpretation of mechanical properties of cellular ceramics are the models of Gibson and Ashby[1], referred to here as GA models, and the Minimum Solid Area (MSA) models, widely discussed by Rice[2,3]. As a rough approximation, we can say that the first models focus on the solid phase comprising the cellular structure, while the second one focuses on the gas phase (i.e. the porosity and its distribution). The GA models are based on the idealization of the cellular structure as composed of a number of hollow polyhedrons (cells), variously stacked and interconnected. These cells are in turn composed of mono-dimensional elements (cell *edges*) and bi-dimensional elements (cell *faces*) supposed to represent the entirety of the sample (i.e. all the sample possesses the same cell size). The balance between closed and open-porosity in the particular cell is fitted by a parameter (ϕ), which expresses the fraction of material present in the cell edges (ϕ thus represents the specific contribution, or "weight", of mono-dimensional elements to the particular property). The MSA models are based on the assumption that the mechanical behaviour of the particular cellular object ideally corresponds to that of a cellular material with a structure comprising the dense uniform packing of identical spherical (or cylindrical) cells. The fitting of experimental data is obtained by referring to a

particular way of packing or stacking of individual cells (and taking into account their shape).

The main and very appreciable feature of GA models is their general approach: the mathematical equations describing different properties (even those different from the mechanical characteristics) are very similar, and there is uniformity in the description of cellular bodies made from different classes of materials (ceramics, polymers or metals). For example, there are different GA models depending on the ductile or fragile failure; the same model of fragile failure may be applied to cellular fragile polymers, glasses or other ceramics.

The concepts of *struts* and *lattice* are the fundamental basis of the GA models. A cell is defined by a number of mono-dimensional elements (struts), such as the edges of polyhedrons, and the connection between different polyhedrons determines a periodic tri-dimensional network (lattice). On the micrometric scale, the geometry of cellular materials resembles that of the frame structures (scaffolds) in civil engineering. However, it is the connection among the struts that constitutes the fundamental difference: while in many civil engineering structures (e.g. metal bridges) the overall structure is determined by the replication of triangular structures, in common cellular materials the number of edges for each face is higher than three, with the result of a generally much lower stiffness and a dramatically different collapse behaviour. This condition is due the so-called "Maxwell's Stability Criterion"[5]: three points joined in a triangular structure cannot be mutually moved, except in the case of stretching the connecting struts. As an analogy, the same stretching of struts is necessary for four points at the corners of a tetrahedron. In stretch-dominated structures (planar, i.e. triangles, or tri-dimensional, like tetrahedrons) the mutual movement of cell corners occurs only after severe loading. Most cellular solids, based on non-triangular (or not fully triangular) structures are bending-dominated: the bending of some struts easily causes the mutual movement of cell corners.

As mentioned above, the GA models focus on the solid phase, and a quantification of the solid phase within the cellular material is given by the relative density ρ_r, i.e. the ratio between the "apparent" density of the cellular material ρ (the "geometrical density", i.e the ratio between the mass and the volume of a cellular sample) and the density of the material in the hypothesis of no porosity ρ_S (the so called "true density", or "skeleton density", which can be easily measured by pycnometry on finely powdered samples): $\rho_r = \rho/\rho_S$.

In lattice-structured materials, i.e. structures based on mono-dimensional elements or open-celled foams, there is a direct correlation between the cell size, L, and the thickness of the cell *edges*, t_e, as follows[1]:

$$\rho_r = \left(\frac{\rho}{\rho_S}\right) = C_1\left(\frac{t_e}{L}\right)^2 \quad (1)$$

In the hypothesis of a material with a cellular structure composed of closed polyhedrons, i.e. closed-celled foams, another correlation must be considered[1], based on the face thickness t_f:

$$\rho_r = \left(\frac{\rho}{\rho_S}\right) = C_2\left(\frac{t_f}{L}\right) \quad (2)$$

The constants C_1 and C_2 are numerical factors depending on the particular cell shape. This description is satisfactory in many situations, especially in the case of low relative density values, but more general expressions may be found by considering the distribution of the solid phase between edges and faces, summarized, as above mentioned, by a ϕ parameter. ϕ is the volume fraction of the solid contained in the cell edges; $(1-\phi)$ obviously expresses the fraction of solid in the faces. The ϕ parameter depends on the thickness of both edges and faces, and on morphological characteristics of the cellular structure, such as the average number of edges per face in a single cell, n, and the number of faces that meet at an edge, Z_f, as follows[1]:

$$\phi = \frac{t_e^{\,2}}{t_e^{\,2} + \frac{Z_f}{n} t_f L} \quad (3)$$

If f is the number of faces in a single cell, there are two correlations between ϕ and the relative density, as follows[1]:

$$\frac{t_f}{L} = \frac{2C_3}{f}(1-\phi)\rho_r$$
$$\frac{t_e}{L} = \left(\frac{2Z_f}{n}\frac{C_3}{f}\phi\rho_r\right)^{1/2} \quad (4)$$

For most foams $Z_f = 3$, $n \approx 5$, $f \approx 14$ (each cell being idealized as a polyhedron with 14 faces, known as “tetrakaidecahedron”) and $C_3 \approx 10$, so that the above reported equations may become simpler[1]:

$$\frac{t_f}{L} = 1.4(1-\phi)\rho_r$$
$$\frac{t_e}{L} = 0.93(\phi\rho_r)^{1/2} \quad (5)$$

Although straightforward in definition, the actual measurement of the ϕ parameter is rather difficult in real bodies; image analysis is undoubtedly useful, but averaging the data for a great number of cells, especially in the case of non-uniform and homogeneous foams, may be very time-consuming. Moreover, for some foam morphologies, the separation between edge and cell wall can be somewhat arbitrary (see Figure 1b).

The parameter ϕ and the relative density constitute the reference for all GA models concerning mechanical properties (i.e. elastic modulus, bending and compressive strength) and functional properties (i.e. thermal or electrical conductivity). The models are based on an open-celled morphology, and are focused simply on relative density; corrections for closed-celled foams are developed as a function of ϕ. Each property is described as "normalized", i.e. every property of the cellular material is referred to that of the solid material. The exponents in the normalized property/relative density come from dimensional analysis[3,6].

The elastic constants (Young's and shear moduli) of a cellular material are expressed normalized to the Young's modulus of the solid phase, E_S, as follows:

$$\frac{E}{E_S} \approx (\rho_r)^2$$
$$\frac{G}{E_S} \approx \frac{3}{8}(\rho_r)^2 \qquad (6)$$

The Poisson's ratio,ν, is predicted to be equal to 0.33, but there is limited information from experimental data, due to the inherent difficulty in measuring this particular property. The elastic contribution of the cell faces, bearing "membrane stresses", is almost linear with the relative density, so that additional parameters in the previous equation are needed. In general, the pressure of the gas phase entrapped in closed cells must be taken into account (variations in the cell volume, after a certain strain, are accompanied by variations of pressure of the fluid); however, for atmospheric pressure (0.1 MPa) and for cellular ceramics, the pressure contribution may be neglected. The elastic constants for bodies with closed cells are described by

$$\frac{E}{E_S} \approx \phi^2(\rho_r)^2 + (1-\phi)\rho_r$$
$$\frac{G}{E_S} \approx \frac{3}{8}\left\{\phi^2(\rho_r)^2 + (1-\phi)\rho_r\right\} \qquad (7)$$

As mentioned above, the cellular structures are "bending dominated". Upon loading, the struts are subjected to buckling, and severe bending moments arise. While in elastomeric foams there is an extensive buckling, i.e. a progressive curvature of cell

edges, due to the relevant deformability of the specific type of materials, as illustrated by Figure A1. 1, ceramic foams (with a linear elastic behaviour) undergo progressive rupture, corresponding to the successive fracturing of edges. This phenomenology is highlighted by the typical stress-strain curve (see Figure A1. 2): after a linear-elastic deformation, the structure continues to collapse at an almost constant stress (the increase of elastic stress with increasing strain is practically counterbalanced by the succession of fracture events at the cell edges), until the cells impinge and the stress rises steeply (the deformability of the "densified" foam resembles that of a powder compact, and the elastic stress is much increased upon progressive packing of fragments).

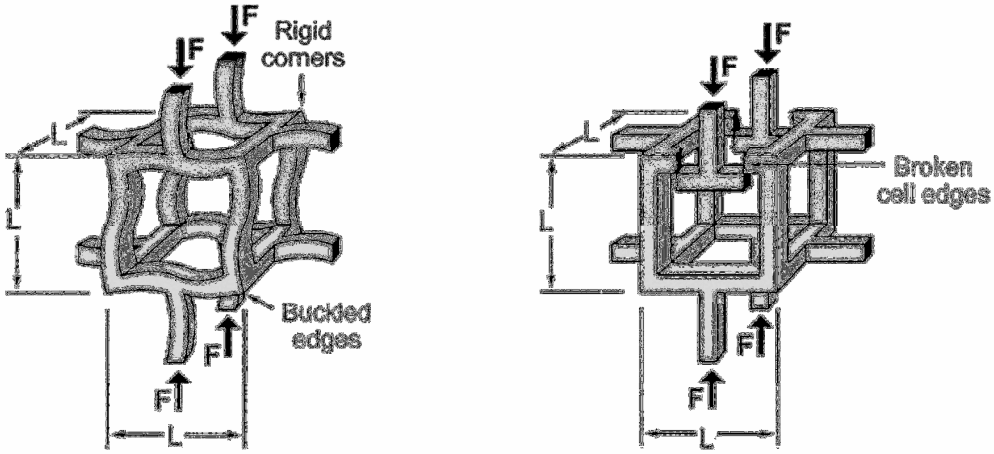

Figure A1. 1- Models of collapse for bending dominated cellular structures: left, elastomeric foam (extensive buckling); right, brittle foam (progressive fracturing of cell edges). From [5], with permission.

The onset of crushing, for open-celled foams, is correlated to the relative density[3] by

$$\frac{\sigma_{cr}}{\sigma_{fs}} \approx 0.2(\rho_r)^{3/2} \qquad (8)$$

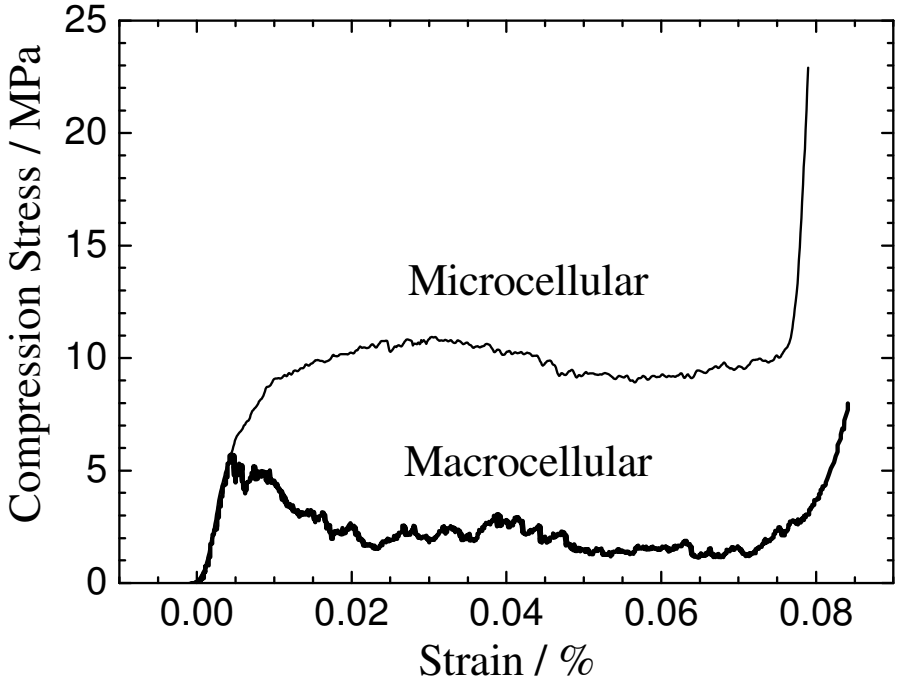

Figure A1. 2- Stress-strain curves for SiOC ceramic foams (macro-cellular - cell size ~460 µm; micro-cellular – cell size ~ 8 µm. Relative density = 0.21 for both samples).

where σ_{fs} is the flexural strength (modulus of rupture) of the solid phase. Also in this case, the contribution of cell faces (subjected to membrane stresses) in modifying the expression for closed-celled foams, is expressed by a linear term, as follows [3]:

$$\frac{\sigma_{cr}}{\sigma_{fs}} \approx 0.2(\phi\rho_r)^{3/2} + (1-\phi)\rho_r \qquad (9)$$

Brittle foams are subjected to a size effect: beyond differences in the distribution of solid phase between cell and faces (the ratios between t_e or t_f and L - and consequently the parameter ϕ - may not be constant when varying the same cell size, L), the strut strength increases with decreasing cell size. Colombo et al. showed[7,8] that SiOC microcellular foams collapse at much higher loads than macrocellular foams, with the same relative density, likely due to the reduction of the probability of finding critical cracks in micro-sized struts (see also Figure A1. 2). Gibson and Ashby[1] reported that, if the modulus of rupture of cell edges is described by a Weibull statistics, the ratio between the crushing strength of two different open-celled foams, with the same solid phase but with different average cell size and different density, depends on the Weibull modulus, m, as follows:

$$\frac{\sigma_{cr,1}}{\sigma_{cr,2}} = \left(\frac{L_2}{L_1}\right)^{\frac{3}{m}} \left(\frac{\rho_2}{\rho_1}\right)^{\frac{1}{m}-\frac{3}{2}} \qquad (10)$$

Moreover, Brezny and Green[9,10] calculated that the critical flaw size in open-cell ceramics is often between one or two cell sizes, thus confirming the improvement of

strength with the decrease of cell size; the same authors, however, reported that strut strength may decrease, in some cases, due to introduction of new flaw populations, so that the mechanical properties are primarily determined by considering the relative density.

The basic idea of underlying the MSA models is that of considering sections, normal to the applied stress (or thermal flux, electric current etc.), in which the solid area is minimized (as an example, for poorly sintered powders, the minimum solid area corresponds to a section comprising the thin necks between adjacent particles). The ratio between this MSA and the area of the sample in the same plane gives the relative MSA, to which each material property needs to be scaled. Many computer models, based on finite element analysis (FEM) may be regarded as extensions of MSA models[3].

Basic GA models are not properly MSA models. GA models are load-bearing models, based on the assemblage of mono- and bi-dimensional elements, neglecting the stress concentrations associated with the junctions of the elements[2], and the structural in-homogeneity in the case of closed cells, which are generally thinner in their central area (sometimes, for foams at an intermediate stage between perfectly closed cell foams and lattice-structured foams, the cell walls contain a hole at the centre)[3]. GA models were found to differ substantially from experimental data collected for several ceramic foams, such as glass[11] or SiOC foams[12,13]. Glass foams have been successfully modelled by the GA approach for Young's modulus, but some uncertainty has been reported for flexural strength, since the data were best fitted by assuming an anomalously low value (11 MPa) for un-foamed solid (the actual bending strength for glass is 5-10 times higher); a better fitting was instead found by using a MSA approach[3,11]. Colombo *et al.*[13] reported that for open-celled SiOC foams (produced from foamed preceramic polymers) the exponents for fitting flexural and bending strength were 2.3 and 3.6 (substantially different than expected) ; on the other side, for the same type of foams, Colombo and Hellmann[[14] found that Ashby's theory was respected for the fitting of elastic modulus data. Brezny and Green[6,9] found that the compressive data for ceramic foams were better fitted by exponents in the range 1.45-2.15, instead of 2 as indicated in the GA model.

A substantial disadvantage of MSA models, compared to GA models, is the fact that the equations are complex and the output of MSA modelling is generally a plot of relative MSA values, on a log scale, versus the porosity, P, on a linear scale[3]. The relative MSA values are the scaling factors for every property. For the evaluation of the Young's modulus of porous bodies, a general power law is frequently used:

$$\frac{E}{E_S} \approx (1-P)^n \qquad (11)$$

where P is the porosity volume fraction. If the exponent n is equal to 2, the equation clearly coincides with that from GA approach. Some authors[15,16,17] reported some porosity-dependent factors and consequent porosity-dependent functions f, so that $E/E_S=f\cdot(1-P)^n$; these functions resemble those for all composite materials[2]. Some models are based on exponential function, as follows:

$$\frac{E}{E_S} \approx e^{-bP} \tag{12}$$

where b represents the slope of initial approximately linear portions of semilog plots (E/E_S or relative MSA on a log scale and P on a linear scale), and depends on the particular packing or stacking of spherical or cylindrical pores, chosen to achieve the best fitting of the data.

The most recent models focus on an interesting refinement of the P factor employed in the previously reported equations[18]. For many porous materials, there is a "critical" porosity volume fraction, P_C, at which the value of the various properties go to zero. The quantification of this volume fraction depends on the pore shape: for example, for cylindrical pores in cubic stacking (as in honeycombs) $P_C\approx1$, while for pores defined from the stacking of solid spheres in cubic stacking, $P_C\approx0.45$, as illustrated by Figure A1. 3. If the normalized porosity, i.e. the ratio P/P_C, is considered, instead of P, the semilog plots become practically coincident, independently of the particular pore shape (see cross-hatched area in Figure A1. 3). From the same Figure A1. 3, we can estimate that for a normalized porosity of 0.3, the relative MSA is about 0.5; this means that a mechanical property (the Young's modulus or other) has about one half of the value than for the solid. The normalization of porosity, as a consequence, may be seen as a quick way for estimating the scaling of mechanical properties with increasing porosity content, on the basis of a single "universal" property-porosity curve.

The highest strength to mass ratio is probably achieved by particular cellular ceramics made by the sintering of hollow microbeads, like those obtained by Green and Hoagland[19], based on the viscous flow sintering of compacts of glass spheres. The key advantage of sintering ceramic beads, compared to direct foaming, is the greater uniformity of wall thickness of the same basic hollow elements, which is retained almost completely after sintering. For the samples with the lowest density, there is only a small contact area between adjacent beads, so that two types of porosity are available, that due to the cavity of spheres (internal porosity) and that from the packing of spheres (external porosity). The mechanical behaviour, for low density (and poor sintering) can be described only by using a semi-empirical MSA approach or a specific model

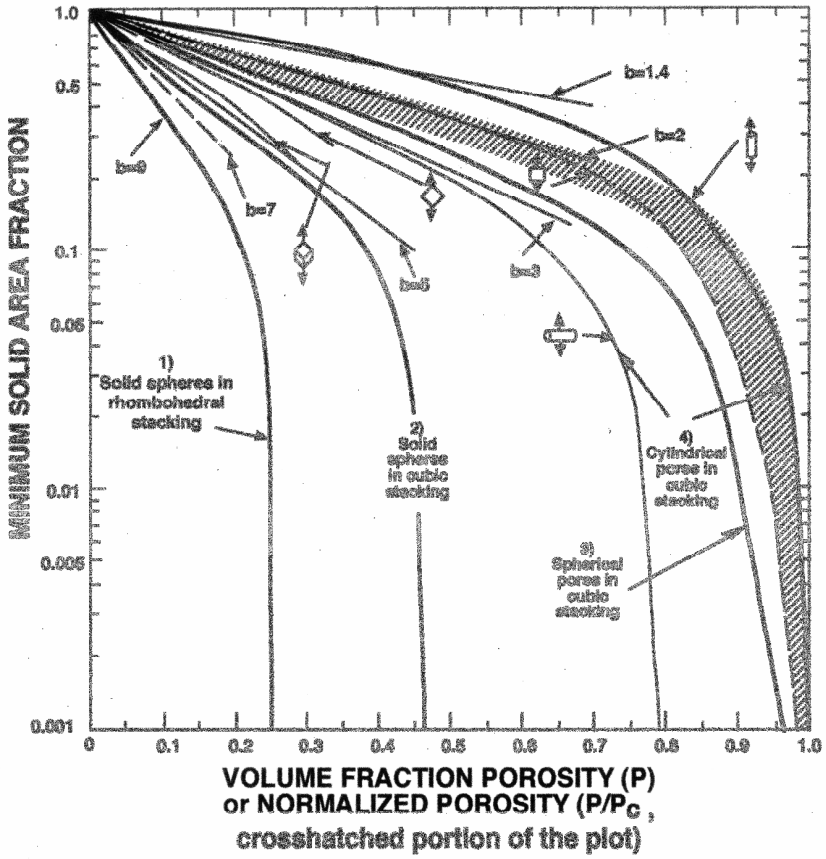

Figure A1. 3- Semi log plots of relative MSA vs. porosity. Critical porosity values are shown for different models based on several packing or stacking of cells or solid elements; the plots become coincident (cross hatched area) by considering normalized porosity (P/P_C) instead of the porosity volume fraction. From [3], with permission.

by the same Green and Hoagland[20]. GA models may be applied when sintering of hollow beads is so relevant that bead walls merge completely into cell walls.

The mechanical properties of honeycomb structures are essentially anisotropic. Owing to the fact that the cellular structure is defined in two dimensions (the same cross-section is replicated along the width of the structure), and not in three-dimensions like open-celled foams, from simple dimensional analysis it derives that there is a linear correlation between relative density and the ratio t/L[1]. Moreover, there is a linear correlation between the relative elastic modulus for a stress applied parallel to tubular pores, regardless of the cross-sectional geometry and the packing geometry of the pores[1]:

$$\frac{E}{E_S} = (1-P) = \rho_r \qquad (13)$$

The same (1-P) dependence represents the upper limit for other properties, such as fracture toughness or strength (flexural and compressive), when load is applied parallel to the pores[2,3]. The properties in the other directions are very different, with a remarkable dependence on the cross-sectional shape[2,21,22]; as a general trend, the

properties are much more scaled with porosity and feature critical porosity values, $P_C<1$. As an example, for a square section, the elastic modulus in directions normal to the pore orientation, but parallel to the cell walls, features a (1-P) dependence, with a proportional factor of about 0.5^2:

$$\frac{E}{E_S} \approx 0.5(1-P) = 0.5\rho_r \qquad (14)$$

Stressing in other directions causes a dramatic reduction of stiffness, which may be modelled by considering a greater dependence with porosity. The variation of elastic modulus in planes normal to the orientation of pores ("transverse" planes) may be summarized in polar diagrams such as that reported in Figure A1. 4, proposed by Gulati[23].

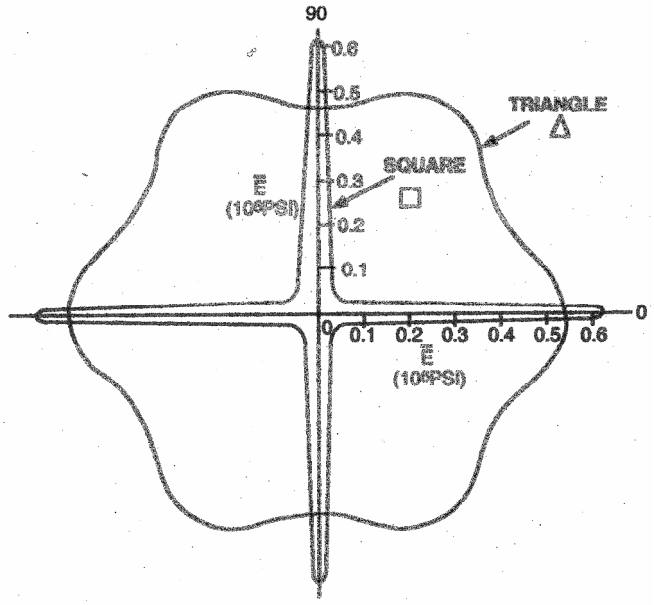

Figure A1. 4- Variation of the elastic modulus in "transverse" planes as a function of cell geometry. From [3], with permission

A fundamental comment that needs to be done concerning plots as the one reported in Figure A1. 4, is that cells with a triangular geometry lead to honeycombs with a drastically lower anisotropy than those with square geometry, due to the above reported stability of triangle based structures (Maxwell's criterion). Gibson and Ashby[1] reported a similar polar diagram, considering also the case of pores with hexagonal shape, which determine structures with a very low stiffness in the transverse planes (the behaviour is more isotropic than in the other cases, but E is slightly greater than the minimum for square cross sections).

The dependence of crushing strength on porosity, in ceramic honeycombs, is of great interest for applications in the automotive industry, where they are used as catalyst supports. Specific tests, with load applied in both parallel and transverse directions to

tubular pores, showed a compressive failure with a $(1-P)^2$ dependence on porosity, and a linear dependence on cell wall strength[3].

A particular type of cellular ceramic structure is that obtained assembling (sometimes sintering or bonding using organic or inorganic binders) randomly oriented fibres. These felts are employed for high-temperature insulation, and a typical example is that of tiles made from silica glass fibres for the thermal protection of the Space Shuttle. Green *et al.*[24,25] developed a relatively simple micromechanical model, by using load-bearing concepts based on the concept of fibre spacing. The model was successful in interpreting the anisotropy of the cellular bodies from fibre felts: it has been shown that more fibres are aligned in the tile plane than in the perpendicular (thickness) direction. If D_1 and D_2 are the fibre spacing in the tile plane ($D_1=D_2$), D_3 is the spacing in the third direction ($D_3>D_1$). The relative density of the cellular ceramic depends on the average fibre radius and on the three spacing values, as follows:

$$\rho_r \approx \pi r^2 \left[\left(1/D_3^{\,2}\right) + \left(2/D_2^{\,2}\right) \right] \tag{15}$$

The elastic moduli in the weak and strong directions, E_3 and E_2, respectively, may be correlated to the fraction of fibres aligned in those directions and the modulus of fibres, E_f:

$$E_3 \approx \pi r^2 E_f / (D_3)^2 , E_2 \approx \pi r^2 E_f / (D_2)^2 \tag{16}$$

The evaluation of strength derives from the evaluation of the flaw size, i.e. it focuses on the critical stress intensity factors, K_c, which are expressed as functions of fibre spacing:

$$K_{c3} = \pi r^2 \left(\pi / \left(2 D_3^{\,3}\right) \right)^{1/2} , K_{c2} = \pi r^2 \left(\pi / \left(2 D_2^{\,3}\right) \right)^{1/2} \tag{17}$$

where σ_{fb} is the fibre strength. The reference parameter is obviously that in the weakest direction, K_3, whose equation may be rearranged as follows:

$$K_{c3} \approx 1.67 \left(E_3 / E_f\right)^{3/4} \sigma_{fb} r^{1/2} \tag{18}$$

The elastic modulus of the cellular material, E_3, may be easily measured experimentally (for example by evaluating the sonic velocity), beyond evaluation of fibre spacing. The (minimum) failure strength σ_{f3} for a given (maximum) flaw size c may be calculated from usual fracture toughness equation, $K_{c3}=\sigma_{f3} (\pi c)^{1/2}$.

A.1.2 Thermal Properties

Thermal conductivity, heat capacity and thermal shock are of great importance for the applications of cellular ceramics, traditionally employed for thermal insulation (the refractory industry is probably the field in which the advantages of porosity were firstly recognized).

Thermal conductivity λ (W m^{-1} K^{-1}) expresses the proportionality between the temperature gradient per unit distance along one direction, $\partial T/\partial x$, and the heat flux (thermal power per unit area), normal to that direction, q', according to Fourier's law:

$$q' = -\lambda \partial T/\partial x \qquad (19)$$

Cellular materials are composite materials, in which one phase is a gas phase, usually air. This means that, in addition to the usual heat transfer mode for solids, thermal conduction, heat transfer modes within gas must be considered. Gasses are capable of conduction, convection, and radiative transfer (through the cell walls and voids)[1].

The total thermal conductivity, λ, derives from the superposition of the three contributions (conduction in both solid and gas, convection, radiation):

$$\lambda = \lambda_{COND,\,solid} + \lambda_{COND,\,gas} + \lambda_{CONV} + \lambda_{RAD} \qquad (20)$$

The convection contribution is very different for closed or open porosity. Natural convection is of importance, in closed cells, only when the Grashof number becomes equal to 1000 or greater; this reference number may be correlated to the cell size, as follows[1,26]

$$Gr = \frac{g\beta\Delta T_c L^3 \rho_{gas}}{\mu^2} \qquad (21)$$

in which g is gravitational acceleration, ΔT_C is the temperature difference across one cell, L is the cell size, ρ_{gas}, β and μ are the density, the volume expansion coefficient and the dynamic viscosity of the gas, respectively. Gibson and Ashby[1] calculated that the minimum cell size, for the Grashof number to of significance, is about 10 mm, normally larger than what is actually present in most cellular ceramics. As a consequence, the convection contribution, i.e. the intrinsic porosity contribution, to the overall thermal conductivity of closed cell foams is negligible.

Radiative transfer, through the "thermal" sub-group of electromagnetic radiations (mainly infrared radiation), between one surface at a temperature T_1 and the other at a temperature T_0, is ruled by Stefan's law:

$$q'_{RAD} = \beta_1 \sigma (T_1^4 - T_0^4) \qquad (22)$$

where σ is Stefan's constant, and β_1 expresses the emissivity of the surfaces. The Stefan's law refers to surfaces separated by a vacuum space; when a cellular solid is inserted, absorption and reflection of electromagnetic radiation occur at the solid phase[1]. Radiation is often dominant for cellular ceramics under high temperature gradients (>1000°C)[2].

Gibson and Ashby[1] proposed a simple model for the evaluation of the *optimum foam density* for thermal insulation, for a closed cell material, subjected to conduction and radiative transport. Conduction varies linearly with increasing relative density, from the low value of the conductive coefficient of a gas to that of solid, multiplied by an efficiency factor (equal to 2/3). Thermal conduction follows a (slightly) modified rule of mixture, and porosity plays only a "dilution" effect to the conduction of the solid phase. The porosity dependence of radiative transport is more complex, since also the thickness of wall cells (t) is important; the transfer primarily increases with cell size (and its degree of openness), which is directly correlated to the radiative path length[2]. The absorption of infra-red radiation (expressed by Beer's law $q'=q'_0e^{-Kt}$, where K is the extinction coefficient) is simply due to the solid phase (possessing an extinction coefficient K_S) [1]. The GA model is expressed by the following equations (it must be noted that the properties of the surfaces separated by the cellular solid must be known, so that the optimum conditions depend on factors not strictly related to the structure of the material):

$$\lambda = \lambda_{COND(SOLID,GAS)} + \lambda_{RAD}$$

$$\lambda_{COND(SOLID,GAS)} = \frac{2}{3}\rho_r\lambda_{COND,solid} + (1-\rho_r)\lambda_{COND,gas} \qquad (23)$$

$$\lambda_{RAD} = 4\beta_1\sigma \cdot T_m^{\ 3} \cdot t \cdot e^{-(K_S\rho_r t)}$$

T_m is the average temperature $(T_1+T_0)/2$. The relative density for achieving minimum conductivity is simply the value at which $\partial\lambda/\partial\rho_r = 0$, and assumes the following expression:

$$\rho_{r\,opt} = \frac{1}{K_s}\ln\left\{\frac{4K_s\beta_1\sigma t^2 T_m^{\ 3}}{\frac{2}{3}\lambda_{COND,solid} - \lambda_{COND,gas}}\right\} \qquad (24)$$

Ashby[5] has recently proposed a revised model for thermal conduction, which is intended to avoid the fact that models with a efficiency factor of 2/3 (or 1/3), although valid for very low density foams, obviously breaks down when relative density approaches 1. The more recent model features a more complex dependence on relative density:

$$\lambda_{COND(SOLID,GAS)} = \frac{1}{3}\left(\rho_r + 2(\rho_r)^{3/2}\right)\lambda_{COND,solid} + (1-\rho_r)\lambda_{COND,gas} \qquad (25)$$

For open cell materials, convection plays a fundamental role. More precisely, *forced convection* occurs, i.e. the heat transport depends on the flow of the fluid in the pores. This in turn depends on external forces (when the fluid passes through the cellular material, as in heat exchangers) or internal forces (when the flow arises from a chemical reaction, developing gasses within the cellular material, as in porous burners). The consequences of forced convection are that the thermal conductivity generally becomes anisotropic (we can experience one value for thermal conductivity in the direction of flow and another in transverse directions) and the convection contribution depends on the cell geometry. MSA models may represent a valid semi-empirical reference for inferring a convection/porosity correlation.

The specific heat capacity c_P (J kg^{-1} K^{-1}), i.e. the capability of a material to store energy as heat, has a simple linear dependence with the porosity, not based on volume fractions but rather on weight fractions[1,26]:

$$c_{P,\,foam} = c_{P,\,solid}(m_{solid}/m) + c_{P,\,gas}(m_{gas}/m) \quad (26)$$

where m, m_{solid} and m_{gas} are the total mass, the mass of the solid phase and the mass of the gas phase, respectively. The weight fraction of the gas phase is normally so small that the heat capacity of a cellular material is practically coincident to that of an un-foamed solid.

Thermal stress and thermal shock resistance are of vital importance for ceramics in high temperature applications. In general, a temperature variation causes a strain ruled by the thermal expansion coefficient α:

$$\varepsilon_{thermal} = \alpha\Delta T \quad (27)$$

If the strain is hindered, a thermo-elastic stress arises, as a function of the Young's modulus and (in the case of strain hindered in 2 or 3D) the Poisson's ratio. For a mono-dimensional strain we can write:

$$\varepsilon = \varepsilon_{thermal} + \varepsilon_{elastic} = \alpha\Delta T + \sigma_{elastic}/E = 0 \Rightarrow \sigma_{elastic} = -E\alpha\Delta T \quad (28)$$

Similar stresses arise when a material separates two zones at different temperature. Due to their intrinsic brittleness, ceramics fail under low tensile stresses, and these may be due to temperature changes, when the contraction, upon cooling, is hindered. Note that in ceramic materials, hindering the expansion occurring upon heating is less critical, as it causes compressive stresses in the component.

The increase of porosity in cellular ceramics, leading to a decrease in the elastic modulus, is essentially the only way to improve the "thermo-elastic" resistance of a component, since the coefficient of thermal expansion is not changed by the presence of porosity. The already reported thermal stresses generally refer to slow temperature variations; rapid variations are even more critical, and produce the "thermal shock" phenomenon. In the thermal shock, the thermal strain associated to temperature

variation may be seen as “self-hindered”: upon fast cooling, for example, the external part of the component is first cooled, and its contraction is hindered by the internal part, still at a higher temperature. The stress produced by thermal shock is ruled by the same equation as the thermal stress for bi-dimensional elements, and this is consistent with the fact that stress arises along all the external surface (i.e. on a bi-dimensional plane) [1]:

$$\sigma = \frac{E\alpha\Delta T}{1-\nu} \tag{29}$$

Fracture occurs when the thermo-elastic stress exceeds the fracture strength. As shown by Orenstein, Green and Vedula[27,28,29], the key factor for thermal breaking is the temperature gradient across the bulk. For a given fracture strength σ_s, we can obtain the maximum allowable temperature drop, which is known as the “hard” thermal shock parameter R_1[26]:

$$\Delta T_{max} = \frac{1-\nu}{E\alpha}\sigma_s = R_1 \tag{30}$$

For a cellular material, since strength and elastic modulus are scaled with respect to those of the fully dense solid by $(\rho_r)^{3/2}$ and $(\rho_r)^2$ factors, respectively, Gibson and Ashby[1] reported the scaling of the thermal shock parameter, as follows:

$$\Delta T_{max\,FOAM} = \frac{0.2\Delta T_{max\,SOLID}}{(\rho_r)^{1/2}} \tag{31}$$

where ΔT_{fs} is the thermal shock parameter of the fully dense solid. High porosity leads to an enhanced thermal shock resistance. The microstructural reason for this behaviour is that struts can accommodate thermal stress by bending; some special processing, acting on the struts characteristics (e.g. enhanced strength due to reduced flaw population), may result in materials with a notably high shock resistance, as shown by Colombo *et al.*[13]. Fend et al.[26] reported another thermal shock parameter, a “soft” parameter, R_2. This parameter is not simply related to the sudden temperature difference, but also considers the maintenance of this temperature difference as a function of time, so that the effect of the thermal conductivity is additionally considered.

$$R_2 = \lambda\frac{1-\nu}{E\alpha}\sigma_s \tag{32}$$

Long-term damage is better represented by this soft parameter. High thermal conductivity causes a rapid homogenisation of temperature, and consequently a rapid decrease of thermal stress. The low thermal conductivity of foams determines a reduction of the soft parameter with respect to the hard parameter. Ceramic foams are

also described by considering the ΔT_{10} parameter ,or the so-called "damage" parameter (D)[26]; the first represents the temperature drop at which local damage causes a 10% reduction of Young's modulus; the second is based on the ratio between the elastic modulus after shock, E, and the elastic modulus in the as-received condition, E_0:

$D=1-E/E_0$

A.1.3 Electrical Properties

The most interesting electrical properties, in cellular ceramics, are the dielectric constant and the electrical resistivity. The first property is typically considered for ceramic materials, which are generally insulators so that electric charges tend to be stored by the material and polarized by an applied electrical field. The second property is of interest mainly for cellular ceramics containing a particular conductive or semiconductive solid phase, as in the case of carbon[30] or SiC foams[31]. Sometimes electrical conductivity results from an insulating primary solid phase embedding or coated by a conductive secondary phase, like in honeycombs made from porcelain ceramics embedding coal tar pitch[31,32]. Conductive or semiconductive foams are of growing interest for porous, electrically powered, heaters[31].

The effect of porosity on the (relative) dielectric constant (adimensional), according to Gibson and Ashby[1,5], is very simple, due to the fact that pores decrease the volume of material capable of polarization (alignment of separate internal opposite charges under applied electric field), with a dielectric constant of ε_s, commonly substituting it by air, whose dielectric constant is practically coincident with that of vacuum (ε=1). Thus:

$$\varepsilon_{FOAM} = 1 + (\varepsilon_s - 1)\rho_r \qquad (33)$$

An alternating voltage between two metallic plates separated by vacuum (or a "perfect" dielectric) produces a current flow that leads the voltage by 90°. This is due to the fact that in vacuum (or in a perfect dielectric) polarization is immediate. No actual material is perfectly dielectric, so that its polarization employs some time, which in turn causes the current to lead the voltage by 90-δ[33]. The tangent of the angle of deviation, multiplied by the dielectric constant, represents the loss factor, D, which expresses the fraction of power dissipated within the dielectric, important for microwave applications. The higher the porosity of the dielectric, the lower the fraction of "real" dielectric (pores are filled with air, i.e. they carry a fraction of ideally dielectric material), so that the loss factor for a cellular material is described by:

$$D_{FOAM} = D_{SOLID}\,\rho_r \qquad (34)$$

where D_0 is the loss factor of the fully dense solid.

Rice[2] reported that the linear relative dielectric constant/porosity correlation is one special case of a more general equation, following an approach similar to that employed for composites. In a multiphase material, the dielectric constant depends on the volume fraction, ϕ_i, of each phase (solid and pores for a cellular material) as follows:

$$\varepsilon^n = \Sigma_i \phi_i \varepsilon_i^n \tag{35}$$

If the exponent n is equal to –1 or +1, serial (rules of mixture) and parallel mixing are respectively obtained, which represent the upper and lower bound for several models. Most models use the expression $\varepsilon = \varepsilon_S$ (1-AP), in which the average A parameter ≈1, but the deviations are rather large (0.8-1.5, the lowest values corresponding to ceramics with very low relative density[34]).

Gibson and Ashby[1] modelled the electrical resistivity ρ_{el} (the potential gradient divided by the current per unit area, Ωm) in analogous manner to thermal conduction. As a consequence, the conductivity σ (the reciprocal of resistivity) increases linearly with relative density. The proportionality coefficients express the tortuosity of the path of the charges in the cellular material under the applied electrical field.

Rice also[2] showed the similarity between models for electrical conductivity and thermal conductivity. In both cases, a flux (a flux of electric charges, i.e. a current, or a heat flux, i.e. thermal power) is referred to a surface of transmission. The MSA approach, focused on the concept of relative cross-sectional area as a scaling factor, provides satisfactory models; the geometrical elements (spheres, cylinders) and their packing and stacking provide a modelling of the above mentioned tortuosity of charge paths. The key difference between thermal and electrical conductivity is constituted by percolation, i.e the existence of a critical volume fraction of conductive phase for achieving a significant conductivity. A dispersed conductive phase gives conductivity, embedded in an insulating matrix, when its volume fraction allows an effective electrical contact between adjacent conductive particles[2].

Martin and Adler [31] reported a model, developed by McLachlan[35], that combines MSA and percolation theory, useful for the evaluation of conductive or semiconductive foams. The conductivity of a composite mixture of insulating and conductive phases, σ_M, is ruled by the McLachlan equation:

$$\phi_i \frac{\sigma_i^{\frac{1}{s}} - \sigma_M^{\frac{1}{s}}}{\sigma_i^{\frac{1}{s}} + \left(\frac{1}{\Phi} - 1\right)\sigma_M^{\frac{1}{s}}} + \phi_c \frac{\sigma_c^{\frac{1}{t}} - \sigma_M^{\frac{1}{t}}}{\sigma_c^{\frac{1}{t}} + \left(\frac{1}{\Phi} - 1\right)\sigma_M^{\frac{1}{t}}} = 0 \tag{36}$$

where ϕ_i and ϕ_c are the volume fractions of the phases and Φ is the critical volume fraction for percolation; σ_i and σ_M are the conductivities of the phases; s and t are two

equation parameters. For foams, the conductivity of voids (the insulating phase) is almost zero compared to the solid ceramic phase, so that a simplified equation may be written:

$$\sigma_M = \sigma_C \left[\frac{\frac{1}{\Phi} - 1 - \frac{\phi_i}{\phi_c}}{\left(\frac{1}{\Phi} - 1\right)\left(\frac{\phi_i}{\phi_c} + 1\right)} \right]^t \qquad (37)$$

The electrical properties of honeycombs depend on simple geometrical aspects[31]. "Longitudinal" resistance (along the direction parallel to tubular pores) is scaled on the cross-sectional area. The resistance of fully dense solid is defined by $R = \rho_{el} L/A$, where L is the width and A is the cross-sectional area. For honeycombs, the cross-sectional area is a fraction of A, A_h, so that $R_h = \rho_{el} L/A_h$. As a consequence, we obtain:

$$R_h = \rho_{el} \frac{L}{A_h} = R \frac{A}{A_h} = R \frac{V}{V_{solid}} = \frac{R}{1-P} \qquad (38)$$

Gerson and Marshall[36] developed a model substantially based on MSA approach for the *electric breakdown*, i.e. the formation of highly localized, conductive paths within a porous dielectric material. After breakdown, the dielectric properties are no longer maintained, since the material is practically a conductor. This transformation is often accompanied by localized melting and vaporization or localized fracture. Electrical breakdown is assumed to occur in "columns" determined by the alignment of pores (modelled into cubic cells in simple cubic stacking) in which the amount of material is below the breakdown level of the fully dense solid[2]. The probability of finding x number of cells with pores aligned in columns of n cells (n is the ratio of pore diameter to specimen thickness) is dependent on porosity P [2]:

$$p = (P)^n(1\text{-}P)^{n-x} \qquad (39)$$

The probability of finding, over many samples, column with the maximum number of voids (causing electric breakdown), $p(x_{max})$, depends on the total number of columns in the sample, N: $p(x_{max}) \approx N^{-1}$

The probability of one particular sample having a column with x_{max} voids, for large N values (small pores to specimen dimensions) $\approx 1\text{-}e^{-1} \approx 0.63$. The resultant breakdown/porosity correlation is very close to a e^{-bP} correlation (linear curve in semilog plots), with the b factor generally increasing with pore diameter[2].

A.1.4 Acoustic Properties

Cellular solids are often employed for the damping of acoustic waves and vibrations. A good damping capability, in cellular ceramics, may be coupled to other properties, in several applications. Due to their refractoriness, cellular ceramics may be employed as acoustic liners inside combustion chambers, for damping combustion oscillations [37]. Cellular glass is commonly used in the building industry as lightweight aggregate in concrete with a good sound absorption, thus coupling mechanical strength (much superior to that of polymeric foams) and acoustic damping[37,38]. Cellular ceramics are widely employed as noise barriers in road tunnels[37], thus coupling sound absorption and durability.

Modelling the acoustic properties of porous media is very difficult since it involves complex equations, mostly derived from Biot's theory[39] and later extensions proposed by Lambert[40,41,42,43]. Gibson and Ashby[1] proposed a much simplified model, based on the expression of the sound velocity along a rod of solid material, with a small thickness compared to the wavelength, $v = (E/\rho)^{0.5}$, where E and ρ are the elastic modulus and the density of the solid. The equation may be applied to most cellular solids, since the condition of the wavelength of sound waves to be much longer than cell size is generally fulfilled (typical wavelengths are in the range 50 mm-5m). The scaling expressions for elastic modulus rule the scaling factor of sound velocities, as follows:

$$v = \sqrt{\frac{E_{FOAM}}{\rho_{FOAM}}} \propto \sqrt{\frac{E_{SOLID}}{\rho_{FOAM}}}\rho_r \qquad (40)$$

The acoustic properties, however, are not based only on a "dilution" of (solid) material capable of transmission of mechanical impulses. Complex fluid-structure interactions (including thermal effects) should be considered. Göransson[44] focused on an acoustic parameter, static flow resistivity (Rayls m^{-1}), which scales on $(\rho_r)^2$ (the lower the density, the highest the resistance to propagation of mechanical waves), and also on the strut cross dimension (the smaller the strut dimension, the highest the resistance).

A.1.5 Permeability

The study of the flow of fluids in a cellular ceramic is very important for evaluating the performance of these components in several important engineering applications, such as filtration, fluid mixing, catalysis of chemical reactions. The permeability of porous media corresponds to the ease with which a fluid (gas or liquid) passes through the cellular structure under a pressure gradient. For a given volumetric flow rate Q and a given exposed surface area A, we have a fluid velocity v = Q/A which can be correlated to the pressure gradient dP/dx by Darcy's law (linear correlation) or by

Forchheimer's equation (parabolic correlation), by means of the fluid absolute viscosity μ and density ρ[45], for incompressible fluids (equations reported in both differential and integral forms):

$$-\frac{dP}{dx}=\frac{\mu}{k_1}v \Rightarrow \frac{P_{IN}-P_{OUT}}{L}=\frac{\mu}{k_1}v \qquad \text{[Darcian permeability]} \quad (41)$$

$$-\frac{dP}{dx}=\frac{\mu}{k_1}v+\frac{\rho}{k_2}v^2 \Rightarrow \frac{P_{IN}-P_{OUT}}{L}=\frac{\mu}{k_1}v+\frac{\rho}{k_2}v^2 \qquad \text{[Non-Darcian perm.]} \quad (42)$$

where L is the medium thickness along the flow direction, P_{IN} and P_{OT} are the entrance and exit pressures, respectively. The equations are slightly different for gasses or vapours (compressible fluids):

$$-\frac{P_{IN}^{\ 2}-P_{OUT}^{\ 2}}{2PL}=\frac{\mu}{k_1}v \qquad \text{[Darcian permeability]} \quad (43)$$

$$-\frac{P_{IN}^{\ 2}-P_{OUT}^{\ 2}}{2PL}=\frac{\mu}{k_1}v+\frac{\rho}{k_2}v^2 \qquad \text{[Non-Darcian permeab.]} \quad (44)$$

P is the pressure at which v, μ and ρ are evaluated. The Darcian correlation considers only viscous effects, while the non-Darcian correlation is more general, taking into account also inertial and turbulence effect. The factors k_1 and k_2 represent the contribution of the porous media to permeability, and these must be scaled to the porosity and pore shape. Although straightforward in the definition, the k_1 and k_2 permeability factors are quite difficult to estimate for most cellular bodies.

The starting point for the evaluation of permeability factors is essentially constituted by equations firstly developed for unconsolidated granular media, such as the one by Kozeny-Carman[45]:

$$k_1=\frac{P^3}{K_K S_o^{\ 2}(1-P)^2} \qquad (45)$$

where P is the void fraction (porosity), S_0 is the specific surface area of granules, K_K is the Kozeny parameter (K_K = 4.8-5.0, depending on the "regularity" of particles). Ergun[45] proposed semi-empirical equations, by using some geometrical models for the powder shape (spheres, cylinders etc.), which are taken into account by the equivalent particle diameter d_p, determined by considering the specific surface area ($d_p = 6/S_0$)

$$k_1 = \frac{P^3 (d_p)^2}{150(1-P)^2}$$
$$k_2 = \frac{P^3 (d_p)}{1.75(1-P)} \qquad (46)$$

Analogous equations are available for fibrous media.

The permeability characteristics of foams depend essentially on the processing route employed for their fabrication (either the replica of polymeric templates – "reticulated" ceramics, the burn-out of sacrificial fillers or the direct foaming of ceramic slurries – see later). In fact, this determines their macrostructure (in particular the presence of cell walls).

The permeability of ceramic replicas is influenced mainly by their nominal pore count, i.e. the number of pores per unit length (3-100 ppi, i.e. "pores per inch"), which is obviously linked to the average cell size (note that one can produce ceramic foams with a similar relative density – i.e. the same amount of void, permeable volume – and different cell size). The higher the pore count, the lower is the permeability, due to the increase in the number of cell boundaries (struts) per unit length (the fluid flow is more conditioned by attrition and turbulence). Although a general decrease of permeability factors with nominal pore count can be found (almost linear in a semilog plot) [45], there is no univocally accepted model, due to the fact that permeability is also affected by other parameters, such as thickening of struts upon coating the organic template with an increased slurry content (a significant increase of relative density, from 0.05 to 0.25, due to thicker struts can for instance cause a dramatic decrease of permeability, of about 90%, besides a ~20-fold increase in crushing strength). As a general trend[45], for reticulated ceramics with different pore counts, cells have an almost constant geometry, so that permeability is ruled mainly by pore size. If the cell size is instead kept constant, the permeability then is mostly correlated to the amount of porosity in the body.

Modified Ergun equations are employed to fit the data for ceramic replicas:

$$k_1 = \frac{P^3}{\alpha S_o^{\,2}(1-P)^2}$$
$$k_2 = \frac{P^3}{\beta S_o (1-P)} \qquad (47)$$

α and β are functional parameter of the equivalent diameter:

$$\alpha = 973 d_c^{\,0.743}(1-P)^{-0.0982}$$
$$\beta = 368 d_c^{\,-0.7523}(1-P)^{0.07158} \qquad (48)$$

The equivalent diameter is again dependent on the specific surface area:

$$S_0 = \frac{4P}{d_c(1-P)} \tag{49}$$

The permeability factors may be linked also to more sophisticated equations (based on "tortuosity" factors, which may be determined by measures of electrical conductivity [45,46]) or by more empirical equations, such as:

$$k_1 = \frac{P^3(d_p)^{0.264}}{1.36x10^8(1-P)^2}$$
$$k_2 = \frac{P^3(d_p)^{-0.24}}{1.8x10^4(1-P)} \tag{50}$$

Cellular ceramics based on the foaming of slurries (gel-cast foams) exhibit a dependence of the permeability on open porosity (the processing causes the presence of cell walls, which have different degrees of openness – cell window size), linearly increasing in semilog plots; the dependence on pore diameter, in semilog plots, is rather peculiar, since permeability factors are very low for pore diameters below 20 μm, but increase steeply to an almost constant value.

The permeability constitutes a key factor in designing honeycombs for several applications, such as automotive emission catalysis and abatement, catalytic combustion, heat-exchange, diesel particulate filtration, etc. The flow modes are essential for modelling the permeability, mainly focused on pressure drop; in fact, cells can be open at both ends and operate like parallel channels or can be partially sealed and connected with each other, so that fluids may experience a complex path within the cellular solid and a longer lasting chemical and physical interaction with the solid surfaces. For the first kind of honeycombs, the pressure drop is simply affected by the viscous friction and turbulence inside the parallel channels, and it is simply modelled on a friction factor f and a hydraulic parameter d_h (equal to four times the cross-sectional area exposed to flow divided by the sectional wetted perimeter):

$$\Delta P = \frac{f\rho_{fluid}Lv^2}{2d_h} \tag{51}$$

It has been shown[45] that there is a critical length L_e, for open, straight, honeycombs since friction, upon entrance of a fluid in the cellular structure, causes flow alterations, adjusted only after a certain distance; the critical length depends on the upstream conditions (laminar or turbulent flow). For honeycombs shorter than the critical length, the permeability of the cellular structure resembles that of perforated plates or screens, and strongly depends on porosity, expressed by the fraction of area open for flow, φ:

$$\Delta P = \left(\frac{1}{Y^2 C^2}\right)\left(\frac{1-\varphi^2}{\varphi^2}\right)\frac{\rho_{fluid} v^2}{2} \qquad (52)$$

C is dependent on the flow conditions and Y is the expansion coefficient for gasses (Y=1 for liquids) [45]; both parameters are reported in charts available in the literature.
The pressure drop for honeycombs with complex flow paths derives from three different components, due to pressure drops across the porous walls, across the passageways and due to changes in the flow area. Modified Kozeny-Carman's equations may be used to model each contribution.

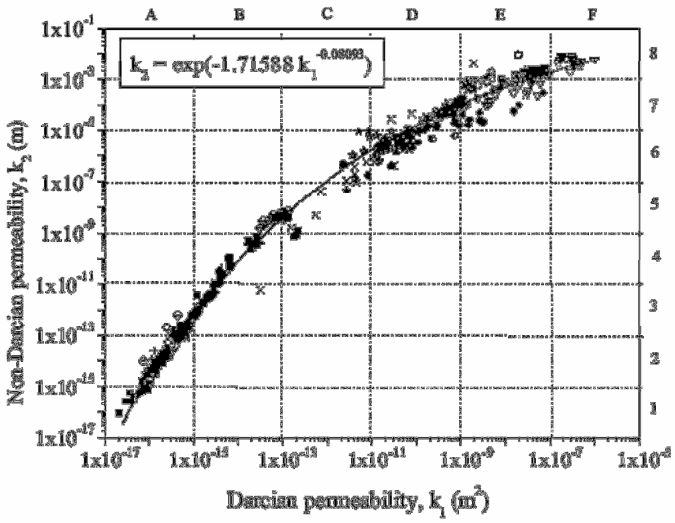

Figure A1. 5- Permeability data gathered from literature, adapted from [45].

The different permeability of different kinds of cellular solids can be summarized by "maps" having k_1 and k_2 as coordinates. The different permeability behaviour corresponds to different zones, as illustrated by Figure A1. 5. The overall correlation between the two factors is expressed by:

$$k_2 = e^{-\left(\frac{1.71588}{k_1^{0.08093}}\right)} \qquad (53)$$

k_1 and k_2 are here expressed in m^2 and m, respectively.

In conclusion, we can state that the various properties of cellular ceramics depend on several, interconnected parameters. However, as a generalization, we can say that the parameter that has the most influence on the various properties is the relative density (i.e. the amount of porosity) that the component possesses. In Figure A1. 1 we

show the qualitative trend of different engineering properties and characteristics of cellular ceramics (foams) with relative density.

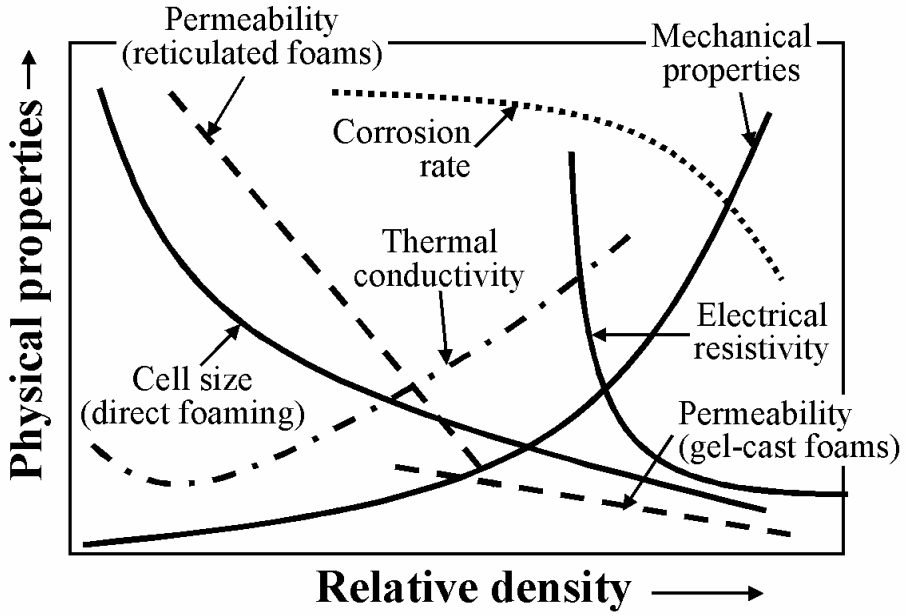

Figure A1. 6- Influence of porosity on some physical properties of cellular ceramics (adapted from [47]).

References

[1] L.J. Gibson and M.F. Ashby, "Cellular Solids, Structure and Properties," 2nd edition. Cambridge University Press, Cambridge, UK, (1999).
[2] R. Rice, "Porosity of Ceramics," Marcel Dekker, Inc., New York, NY (1998).
[3] R. Rice, Mechanical Properties, in "Cellular Ceramics: Structure, Manufacturing, Properties and Applications", M. Scheffler and P. Colombo eds. WILEY-VCH Verlag GmbH, Weinheim, Germany, 291-312 (2005).
[4] Ashkin, D., Haber, R.A., Wachtman, J.B., *J. Am. Ceram. Soc.*, *73*, 3376-81 (1990).
[5] M.F. Ashby, Cellular Solids – Scaling of Properties, in "Cellular Ceramics: Structure, Manufacturing, Properties and Applications", M. Scheffler and P. Colombo eds. WILEY-VCH Verlag GmbH, Weinheim, Germany, 3-17 (2005).
[6] V.R. Vedula, D.J. Green, J.R. Hellmann, *J. Am. Ceram. Soc.*, *82*, 649-56 (1999).
[7] Colombo, P., Bernardo, E., Biasetto, L. *J. Am. Ceram. Soc.*, *87*,152-154 (2004).
[8] Colombo, P., Bernardo, E. *Composites Science and Technology*, 63, 2353-59 (2003).
[9] Brezny, R., Green, D.J., The Mechanical Behavior of Cellular Ceramics, in "Materials Science and Technology – A Comprehensive Treatment", Vol.11, R.W. Cahn, P. Haasen, E.J. Kramer eds. VCH Publishers, Weinheim, Germany (1991).
[10] Brezny, R., Green, D.J., *J. Am. Ceram. Soc.*, *74*,1899-1905 (1991).
[11] J.G. Zwissler, M.A. Adams, Fracture Mechanics of Cellular Glass, in "Fracture Mechanics of Ceramics", R.C. Bradt, A.G. Evans, D.P.H. Hasselman, F.F. Lange eds. Plenum Press, New York, NY, 211-242 (1983).
[12] Colombo, P., Modesti, M., *J. Am. Ceram. Soc.*, *82*, 575-578 (1999).
[13] Colombo, P., Hellmann, J.R., Shellermann, D.L., *J. Am. Ceram. Soc.*, *85*, 2306-12 (2002).
[14] Colombo, P., Hellmann, J.R., *Mat. Res. Innovat.*, *6*, 260-72 (2002).
[15] Hasselman, D.P.H., *J. Am. Ceram. Soc.*, *54*, 442-453 (1962).
[16] Nielsen, L.F., *J. Am. Ceram. Soc.*, *67*, 93-98 (1983).
[17] Nielsen, L.F., *J. Am. Ceram. Soc.*, *73*, 2684-89 (1990).
[18] Rice, R., *J. Mat. Sci.*, *40*, 983-89 (2005).
[19] Green, D.J., Hoagland, R.G., *J. Am. Ceram. Soc.*, *68*, 395-98 (1985).
[20] Green, D.J., Hoagland, R.G., *J. Am. Ceram. Soc.*, *68*, 403-409 (1985).
[21] Day A.R., Snyder, K.A., Garboczi, E.J., Thorpe, M.F., *J. Mech. Phys. Solids*, *40*, 1031-51 (1992).
[22] Snyder, K.A., Garboczi, E.J., Day, A.R., *J. Appl. Phys. 72*, 5948-55 (1992).
[23] S.T. Gulati, A. Schneider, "Mechanical Strength of Cellular Ceramic Substrates" in Proc. Ceramics for Environmental Protection (Enviceram '88) Cologne, Germany, 12/7-9/1988, Deuthsche Keramische Gesellschaft e.V., Köln, Germany.
[24] Green, D.J., Lange, F.F., *J. Am. Ceram. Soc.*, *65*, 138-41 (1982).
[25] Green, D.J., Ritter, J.E., Lange, F.F., *J. Am. Ceram. Soc.*, *65*, 141-6 (1982).
[26] T. Fend, D. Trimis, R. Pitz-Paal, B. Hoffschmidt, O. Reutter, Thermal Properties, in "Cellular Ceramics: Structure, Manufacturing, Properties and Applications", M. Scheffler and P. Colombo eds. WILEY-VCH Verlag GmbH, Weinheim, Germany, , 342-360 (2005).
[27] Orenstein, R.M., Green, D.J., *J. Am. Ceram. Soc.*, *75*, 1899-905 (1992).
[28] Vedula, V.R., Green, D.J., Hellmann, J.R., *J. Mat. Sci.*, *33*, 5427-32 (1998).
[29] Vedula, V.R., Green, D.J.,, P., Hellmann, J.R., *J. Am. Ceram. Soc.*, *82*, 649-56 (1999).
[30] J. Klett, Carbon Foams, in "Cellular Ceramics: Structure, Manufacturing, Properties and Applications", M. Scheffler and P. Colombo eds. WILEY-VCH Verlag GmbH, Weinheim, Germany, 137-157 (2005)
[31] H.P. Martin, J. Adler, Electrical Properties, in "Cellular Ceramics: Structure, Manufacturing, Properties and Applications", M. Scheffler and P. Colombo eds. WILEY-VCH Verlag GmbH, Weinheim, Germany, 361-380 (2005).
[32] Alcaniz-Monge, J.A., Cazorla-Amoros, D., Linares-Solano, A., Morallon, E., Vasquez, J.L., *Carbon*, , *36*, 1003-9 (1998).
[33] R.M. Rose, L.A. Shepard, J. Wulff, "The Structure and Properties of Materials – Volume IV, Electronic Properties", John Wiley and Sons, Inc., New York, NY (1966).
[34] Fujiu, T., Messing, G.L., Huebner, W., *J. Am. Ceram. Soc.*, *73*, 85-90 (1990).

[35] McLachlan, D.S., Blaskiewicz, M., Newnham, R.E., *J. Am. Ceram. Soc.*, *73*, 2187-203(1990).
[36] Gerson, R., Marshall, T.C., *J. Appl. Phys.*, *30*, 1650-53(1959).
[37] I.D.J. Dupère, T.J. Lu, A.P. Dowling, Acoustic Properties, in "Cellular Ceramics: Structure, Manufacturing, Properties and Applications", M. Scheffler and P. Colombo eds. WILEY-VCH Verlag GmbH, Weinheim, Germany, 381-99, (2005).
[38] G. Scarinci, G. Brusatin, E. Bernardo, Glass Foams, in "Cellular Ceramics: Structure, Manufacturing, Properties and Applications", M. Scheffler and P. Colombo eds. WILEY-VCH Verlag GmbH, Weinheim, Germany, , 158-75 (2005)
[39] Biot, M.A., *J. Acoust. Soc. Am.*, *28*,168-178, and ibidem, 179-191 (1955).
[40] Lambert, R.F., *J. Acoust. Soc. Am. 72*, 879-87 (1982)
[41] Lambert, R.F., *J. Acoust. Soc. Am.*, *73*, 1131-38, and ibidem, 1139-46 (1983).
[42] Lambert, R.F., *J. Acoust. Soc. Am.*, *77*, 1246-47 (1985).
[43] Lambert, R.F., *J. Acoust. Soc. Am.*, *88*, 1950-9 (1990).
[44] Göransson, P., *Phil. Trans. R. Soc. A*, *364*, 89-108 (2006).
[45] M.D.M. Innocentini, P. Sepulveda, F. dos Santos Ortega, Permeability, in "Cellular Ceramics: Structure, Manufacturing, Properties and Applications", M. Scheffler and P. Colombo eds. WILEY-VCH Verlag GmbH, Weinheim, Germany, 313-41 (2005).
[46] Moreira, E.A., Innocentini, M.D.M., Coury, J.R., *J. Eur. Ceram. Soc.*, *24*, 3209-18 (2004).
[47] Sepulveda, P. *Am. Ceram. Soc. Bull.*, *76*, 61-65 (1997).

Appendix 2

Characterization of Structure and Morphology

A 2.1 Parameters describing the structure of the foams

The complete description of the complex, three-dimensional architecture of ceramic foams requires several structural parameters. Depending on the specific application, other characteristics may be relevant. Some important structural parameters are:

1) Cell size and its distribuition
2) Strut thickness and its distribuition
3) Strut shape and morphology (e.g. dense or hollow struts)
4) Cell window size (open or closed pores, degree of interconnectivity)
5) Degree of anisotropy (of porosity, of pore size, graded materials, etc.)
6) Surface to volume ratio[1], (presence of cell walls)

In Fig. A.2.1 a) the typical parameters of an open-cell microcellular ceramic foam and b) the schematic model adopted for mechanical properties interpretation are reported.

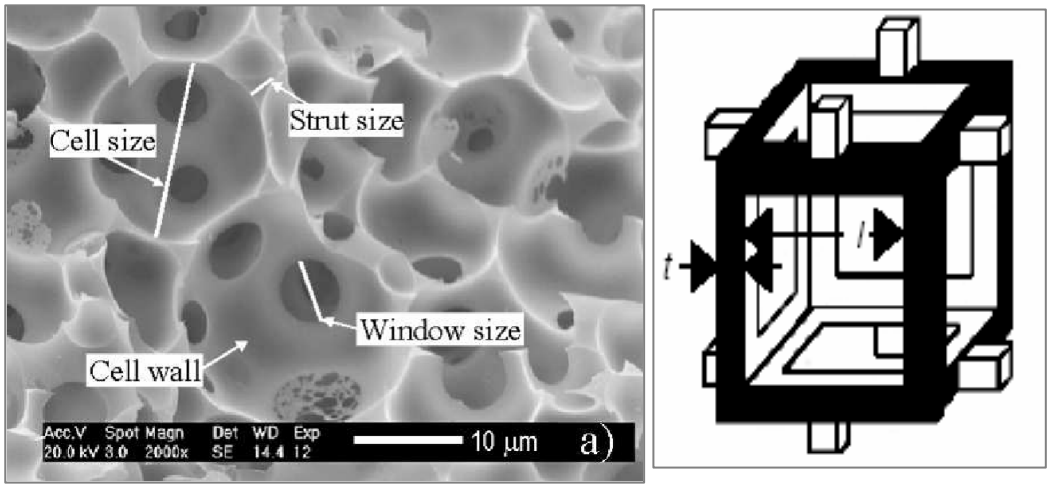

Figure A.2.1- Left: typical parameters of an open-cell mcrocellular foam; right: the schematic model for mechanical properties interpretation.

As mentioned in A.1, all these parameters strongly affect the material properties such as mechanical strength, thermal conductivity, and gas permeability ecc.

Although resolving the structure of cellular foams has been the subject of scientific research for some time, no simple standard experimental technique or procedure to determine some of these common structural parameters has been identified so far.

Although most of characterization techniques have proven their value in different fields of scientific research for several years, their potential in investigating the parameters

that describe the shape, isotropy and interconnectivity of single cells, as well as the isotropy and fractional density of the whole component, has yet to be explored in highly porous materials.

The following section of this chapter describes the Image Analysis technique used in the determination of some of the most relevant structural parameters of the polymer derived microcellular ceramic foams reported in Chapter 2.

As previously reported, SiOC foams were produced by mean of a commercial available silicon resin (MK, Wacher Chemie) and polymethilmetacrilate microbeads of different nominal sizes (10, 25, 50, 100 and 185 μm, samples S10, S25, S50, S100 and S185 respectively) as pores source (see also Chapter 2.2).

Expect Image Analysis, other methods are available from the literature such as the PPI (Pores Per Inch) and Visiocell.

In the PPI method the number of pores is counted over a standard length of one inch^2.

The linear intercept method was primarily used when manual measurements were required to obtain data, because they could be performed by drawing random lines on images of sections. Figure A.2.2. exemplifies this method on a micrograph of a polyurethane foam.

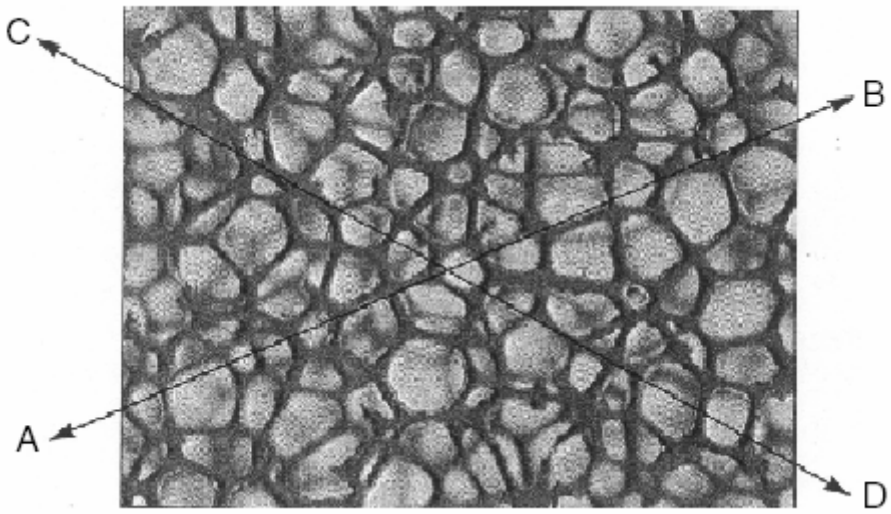

Figure A.2.2- Illustartion of the principle and the uncertainty of the ppi method

With modern computer-base instruments, it is usually easier to measure the intersection areas, which consist in a cross-sectional plane within the object.

This unit can be a little confusing and subjective because of:

1. The unclear definition of a “pore”: it can be a window or the full section of the cell.

2. The size of the pore: in case of a cell window, the size depends on the viewing angle. For the cell section, the size depends on the location of the section (top, middle, bottom).
3. The data scatter broadly within a sample: counting from A to B or from C to D in Fig. Leads to significant differences.
4. Analogous to other characterization techniques, dimensional reduction is an important issue: the cell is a three-dimensional feature of the foam, while ppi is a reduction of the volume to a linear, one-dimensional of a undefined unit (the pore). Under the assumption of spherical cells that are relatively uniform in size, a correction factor can be derived[3]:

$$D_{sphere} = \frac{t}{0.616} \quad (1)$$

Where D_{sphere} is the average sphere diameter and t the average cell chord length.

Because of the problems described above, the ppi method has not been universally accepted as an international unit; although it is widely used in industry Therefore, it is becoming increasingly less relevant in present-day characterization and will not be discussed further.

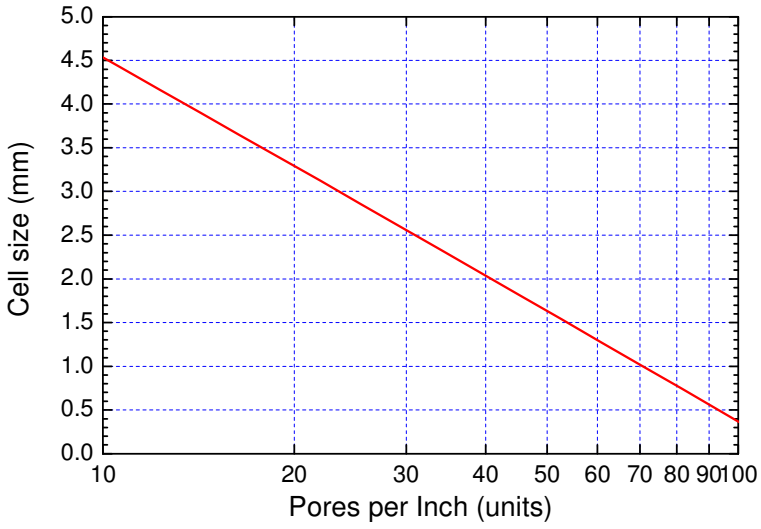

Figure A.2.3- Cell size (mm) and PPI relationship for a macrocellular foam[4]

Visiocell is a three-dimensional method based on light micrographs, originately developed by the company Recticel to characterize polyurethane foams[2]. The basis of this technique is an image of a horizontal section of a foam sample taken with a magnifying camera (Figure A.2.4).

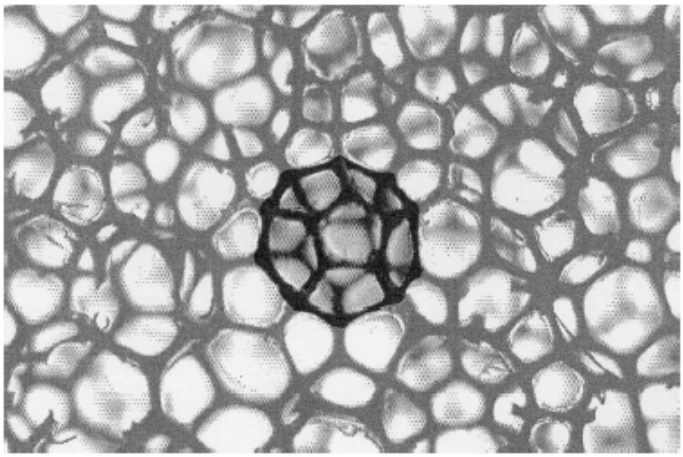

Figure A.2.4-Typical picture of a polyurethane foam with a cell diameter of approximately 1000µm.

A representative cell is selected by identifying its approximately circular shape comprising ten struts and one or two small pentagon(s) in its centre. These pentagons are the underside and/or upper side window(s). The actual measurement is performed by superimposing a calibrated ring, printed on transparent paper. The ring that most closely fits the cell in the image indicates the cell size in the foam. The cell diameter is in this case defined as the average between the internal and external circle of the ring. The accuracy of this technique is about 2%, and its nature only permits the determination of regular cell structures with cell sizes larger than 450 µm. The use of Visiocell in the characterization of ceramic foams is limited as it starts from the assumption of a uniform distribuition of spherical pores. Therefore, it can only be used for a fast estimate of cell size.

A 2.2 Image Analysis

Image analysis has proven its value in different fields of scientific research [5,6].
Common application fields include geology (simulation of permeability of porous stone, composition of coal or minerals), medicine (characterization of bone structure, analysis of medical images), biology (cell biology by selective staining, root quantification, particle counting), and materials science (grain size distribuition, microstructure of composite materials). Image analysis uses a series of image-processing routines to extract meaningful numerical information starting from an image. The results from an image analysis for a porous material can include several

important pore characteristics like the number of intersections, the perimeter, the pore size distribuition, the porosity, and the shape factor of the pores[7].

Principle

The image analysis routine typically requires several sequential processing steps[8]. Although these steps can differ depending on the kind of image and on the information one wants to obtain, a general outline of the procedure is described in the following.

1. *Image acquisition and input:*

   The conventional approach for image acquisition is microscopy. As the magnification of the image is governed by the pore size of the sample, this can be done by light or scanning electron microscopy (SEM). Careful preparation of the sample is required to obtain sufficient difference in brightness or contrast between ceramic material and the substance in the pore (air or imbedded material). One solution to the contrast problem consists of cutting thin slices, infiltrating the cellular material with resin, and finally polishing the plane of interest. Image analysis can also be performed on images from other sources, such as the two-dimensional slices from computerized X-ray microtomography. Figure A.2.5 shows some images obtained by optical microscopy and scanning electron microscopy of microcellular SiOC foams.

   In these images, the ceramic material is represented by the light areas, and the resin (or air) by darker areas.

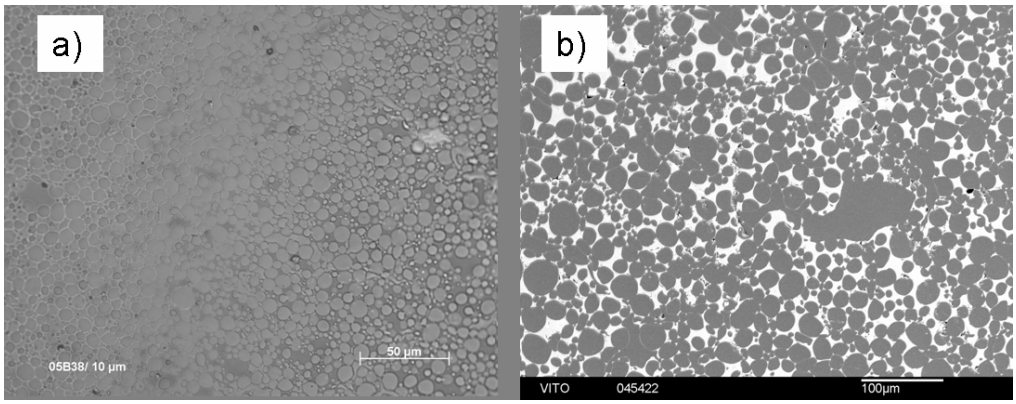

Figure A.2.5- Optical microscopy a) and Scanning elecron microscopy b) images of SiOC foams after impregnation

2. *Image enhancement*

Before image analysis is performed, some preliminary image enhancement is usually required. The selection of the region of interest (ROI), which is possible for a variety of geometrical or random shapes, excludes edge effects and incomplete representation of certain features by frame limitations. Image defects are suppressed by other functions, such as smoothing or median filtering for noise reduction, improvement of

contrast, correction for non uniform image illumination, low-pass filtering for correction of shading, and stray light effects. If necessary, image details can be improved to further enhance the visibility of features of interest.

3. Image thresholding

The next step, probably the most important in image analysis, is threshold segmentation, in which pixels that represent the actual feature of interest are identified in the image by analyzing relative pixel intensity. This can be an interactive manual procedure based on the grey-scale histogram. The histogram is a graph of the distribuition of red, green, blu, grey scale, hue, saturation, and/or lightness values in an image as a function of the number of pixels at each value. The lightness values of the image can range from black to white (grey values 0 to 255). In the ideal case, a clear separation of the pixel intensity of the feature of interest exists. Several threshold algorithms are available, depending on the type of image, the nature of the boundary, and so on.

In the case of porous materials, only two phases, air and solid, are of interest. However, most grey-scale images do not have a sharp boundary at the interface between the two different phases. Instead, there is a boundary region over a distance of several pixels in which the grey-scale changes gradually from one grey level to the other. This feature is illustrated in Figure A.2.7, which shows the unsharp, diffuse boundary in an image of the SiOC microfoams, obtained by FESEM, and the corresponding grey-scale histogram.

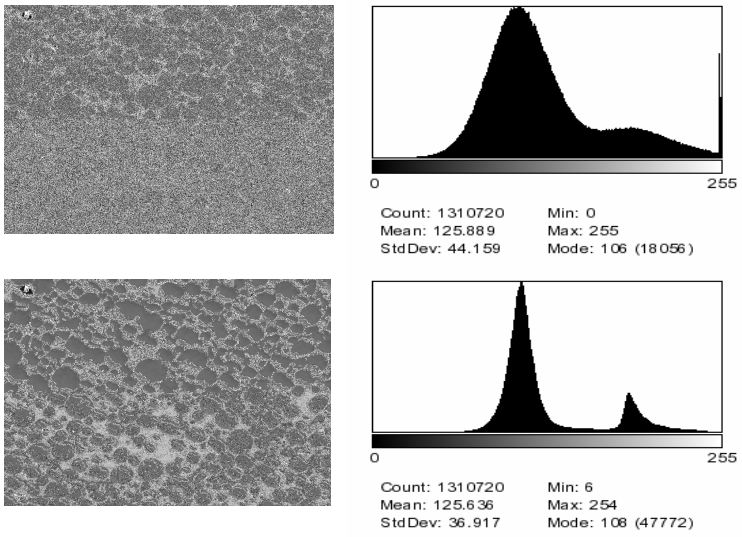

Figure A.2.7- Gry level distribuition, before (top) and after smoothing (bottom)

The maxima at 100 and 200 greylevels correspond to resin and ceramic material respectively. The minimum in the grey-scale histogram can be set as threshold for this image. Small changes in the threshold parameters alter the size of the regions of interest (i.e. the ceramic material) by changing the specific location in the boundary region where the pore is defined in the binary image. Inconsistent human judgements can and often do lead to operator-dependent measurements.

4. *Binary Image Processing*

When the thresholding procedure leaves artefacts behind, the use of combinations of erosion and dilation, which are binary image processing functions that compare pixels to their immediate neighbours, permits selective correction of the binary image details. The Euclidian distance function generates a distance-transformed image by assigning values to pixels within features that measure the distance to the nearest background point. It can be regarded geographically as a “landscape” with grey-scale hills and valleys. This distance map is used as input for the watershed function. This algorithm is a strong tool for separating touching convex shapes by flooding the valleys and finding the dividing lines between the different valleys in the “landscape”.

However, if the overlap is too great, this method will fail, and adjacent features are considered as being one. Thus, for samples with very low density, manual correction to identify the individual pores is laborious but indispensable. Skeletonization, also known as thinning, determines the skeleton, one pixel wide, of the white regions of the formerly defined binary image.

5. *Measurements:*

Once the features have been unambiguously identified by the routine, different measurements can be performed: counting features (with the possibility of eliminating features based on their size or shape), size measurements (length, perimeter, area), shape measurements (circularity), and intensity (topology, information on grey scale). The generated data are classified and can be analyzed statistically.

Figure A.2.8 gives an overview of the successive steps in the image analysis routine for measuring SiOC microcellular foams.

Alternative image analysis routines are based on granulometry: the pores are assumed to be particles whose size can be determined by passing them successively through meshes with increasing size and collecting what remains after each pass. Certainly for pores with more irregular shapes, this approach is advantageous, as no assumptions about the shape factor are made.

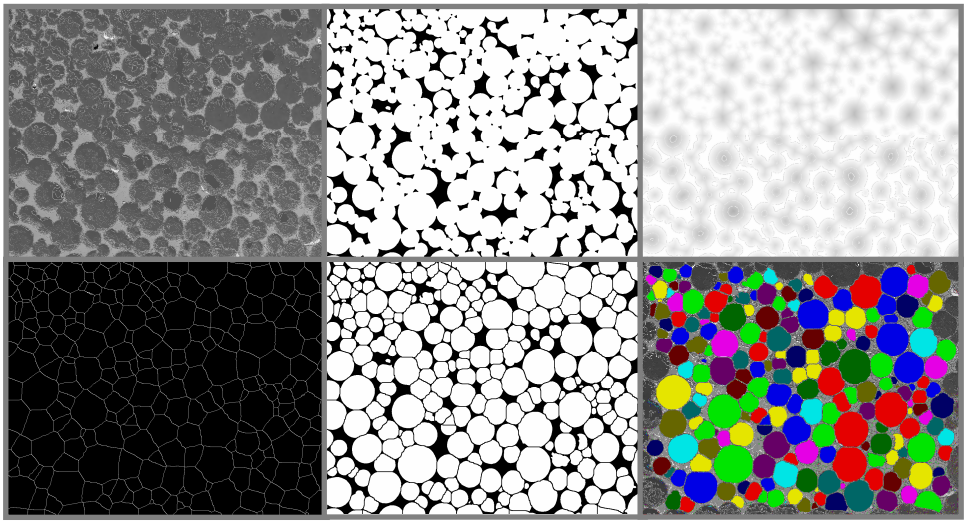

Figure A.2.8- Binary Image Processing. From top-left to bottom-right: FESEM image, binary image, euclidian distance map, skeletonization, pores count.

6. Interpretation of measured characteristics

Image analysis can quantitatively extract important structural parameters for porous materials. However apart from problems related to sample preparation (embedding, slicing, contrast…), other issues concerning the interpretation of the data must be addressed.

The pore size distribuition and other structural properties of the porous material are part of a three-dimensional pore space. The image analysis data are based on only two-dimensional sections. As the intersections through the individulal pores are randomly oriented in space, the pore size distribuition measured in this way will not completely represent the actual distribuition. Inevitably, the reduction from spatial morphologies to their planar sections results in most cases in a great loss of information. Only in the case of materials with well-defined pore shape and uniform pore size distribuition does an analytical solution for this reduction exist..

Several method and techniques have been proposed for obtaining three-dimensional information from two-dimensional images of the micro- and macrostructure.

The scientific and mathematical field dealing with the relationship between the data from two-dimesional images (either sections or projections) and the three-dimensional

reality of which they represent is called *stereology*[9,10] although a complete overview of the stereological approach is outside of the scope of this chapter , some general principles are described below.

Two aspects must be taken into account when converting the two-diemnsional data to the three-dimensional representation of the porous sample[11]. The cut-section effect deals with the fact that the intersection plane rarely cuts through the center of each pore. As a result, the pore size distribuition will be broader, even if the the reeal distribuition is monodisperse. For polydisperse distribuitions, the problem becomes even more complex, as samller features are less likely to be cut by a plane than larger features. This is known as the intersection-probability effect. Additional errors may originate from the presence of preferred spatial orientations and shape variations (e.g. elongated pores).

Mathematical theories to correct the two-dimensional data are mainly based on randomly distribuited spheres. Assuming a monodisperse distribuition of spheres, the intersection probability effect can be resolved by stating:

$$n_v = \frac{n_a}{D} \tag{1}$$

where n_v is the total number of spheres per unit volume , n_a the total number of spheres per unit area, and D the diameter of the spheres. This equation can be modified to apply a distribuition of other shapes.

The cut-section effects can be resolved analytically only for spheres. The function describing the probability of a random intersection of a sphere rises to a maximum near the diameter of the sphere. Hence, the mean intersection length is close to the ttrue three-dimensional size of the object. However, depending on the true three-dimensional shape and the preferred orientation of the pores, other sectional shapes will be produced[11]. This poses a serious limitation in calculating real-life samples, as deviations from perfect spheres and irregular pore forms will have substantial influence on the results.

Saltikov proposed a method of unfolding a population of intersection lengths into the true length using a function of the intersection lengths. This method works well for spheres and spherelike shapes. Large errors are introduced when more complex shapes are present[12,13].

Shape-related parameters can be included in some more advanced methods like an extended Scwarz-Saltikov approach or iterative solutions.

Another option for extracting three-dimensional data is serial sectioning. Apart from being time consuming and laborious, this method is rarely applicable to large enough volumes of material to give statistically meaningful data. Moreover, the section spacing in *z* direction limits the lower pore size detection[11,14]. The degree of anisotropy

can be estimated by comparing the parameters of the porus material in *x*, *y*, and *z* directions.

Specifications

The five foams samples were embedded in a resin and cut into thin sections. Images were digitally recorded under a FESEM (6340F, Jeol, Tokyo, Japan). For each sample three to five images were recorded, and the data averaged. Image analysis was performed with the KS400 routine version 3.0 (Carl Zeiss Vision GmbH), which allows the application of user-defined macros.

Samples S10, S25 and S50 were both authomatically and manually analyzed and results compared.

Results

1) Porosity:

The determination of the two-dimensional porosity of the foam sample is a relatively straightforward procedure provided the image has been thresholded correctly. The porosity is calculated as the count of pixels that rapresent pores on given surface[8,14].

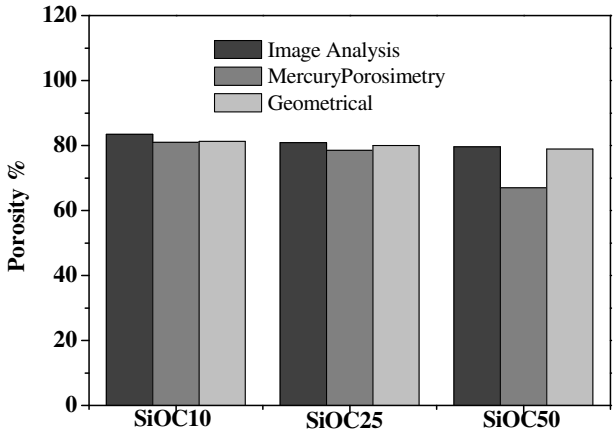

Figure A.2.9-Comparison of the average porosity calculated by image analysis, the geometrical porosity calculated and the porosity percentage measured by mercury porosimetry.

Figure A.2.9 compares the porosity measured by image analysis and the geometrical density (percentage of the theoretical.density). This can be regarded as an evaluation of the threshold process, as large and consistent differences would point to incorrect identification of pore boundaries**.**

2) Pore size distribuition

The results of the image analysis routine are parameters such as the area, the equivalent diameter, and the circularity of each pore. Pore size distribuitions can be derived from the calculation of the area of the individual pores in the thresholded image[5]. In this study, each pore area in the intersection plane was determined by counting the number of pixels in each pore, multiplied by the area of one pixel. Assuming spherical pores, the diameter of a circle with equivalent area D_{eq} can be calculated:

$$D_{eq} = 2 \cdot \sqrt{\frac{area}{\pi}} \tag{3}$$

The equivalent diameter can be classified in a histogram function by using a suitable bin size which can be fitted to an appropriate function. Anotehr option is topresent pore size distribuition as the cumulative pore fraction as a function of equivalent pore diameter. Depending on the number of pores in one image, this corresponds to 100 (for the largest pore size) to over 1100 pores that were analyzed. The calculation of the cumulative curve is based on the summation of all measurements. Small artefacts remaining in the image were removed by imposing a minimum equivalent pore diameter.

This procedure is exemplified in Figure A.2.9 for sample S25. Starting from a microscopiic image, a histogram classification of the equivalent pore diameter (as calculated from Eq.3) is obtained. The cumulative counts of four separate measurements showed a good agreement and the dot cumulative graph with black dots represent the average of the four measurements.

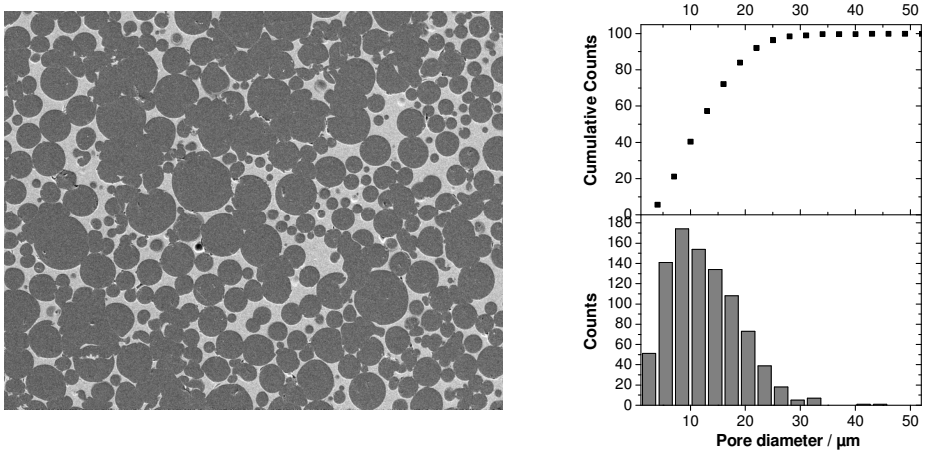

Figure A.2.9- Pore size distribuitiom: left, FESEM image of an impregnated SiOC foam (S25); right, pore diameter counts and cumulative counts.

Figure A.2.10 presents the overview of the cumulative counts for three of the investigated samples. The pores size distribuitions cover the range from about 2 µm to 100 µm.

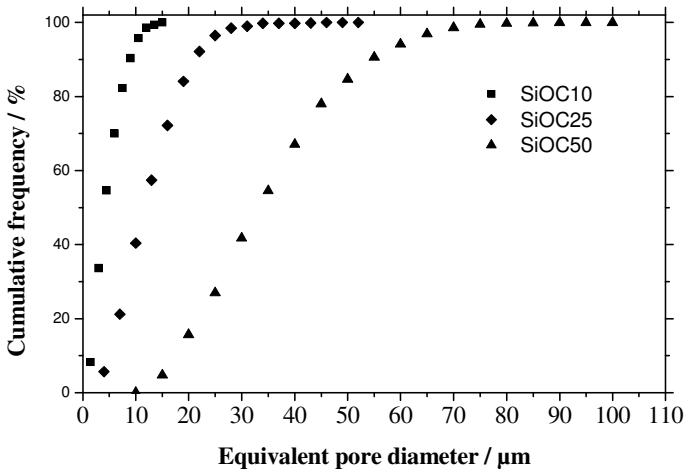

Figure A.2.10- Cumulative counts of the investigated samples

Differentiation of the cumulative curves over discrete intervals yelds the area number density for each size interval (i.e. yhe number of pores in each bin divided by the total area measured). Figure A.2.11 presents the area number density as a function of the equivalent pore diamter for samples S10, S25 and S50; the mean pore diamter increase with increasing PMMA size.

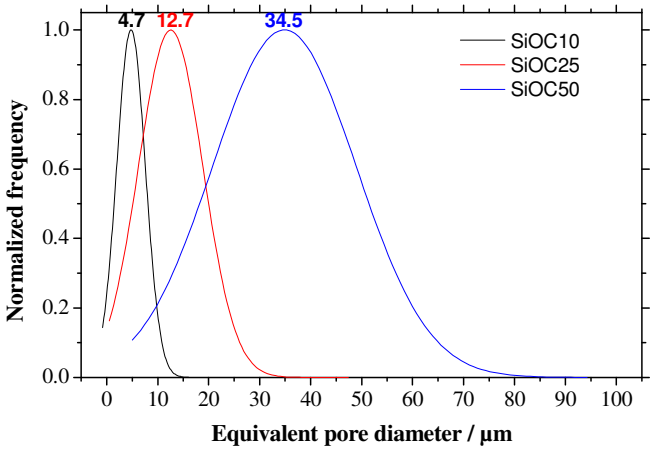

Figure A.2.11- Equivalent pore diameter of the analyzed samples

Assuming that the investigated samples are characterized by a random orientation of spherical pores with a relatively narrow cell size distribuition, a simple stereological correction factor can be applied to determine the three-dimensional mean pore diameter. It can be shown that the average circular segment diameter D_{circ} due to random truncation of the cells with respect to depth at the planeof the specimen surface. The relation can be expressed by the following equation[3,5]:

$$D_{sphere} = \frac{D_{circ}}{0.785} \tag{4}$$

Figure A.2.12 compares the mean pore diameters measured by image analysis routine, calculated from volume shrinkage and by manual measurements on the non embedded samples.

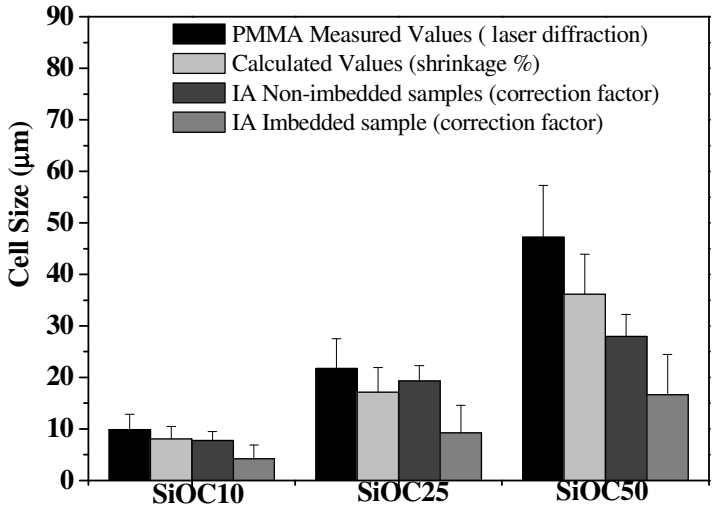

Figure A.2.12- Results overview

By image analysis processing it is possible to measure cell size, porosity percentage and the relative density of the foam. Other techniques are available to measure porosity percentage and cell-window size, such as the already mentioned mercury porosimetry and capillary flow porometry. Since the high amount of literature available for such techniques they will be not discussed further.

A.2.3 Cell-density calculation

There are two different ways of counting the cell density: The first one is to count the number of cells per unit volume with respect to foamed material and the second is with respect to non-foamed material. Both are useful for different purposes. The first one is the traditional way, and it allows an easier understandingof the foam structure.
But the second one is used to describe the processing-to-structure relationships. Since the foam processing (for direct foaming) consists of cell nucleation and cell growth, there has been a strong desire to describe the final cell morphology in terms of cell nucleation and growth behaviors. In other words, by defining the cell density as the density of cell-nuclei (without any consideration of the expansion in this stage), the cell density can be used to indicate how well cell nucleation was conducted. So to speak, the cell density is meant to be the cell-nuclei density indicating the number of cells nucleated in the polymer matrix in the stage of cell nucleation. In our case, the cell density calculated with respect to the non-foamed polymer was used to characterize the foam structure[15].

Figure A.2.13 Cell density calculatin procedure

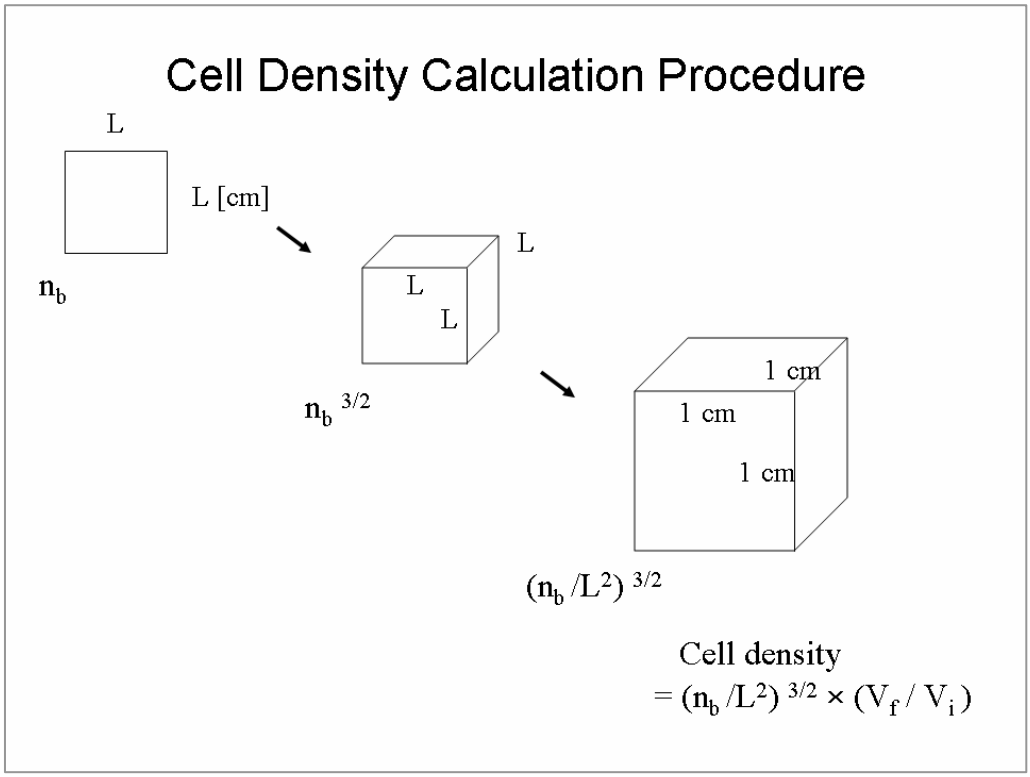

However, since the processing route used to develop microcellular ceramic foams, in the present work, is not related to the cell nucleation and growth, calculations were performed on samples after pyrolysis.

The procedure used for calculations is reported in Figure A.2.14, where:

- n_b is the number of counts inside the farme of size L (see also Figure A.2.15)
- V_f= volume of the foam and V_i=volume of the skeleton

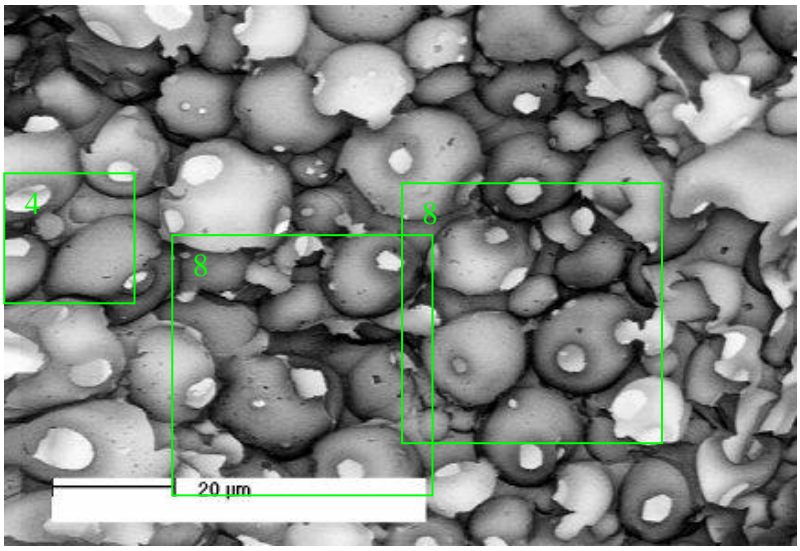

Figure A.2.14- Intermediate step during the cell-density calculation routine

References

[1] Mullens S, Luyten J, and Zeschky J, *Characterization of Structure and Morphology* , in "Cellular Ceramics: Structure, Manifacturing, Properties and Applications", Scheffler M. and Colombo P editors, Wiley Vch, 2004

[2] Wallaeys B., Mortelmans R, Reticel *Brochure technical Foams- The Guide 2000*, Reticel Co. Wetteren (2000)

[3] ASTM Standars, *Standards Test Method for Cell Size of Rigid Cellular Plastics*, ASTM D 3576, 919-22 (1977)

[4] Adler J., Standke G., "Offenzellige Schaumkeramik, Teil 1" Keramische Zeitschrift 55 [9] 694-703 (2003).

[5] Lock P, Jing X, Zimmermann R, Schulueter E, *J. Appl. Phys*., 92, 6311-19 (2002)

[6] Liu Z-Q, austin T, Thomas C, Clement J, *Comput. Biol. Med*., 26, 65-76 (1996)

[7] Càrcel A, Ferrer C, *Determination of Pore size*, in Proceedings of the International Conference on Cellular Metals and Metal Foaming Technology, Banhart J (Ed.), MIT Publications, Berlin, (2003)

[8] Landis E, Petrell A, Nagy E, *Concr. Sci. Eng*., 2, 162-69 (2000)

[9] Underwood E, *Quantitative Stereology*, Addison-Wesley Publishers, Reading (1970)

[10] Royet J, *Prog. Neurobiol*.,37, 433-74 (1991)

[11] Higgins M, Am. Mineral, 85, 1105-1116 (2000)

[12] Cruz-Orive L, *J. Microsc*, 131, 265-90 (1983)

[13] Berger A, rooselle G, *Am. Mineral*, 86, 215-24 (2001)

[14] Moreau E, Velde B, terribile F, *Geoderma*, 92, 55-72 (1999)

[15]. Xu X, Park C.B, Xu D., and Pop-Iliev R., *Polymer Engineering and Science*, 43, 1378-90 (2003)

Ringraziamenti Speciali:
Prof. Paolo Colombo